

Electrodeposition of Mn Oxide Supercapacitors

by

Michael P. Clark

A thesis submitted in partial fulfillment of the requirements for the degree of

Master of Science
in
Materials Engineering

Department of Chemical and Materials Engineering
University of Alberta

© Michael P. Clark, 2015

Abstract

In today's society, the need for renewable energy sources is driving the development of new energy storage devices. Supercapacitors are one such device and are characterized by their large power density, long cycle life, and environmental friendliness. Many novel materials and architectures have been developed to produce supercapacitors with high specific capacitances (F/g). However, many of these materials are not practical for commercial applications because of their high cost and labor intensive production. The goal of this thesis is to produce high performance supercapacitor electrodes using inexpensive materials and an inexpensive and simple electrodeposition technique developed by our research group.

By modifying the electrodeposition process previously developed by our research group, fibrous Mn oxide rods were deposited onto Ni foam substrates. One major factor affecting supercapacitor performance is the electrode surface area; the fibrous micron scale rods greatly improve the electrode surface area and consequently capacitive performance. Deposits were characterized using a variety of materials and electrochemical techniques including scanning electron microscopy (SEM), transmission electron microscopy (TEM) and cyclic voltammetry (CV). The electrodeposited rods are 15-20 μm long, around 2 μm wide, and are petal shaped, with the bases of rods being narrower than the tops. The rods are composed of many sheets, each only a few nanometers wide.

TEM analysis revealed that the sheets are nanocrystalline with a grain size of about 5 nm. Electron diffraction patterns can be indexed to either cubic spinel Mn_3O_4 or hexagonal birnessite MnO_2 . X-ray photoelectron spectroscopy (XPS) indicated that Mn is present in the deposit as a mixture of oxidation states. Mn oxide deposits on Ni foam exhibited a capacitance of 144 F/g (450 mF/cm^2), at a galvanostatic charge/discharge rate of 0.5 mA/cm^2 . During extended cycling,

dissolution and redeposition of Mn oxide caused cracking and peeling of the deposit. After 500 cycles, a change in oxidation state is observed, with the mixed $\text{Mn}^{2+}/\text{Mn}^{3+}$ state being oxidized to Mn^{4+} . Despite the damage caused by cycling, redeposition and the oxidation state change lead to a capacitance increase of 13% over 500 cycles.

With the aim of improving capacitive performance, a conductive polymer coating of polyethylenedioxythiophene (PEDOT) was applied to Mn oxide deposits using an electropolymerization technique. Helium ion imaging revealed that the PEDOT conformally coated the fibrous Mn oxide rods. The PEDOT coating improved the initial capacitance from 144 to 217 F/g (450 to 690 F/cm²). The PEDOT coating successfully prevented dissolution during cycling. Although capacitance dropped by 9% over 500 cycles, the capacitance at cycle 500 for deposits with PEDOT was still larger than deposits without PEDOT.

Deposits were annealed in air and forming gas (95% N₂ and 5% H₂) at 350°C for 1 h. Both annealed deposits experienced an increase in crystallinity with annealing. Deposits annealed in air retained their cubic spinel Mn₃O₄ structure, while deposits annealed in forming gas transformed to a tetragonal spinel Mn₃O₄ structure. The capacitances of deposits annealed in air and forming gas were 93 and 56 F/g (230 and 170 mF/cm²), respectively, measured by CV at a scan rate of 10 mV/s.

The nucleation and growth of electrodeposited Mn oxide rods was investigated by preparing deposits on Au coated Si at varying deposition times between 0.5 s and 5 min. The deposits were investigated using high resolution SEM and TEM. A model for the nucleation and growth of Mn oxide rods has been proposed.

TEM analysis of 3 s and 6 s deposits shows that the sheets are initially amorphous and then begin to crystallize into a cubic spinel Mn_3O_4 crystal structure. High resolution imaging of the 6 s sample shows small crystalline regions (~5 nm in size) within an amorphous matrix.

Acknowledgements

I would like to thank Dr. Douglas G. Ivey for his support and guidance throughout my Master's program. I have always appreciated his to-the-point feedback and skeptical outlook on research. I have learned a great deal while under his supervision and am grateful for his love of teaching, patience, and compassion.

Financial support from the Natural Sciences and Engineering Research Council (NSERC), the Government of Alberta, the Faculty of Graduate Studies and Research (FGSR), the Electrochemical Society (ECS), and the Graduate Student's Association (GSA) is gratefully acknowledged.

For technical support and input, I thank Mr. Wei Qu from the National Research Council, Canada (NRC). For help with structural analysis, I would like to thank Dr. Anqiang He (TEM/XPS), Dr. Neda Dalili (TEM), Ms. Gayle Hatchard (SEM), Dr. Shihong Xu (XPS), Dr. Dimitre Karpuzov (XPS), and Dr. Peng Li (HIM). For help with laboratory work, I would like to thank our summer and co-op students Ms. Aliesha Johnson, Mr. Prakhar Sharma, and Mr. Daniel Bouliane.

The support of friends and family over the duration of my degree has been tremendous and is greatly appreciated. The help and knowledge of my friend and fellow student Ellie Davari has been critical both in course work and during my research. Without the loving support of my parents over the last few years, completing my degree would have been extremely difficult and I am very grateful to have them.

Table of Contents

Chapter 1: Introduction	1
1.1 References.....	3
Chapter 2: Literature Review	4
2.1 <i>Electrochemical Capacitors</i>	4
2.1.1 Electrical double layer capacitors.....	5
2.1.2 Faradaic capacitance.....	7
2.1.2.1 Adsorption/desorption.....	7
2.1.2.2 Lattice intercalation.....	7
2.1.2.3 Redox reactions.....	7
2.2 <i>Materials for Electrochemical Capacitors</i>	8
2.2.1 Carbon based materials.....	8
2.2.2 Transition metal oxides.....	9
2.2.2.1 Ruthenium oxide.....	9
2.2.2.2 Manganese oxide.....	10
2.2.2.3 Other oxides.....	13
2.2.3 Conducting polymers.....	14
2.2.3.1 Poly(3,4-ethylenedioxythiophene) (PEDOT).....	15
2.2.4 Composites.....	15
2.3 <i>Electrochemical Synthesis</i>	16
2.3.1 Electrodeposition of Mn oxide.....	16
2.3.2 Electropolymerization of PEDOT.....	18
2.3.3 Nucleation and growth.....	18
2.4 <i>Characterization Techniques</i>	20
2.4.1 Materials techniques.....	20
2.4.1.1 Scanning electron microscopy.....	21
2.4.1.2 Transmission electron microscopy.....	21
2.4.1.3 X-ray photoelectron spectroscopy.....	22
2.4.2 Electrochemical techniques.....	22
2.4.2.1 Cyclic voltammetry.....	22
2.4.2.2 Galvanostatic cycling.....	24
2.4.2.3 Electrochemical impedance spectroscopy.....	24
2.5 <i>Previous Work in the Ivey Research Group</i>	25
2.5.1 Electrodeposition of Mn oxide for electrochemical capacitors.....	25
2.5.2 Effect of electrodeposition conditions on Mn oxide deposits.....	26
2.5.3 Improved capacitive behavior of Mn oxide/PEDOT electrodes.....	27
2.5.4 Electrochemical behavior of Co doped Mn oxide.....	28
2.6 <i>References</i>	29

Chapter 3: Electrodeposition of Mn oxide Rods on Ni Foam	38
3.1 <i>Introduction</i>	38
3.2 <i>Experimental</i>	40
3.2.1 Mn oxide deposition.....	40
3.2.2 Electropolymerization of PEDOT.....	41
3.2.3 Materials characterization.....	41
3.2.4 Electrochemical characterization.....	42
3.3 <i>Results and Discussion</i>	42
3.3.1 Mn oxide deposition conditions.....	42
3.3.2 PEDOT deposition.....	46
3.3.3 Transmission electron microscopy.....	48
3.3.4 X-ray photoelectron spectroscopy.....	50
3.3.5 Cyclic voltammetry.....	52
3.3.6 Galvanostatic cycling.....	56
3.3.7 Annealing of Mn oxide deposits.....	58
3.4 <i>Conclusions</i>	60
3.5 <i>References</i>	61
Chapter 4: Nucleation and Growth of Mn Oxide Rods	64
4.1 <i>Introduction</i>	64
4.1.1 Nucleation and Growth.....	64
4.1.2 Anodic electrodeposition of Mn oxide.....	64
4.2 <i>Experimental</i>	66
4.2.1 Mn oxide deposition.....	66
4.2.2 Scanning electron microscopy.....	66
4.2.3 Transmission electron microscopy.....	67
4.2.4 X-ray photoelectron spectroscopy.....	67
4.3 <i>Results and Discussion</i>	67
4.3.1 Scanning electron microscopy.....	67
4.3.2 X-ray photoelectron spectroscopy.....	73
4.3.3 Transmission electron microscopy.....	74
4.4 <i>Conclusions</i>	77
4.5 <i>References</i>	77
Chapter 5: Conclusions and Recommendations	79
5.1 <i>Conclusions</i>	79
5.1.1 Nickel foam work.....	79
5.1.2 Nucleation and growth work.....	80
5.2 <i>Recommendations</i>	80
References	82
Appendix	92

List of Tables

Table 2-1: Mn oxide (MnO ₂) crystal structures from Ghodbane et al.	11
Table 2-2: Comparison of various metal oxides.	14
Table 2-3: Capacitance results for various Mn oxide nanostructures. Cycled in 0.5 M Na ₂ SO ₄ at 20 mV/s.	27

List of Figures

Figure 2-1: Ragone plot comparing various energy storage devices.	4
Figure 2-2: Schematic of a double-layer EC.	5
Figure 2-3: Stern model for electrical double layer charge storage at a positively charged surface. IHP and OHP are the inner and outer Helmholtz planes and refer to the distance of closest approach for specifically and non-specifically adsorbed ions, respectively. ψ is the potential in the electrolyte and ψ_0 is the potential at the electrode surface.	6
Figure 2-4: Schematic voltammogram of MnO ₂ in 0.1 M K ₂ SO ₄ , showing successive redox reactions resulting in capacitive behavior.	8
Figure 2-5: Schematic representation of Mn oxide (MnO ₂) crystal structures: (A) pyrolusite β -MnO ₂ , (B) ramsdellite, (C) birnessite δ -MnO ₂ , and (D) spinel λ -MnO ₂	12
Figure 2-6: Capacitance, ionic conductivity, and specific surface area for various Mn oxide crystal structures, from Ghodbane et al.	12
Figure 2-7: Mn oxide morphologies obtained through anodic electrodeposition. (A) 3D fibrous network, (B,C) Mn oxide rods grown from a dilute electrolyte, (D) fibrous surface of a rod from (C), (E) Mn oxide rods grown by CV, (F) interconnected nanosheets grown by CV.	17
Figure 2-8: Schematic of (A) instantaneous, and (B) progressive nucleation mechanisms. [95].	19
Figure 2-9: Heterogeneous growth mechanisms: (a) Volmer-Weber (b) Frank-van der Merwe, and (c) Stanski-Krastanov.	20
Figure 2-10: Schematic representation of an ideal cyclic voltammogram. C is capacitance, I_f is the forward sweep current, I_b is the backward sweep current, and v is the scan speed.	23
Figure 2-11: Schematic representation of a GSC curve for an ideal capacitor. C is the capacitance, V is the voltage, and t is the time.	24
Figure 2-12: SEM SE micrographs of Mn oxide deposits prepared from (A,B) 0.01 M MnSO ₄ at 30 mA/cm ² and (C,D) 0.01 M Mn(CH ₃ COO) ₂ at 5 mA/cm ²	25
Figure 2-13: CV curves for deposits (A) without PEDOT, and (B) with PEDOT. Cycling was done in 0.5 M Na ₂ SO ₄ at 20 mV/s. Potential is vs. SCE.	28
Figure 3-1: SEM SE images (plan view and cross section) of Mn oxide rods on Au coated Si, The deposits were prepared from 0.01 M Mn(CH ₃ COO) ₂ at 60°C at a current density of 5 mA/cm ² for 10 min.	39
Figure 3-2: Cell schematic for Mn oxide deposition on Ni foam.	41
Figure 3-3: SEM SE images of Mn oxide deposits prepared using the Mn(C ₂ H ₃ O ₂) ₂ electrolyte with NH ₄ (C ₂ H ₃ O ₂) and DMSO as additives, at various current densities: (A, E) 5 mA/cm ² , (B, F)	

10 mA/cm ² , (C, G) 15 mA/cm ² , and (D, H) 20 mA/cm ² . Depositions were conducted for 5 min.	43
Figure 3-4: SEM SE images of Mn oxide deposits prepared at varying rotation speeds: (A) 50 RPM, (B) 75 RPM, and (C) 100 RPM. The current density and deposition time were 20 mA/cm ² and 2.5 min, respectively.	44
Figure 3-5: SEM SE images of Mn oxide deposits prepared with varying deposition times: (A, D) 2.5 min, (B, E) 5 min, and (C, F) 10 min. Deposition current density was 20 mA/cm ² and rotation speed was 75 RPM.	45
Figure 3-6: SEM SE images of Mn oxide deposits. (A) Side view of Mn oxide rods, (B) Mn oxide deposit within the Ni foam porosity. Mn oxide deposits were prepared at 20 mA/cm ² for 5 min at 75 RPM.	46
Figure 3-7: SEM SE images of Mn oxide deposits: (A,C) without PEDOT, (B,D) with PEDOT. Mn oxide deposits were prepared using 20 mA/cm ² for 5 min at 75 RPM. The PEDOT coating was prepared at 1 V for 45 s.	47
Figure 3-8: HIM SE images of Mn oxide deposits: (A) without PEDOT, (B) with PEDOT. Mn oxide deposits were prepared on Au coated Si at 5 mA/cm ² for 5 min. The PEDOT coating was prepared at 1 V for 45 s.	47
Figure 3-9: TEM results for Mn oxide deposits. (A,B) as deposited, (C-E) cycled 500 times at 20 mV/s. (A,C) Bright field images, (B,D) diffraction patterns from the regions shown in A and C, (E) dark field image. The samples were deposited at 20 mA/cm ² for 10 min, with a rotation speed of 75 RPM.	49
Figure 3-10: High resolution TEM image of Mn oxide deposits. (A) as deposited, and (B) cycled at 20 mV/s for 500 cycles. The samples were prepared at 20 mA/cm ² for 10 min, with a rotation speed of 75 RPM.	50
Figure 3-11: XPS Mn 3s spectra for as deposited and cycled Mn oxide (500 cycles). Mn oxide deposits were prepared at 20 mA/cm ² for 5 min at 75 RPM.	51
Figure 3-12: Mn 3s XPS peak splitting as a function of Mn oxidation state in MnO _x	51
Figure 3-13: CV curves at varying scan speeds for deposits: (A) Without PEDOT and (B) with PEDOT. Mn oxide deposits were prepared at 20 mA/cm ² for 5 min at 75 RPM. The PEDOT coating was prepared at 1 V for 45 s.	53
Figure 3-14: Capacitance values at various scan speeds. Mn oxide deposits were prepared at 20 mA/cm ² for 5 min at 75 RPM. The PEDOT coating was prepared at 1 V for 45 s.	53
Figure 3-15: Capacitance values as a function of cycle number, at a scan rate of 20 mV/s. Mn oxide deposits were prepared at 20 mA/cm ² for 5 min at 75 RPM. The PEDOT coating was prepared at 1 V for 45 s.	54
Figure 3-16: SEM SE images of Mn oxide deposits after 500 cycles: (A,C) Without PEDOT and (B,D) with PEDOT. Note the regions of Mn oxide redeposition for the uncoated Mn oxide sample, indicated by the arrow in (C). Mn oxide deposits were prepared at 20 mA/cm ² for 5 min at 75 RPM. The PEDOT coating was prepared at 1 V for 45 s.	55

Figure 3-17: GSC curves for Mn oxide deposits on Ni foam at varying charge/discharge rates: (A,B) without PEDOT, (C,D) with PEDOT. Mn oxide deposits were prepared at 20 mA/cm² for 5 min at 75 RPM. The PEDOT coating was prepared at 1 V for 45 s..... 57

Figure 3-18: Capacitance values as a function of constant current charge/discharge rate. Mn oxide deposits were prepared at 20 mA/cm² for 5 min at 75 RPM. The PEDOT coating was prepared at 1 V for 45 s..... 58

Figure 3-19: TEM results for Mn oxide deposits annealed for 1 h at 350°C in (A-C) air and (D-E) forming gas (95% N₂ + 5% H₂). (A,B) Bright field images, (B,E) selected area diffraction patterns, and (C,F) dark field images using part of the innermost rings. Mn oxide deposits were prepared at 20 mA/cm² for 5 min at 75 RPM..... 59

Figure 3-20: CV curves for deposits annealed in air and forming gas (95% N₂ 5% H₂) for 1 h at 350°C. Scan speed of 10 mV/s. Mn oxide deposits were prepared at 20 mA/cm² for 5 min at 75 RPM..... 60

Figure 4-1: SEM SE micrographs of the early stages of nucleation and growth of Mn oxide. Deposition times were (A) 1 s (bare Au inset at same magnification), (B) 2 s and (C, D) 4 s..... 68

Figure 4-2: SEM SE micrographs of Mn oxide deposition: (A) 5 s, (B) 6 s, (C) 8 s, and (D) 10 s. The circled areas in (C) show larger particles that have experienced accelerated growth. (D) is a high magnification image of one such particle after a deposition time of 10 s. 69

Figure 4-3: Schematic representation of the formation of round particles from coalescing sheets. When a sheet is formed, preferred nucleation sites are introduced at the base of the sheet. New sheets will form heterogeneously at these nucleation sites. As more sheets continue to form alongside each other, they agglomerate and eventually form into round particles..... 69

Figure 4-4: SEM SE micrographs of Mn oxide rod formation. Deposition times were (A, B) 30 s and (C, D) 60 s. The boxes in A and C show the fields of view for B and D, respectively. 70

Figure 4-5: SEM SE micrographs showing the Mn oxide rod structure after 5 min deposition. (A-C) are plan view images at successively higher magnifications. (D) is a cross section image. The white circle in (D) shows a rod that has been squeezed out by the growth of neighboring rods.. 72

Figure 4-6: Schematic illustrating the effect of increasing deposit height on the resistance of the deposit. As deposition occurs, Mn ions from the solution lose two electrons, each in separate steps: oxidation of Mn²⁺ to Mn³⁺ and oxidation of Mn³⁺ to Mn⁴⁺. After each of these steps, the released electron must travel through the Mn oxide deposit to the Au current collector. As the electron passes through the Mn oxide, it experiences some resistance, R. As deposition proceeds, the height and, consequently, the resistance of the oxide layer increases (R₂>R₁). Because Mn oxide is poorly conductive, small changes in deposit height cause large changes in the deposit resistance. An increase in deposit resistance causes a decrease in the potential at the surface of the deposit, which reduces deposition rate. This effect causes shorter rods to grow more quickly than longer rods, and ultimately leads to rods that are uniform in height. 72

Figure 4-7: Schematic representation of the nucleation and growth process of Mn oxide rods. (A) Nucleation initiates as thin sheets along grain boundaries and triple points. (B) New sheets continue to nucleate, spreading away from the grain boundaries until sheets cover the gold

surface. (C) As more sheets form, they begin to agglomerate into round particles. (C) and (D) are at a lower magnification than (A) and (B). (D) Shortly after the transition from sheet-like to round particles, some particles begin to accelerate in growth. At first the accelerated growth is omnidirectional, but once the particle is about 1 μm in diameter, growth is primarily away from the sample surface. As deposition continues, new rods form from the round particles between existing rods. (E) After about 5 min of deposition, the Au surface is covered with petal shaped Mn oxide rods. 73

Figure 4-8: Mn 3s XPS spectra for 3 and 6 s Mn oxide deposits prepared on Pt coated Si. 74

Figure 4-9: TEM results for Mn oxide deposits after deposition times of 3 s (A-C) and 6 s (D-F). Bright field images are shown in A and D, B and E are SAED patterns, and C and F are dark field images. 76

Figure 4-10: High resolution images Mn oxide sheets after a deposition times of 3s (A) and 6 s (B). A shows an amorphous structure while B shows a mixture of crystalline (one example is circled in white) and amorphous regions. 76

Chapter 1: Introduction

Over the past few decades, electrochemical energy storage devices such as batteries, fuel cells and electrochemical capacitors have been gaining an increasing amount of interest from academia as well as industry. This interest is fueled largely by the development of hybrid and electric vehicles as well as the drive towards renewable energy sources. Electrochemical capacitors are characterized by their high power density, long cycle life, and low cost. Electrochemical capacitors are used in conjunction with other energy storage devices to provide a burst of power during periods of high load such as accelerating an electric vehicle. Some other applications for electrochemical capacitors are portable electronics, energy grids, and emergency power supplies. [1,2]

Mn oxide is of particular interest to many researchers because it is inexpensive, environmentally benign and has a high theoretical capacitance. Mn oxide, like many transition metal oxides, stores charge in two ways: electrostatically in the double layer and through Faradaic reactions at the surface as well as in the bulk of the electrode. The theoretical capacitance of Mn oxide is difficult to achieve because of Mn oxide's poor electronic and ionic conductivity. Much of the recent work on Mn oxide electrochemical capacitors has been aimed at addressing the poor conductivity of Mn oxide electrodes by creating nanoscale architectures and/or forming composites with conductive materials like carbon and conducting polymers. [3,4] The use of conductive porous substrates such as high surface area carbon or Ni foam can also help address the poor conductivity of Mn oxide. The porosity of these substrates facilitates the electrochemical activity of material deep within the substrate, which allows much more material to be deposited per unit area than a planar substrate would allow. Over the past few years Ni foam has become a popular substrate for Mn oxide electrochemical capacitors and has been shown to facilitate very high areal capacities. [5-8]

Electrodeposition is a popular method of producing Mn oxide electrochemical capacitors because it is inexpensive, easy to perform and is able to conformally coat complex shapes. Deposition parameters such as temperature, time, current, electrolyte composition and agitation are easily modified and can have an effect on the properties of the resulting deposit. By varying

deposition conditions, a wide variety of deposit morphologies can be obtained. Some Mn oxide morphologies achieved through electrodeposition are sheets, rods, fibers, and particles.

In previous work by our research group, a template free process to electrodeposit high surface area Mn oxide rods onto Au coated Si substrates and coat them with a conductive polymer, polyethylenedioxythiophene (PEDOT), was developed. [9-11] These deposits exhibited good specific capacitances, but due to their low mass, had poor areal capacitance. In practical applications for electrochemical capacitors, areal capacitance is a more relevant measure of performance than specific capacitance.

This thesis is broken into five main sections, the first being the Introduction. Section 2 is a literature review that contains information on the basics of supercapacitors, materials for supercapacitors, electrochemical synthesis, characterization techniques, and a summary of our group's previous work on Mn oxide.

The first objective of this work is to apply the deposition process previously developed by our research group to Ni foam, a more practical substrate, with the aim of achieving high areal capacitance. This work is covered in Section 3. To achieve high surface area Mn oxide rods on Ni foam, select deposition conditions are varied, using the conditions from Babakhani and Ivey's work as a starting point. Deposits are characterized using a variety of material and electrochemical techniques. The effect of applying a PEDOT coating to deposits on Ni foam is also investigated.

The second objective of this work is to characterize the nucleation and growth of electrodeposited Mn oxide rods. Section 4 utilizes high resolution scanning electron microscopy (SEM) and transmission electron microscopy (TEM) to visualize deposits at various stages of deposition and a model for the nucleation and growth process of electrodeposited Mn oxide rods is proposed.

Section 5 concludes the thesis and contains recommendations for future work.

1.1 References

- [1] R. Ko and M. Carlen, “Principles and applications of electrochemical capacitors,” *Electrochem. commun.*, vol. 45, pp. 2483–2498, 2000.
- [2] P. Simon and Y. Gogotsi, “Materials for electrochemical capacitors,” *Nat. Mater.*, vol. 7, no. 11, pp. 845–54, Nov. 2008.
- [3] G. Wang, L. Zhang, and J. Zhang, “A review of electrode materials for electrochemical supercapacitors,” *Chem. Soc. Rev.*, vol. 41, no. 2, pp. 797–828, Jan. 2012.
- [4] W. Wei, X. Cui, W. Chen, and D. G. Ivey, “Manganese oxide-based materials as electrochemical supercapacitor electrodes,” *Chem. Soc. Rev.*, vol. 40, no. 3, pp. 1697–721, Mar. 2011.
- [5] Z. Sun, S. Firdoz, E. Y.-X. Yap, L. Li, and X. Lu, “Hierarchically structured MnO₂ nanowires supported on hollow Ni dendrites for high-performance supercapacitors,” *Nanoscale*, vol. 5, no. 10, pp. 4379–87, May 2013.
- [6] J. Xiao, S. Yang, L. Wan, F. Xiao, and S. Wang, “Electrodeposition of manganese oxide nanosheets on a continuous three-dimensional nickel porous scaffold for high performance electrochemical capacitors,” *J. Power Sources*, vol. 245, pp. 1027–1034, Jan. 2014.
- [7] J. Yang, L. Lian, H. Ruan, F. Xie, and M. Wei, “Nanostructured porous MnO₂ on Ni foam substrate with a high mass loading via a CV electrodeposition route for supercapacitor application,” *Electrochim. Acta*, vol. 136, pp. 189–194, Aug. 2014.
- [8] P. Xu, K. Ye, D. Cao, J. Huang, T. Liu, K. Cheng, J. Yin, and G. Wang, “Facile synthesis of cobalt manganese oxides nanowires on nickel foam with superior electrochemical performance,” *J. Power Sources*, vol. 268, pp. 204–211, Dec. 2014.
- [9] B. Babakhani and D. G. Ivey, “Effect of electrodeposition conditions on the electrochemical capacitive behavior of synthesized manganese oxide electrodes,” *J. Power Sources*, vol. 196, no. 24, pp. 10762–10774, Dec. 2011.
- [10] B. Babakhani and D. G. Ivey, “Anodic deposition of manganese oxide electrodes with rod-like structures for application as electrochemical capacitors,” *J. Power Sources*, vol. 195, no. 7, pp. 2110–2117, Apr. 2010.
- [11] B. Babakhani and D. G. Ivey, “Improved capacitive behavior of electrochemically synthesized Mn oxide/PEDOT electrodes utilized as electrochemical capacitors,” *Electrochim. Acta*, vol. 55, no. 12, pp. 4014–4024, Apr. 2010.

Chapter 2: Literature Review

2.1 Electrochemical Capacitors

Electrochemical capacitors (ECs) have gained an increasing amount of attention over recent years, mainly because of their high power density, long cycle life, wide operating temperature range, and ability to bridge the power/energy gap between batteries and conventional dielectric capacitors. Figure 2-1 shows a Ragone plot, which compares a number of energy storage devices. [1] ECs are also known as supercapacitors, ultracapacitors, Faradaic capacitors, pseudocapacitors, and electrochemical double layer capacitors, as well as many other names. Some of the names given to ECs have been used to try to define specific types of EC in terms of their properties; however, there is currently no consensus on the strict definition for many of the names given to ECs.

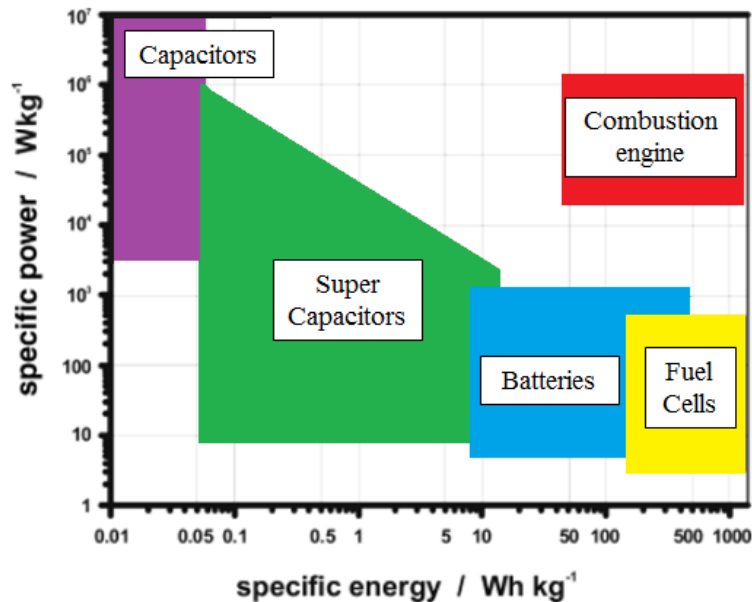


Figure 2-1: Ragone plot comparing various energy storage devices. [2]

The first patents for ECs were filed in 1957; however, significant developments were not made until the introduction of hybrid vehicles in the 1990's. If used in conjunction with batteries or fuel cells, ECs could provide an energy boost during acceleration and allow for energy recuperation during braking. Other applications for EC include hand-held electronics, renewable energy storage, and emergency power supplies. [1,3]

ECs are similar to batteries in their design and manufacturing; Figure 2-2 shows a schematic for an EC. An EC consists of two electrodes, two current collectors, an electrolyte, and a separator to electrically isolate the two electrodes. [1] The electrodes are typically high in surface area and can be made from a variety of materials. Energy storage can occur through a number of different mechanisms for an EC, depending on the properties of the electrodes and the electrolyte. The electrode material, among other factors such as surface area, crystallinity, pore size, and morphology, strongly affects the performance of an EC. [1,3]

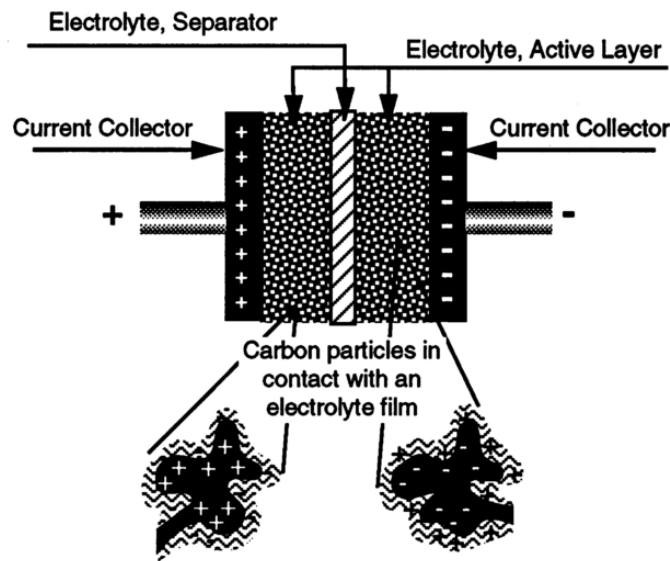


Figure 2-2: Schematic of a double-layer EC. [3]

2.1.1 Electrical double layer capacitance

ECs can be categorized into two groups, depending on their dominant charge storage mechanism. The first type of electrochemical capacitor is an electrical double layer capacitor (EDLC). These materials store charge in the electrical double layer formed by electrostatic accumulation of electrolyte ions at the electrode surface. [3-7] Polarization at the sample surface produces what Helmholtz described in 1853 as double layer capacitance: [8]

$$C = \frac{\epsilon_r \epsilon_0}{d} A \quad (2-1)$$

where ϵ_r is the electrolyte dielectric constant, ϵ_0 is the permittivity of free space, d is the effective thickness of the double layer, and A is the specific surface area of the electrode with access to electrolyte ions. The Helmholtz model was refined by Gouy and Chapman, as well as Stern and Geary, who suggested that ions are distributed between two regions - the compact layer (Stern layer) and the diffuse layer. In the compact layer, ions are strongly adsorbed to the electrode surface. The diffuse layer, as described by Gouy and Chapman, consists of a continuous distribution of electrolyte ions. [5-7] Depending on the electrolyte used, the double layer capacitance yields around 5-50 $\mu\text{F}/\text{cm}^2$. [7,9] Figure 2-3 shows the proposed model for electrical double layer charge storage. [4]

Charge storage processes occurring at the electrode surface give rise to some advantages for EDLCs. EDLCs exhibit large power densities and high charge/discharge rates because the kinetics of surface adsorption and desorption for ions is fast. In batteries and Faradaic capacitors, reduction/oxidation (redox) reactions cause volume changes during cycling, causing mechanical degradation and reduction of cycle life. Redox reactions do not occur in EDLCs, providing excellent cycle life (>100000 cycles) and nearly ideal capacitive behavior. [5,7] An ideal capacitor exhibits a constant current over the entire voltage window, resulting in a cyclic voltammetry (CV) curve in the shape of a rectangle.

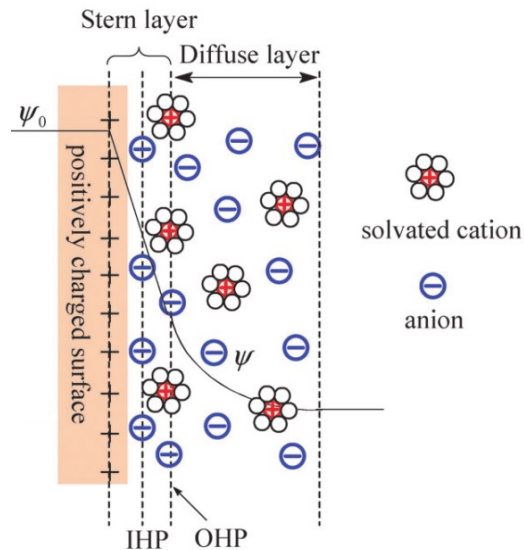


Figure 2-3: Stern model for electrical double layer charge storage at a positively charged surface. IHP and OHP are the inner and outer Helmholtz planes and refer to the distance of closest approach for specifically and non-specifically adsorbed ions, respectively. ψ is the potential in the electrolyte and ψ_0 is the potential at the electrode surface. [4]

2.1.2 Faradaic capacitance

The second charge storage mechanism involves reversible Faradaic reactions that occur at the electrode material. A capacitor exhibiting this mechanism is referred to as a Faradaic capacitor (FC). Three types of Faradaic reactions can take place in FCs: adsorption/desorption of ions, intercalation of ions into the lattice, and redox reactions. [3,6,10] Storing charge through Faradaic reactions allows for capacitance values that are 10-100 times larger than those for EDLCs. However, Faradiac reactions in FCs tend to be slower than for non-Faradaic reactions in EDLCs, resulting in lower power densities for FCs. FCs can also suffer from poor cycling stability due to structural changes of the electrode material during cycling. [3,10]

2.1.2.1 Adsorption/desorption

Adsorption of cations onto a surface is known as underpotential deposition (UPD). Some well-known cases of UPD are H^+ adsorption on Pt, Pb, and Au. UPD results in a monolayer or quasi-monolayer of electrochemically active species that can be adsorbed/desorbed quickly and reversibly. Since these reactions do not rely on diffusion or phase changes, UPD charge storage is fast and does not damage the structure of the electrode. As with EDLCs, the amount of charge that can be stored on an electrode is dependent on the effective surface area. CV curves of capacitors exhibiting primarily UPD mechanisms result in nearly ideal capacitive behavior. [11]

2.1.2.2 Lattice intercalation

Lattice intercalation and UPD mechanisms are similar in that they both result in nearly ideal capacitive behavior. Unlike UPD, however, intercalation occurs within the bulk of the electrode, increasing utilization of the electrode material. [11] Intercalation of electrolyte ions into the crystal structure of the electrode introduces strains to the lattice; during cycling this can lead to mechanical degradation. The amount of charge that an electrode can store through intercalation is dependent on the crystal structure and ionic conductivity of the electrode material. [12]

2.1.2.3 Redox reactions

Redox reactions for many metal oxides and metal hydroxides can give rise to capacitive behavior. Redox reactions typically result in high capacitance values; however, they can cause structural damage to the electrode, reducing cycle life. CV curves for an electrode undergoing a

redox reaction are not rectangular. Redox reactions typically lead to a large peak current at the potential associated with that reaction. If a material exhibits multiple successive redox peaks that overlap, it is possible to generate a rectangular voltammogram; this material would be a redox capacitor. [7,10] A schematic of how overlapping redox reactions can yield a rectangular voltammogram is shown in Figure 2-4. [7]

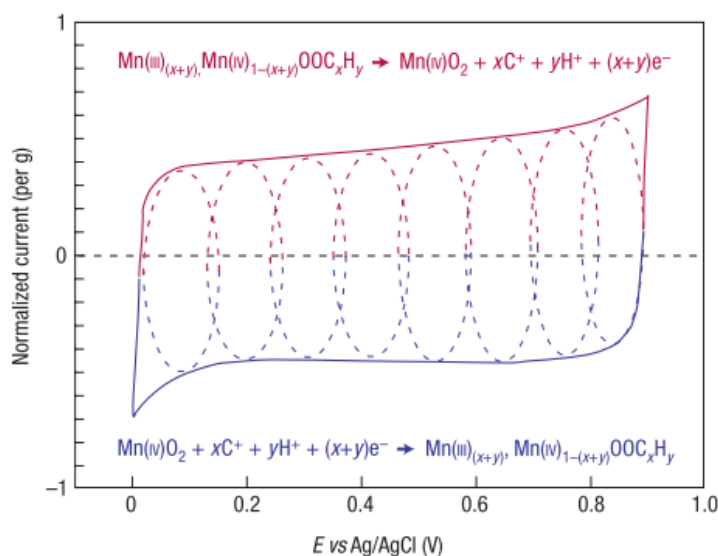


Figure 2-4: Schematic voltammogram of MnO_2 in 0.1 M K_2SO_4 , showing successive redox reactions resulting in capacitive behavior. [7]

2.2 Materials for Electrochemical Capacitors

For a material to be utilized as an electrochemical capacitor, it must exhibit one or more of the charge storage mechanisms mentioned above. Materials properties, such as ionic conductivity, electronic conductivity, crystallinity, and morphology, affect device performance and should be considered when selecting a material for an electrochemical capacitor. In general, materials for ECs can be categorized into four groups: carbon materials, transition metal oxides, conducting polymers, and composites. [3]

2.2.1 Carbon-based materials

High surface area carbon materials are commonly used as EC electrodes because of their large surface area, moderate cost, good electrical conductivity, high chemical stability, and wide range of operating temperatures. [3,5] Carbon-based materials rely on the double layer mechanism of charge storage, facilitating high power densities and fast charge/discharge rates. However, the

double layer mechanism limits the energy density of carbon ECs; FCs are capable of much higher energy densities. [7]

Many types of carbon have been investigated as EC materials including activated carbon, carbon nanotubes, graphene, graphene oxide, and carbon aerogels. [5,10-13,17-19] Carbon materials have capacitance values that range from tens of F/g up to around 300 F/g. The capacitance of carbon based materials is highly dependent on the electrochemically active surface area. Some practical limitations for carbon ECs are the trade-off between surface area and electrical conductivity, as well as the ability to control porosity size distribution. Because charge in carbon materials is stored electrostatically, the energy density of carbon ECs is low compared with FCs. [5,9]

2.2.2 Transition metal oxides

Transition metal oxides typically exhibit multiple charge storage mechanisms. Not only do transition metal oxides store charge electrostatically like carbon, but they also store charge through Faradaic mechanisms. [3,20] Faradaic charge storage mechanisms facilitate high energy densities for transition metal oxide ECs, but can lead to reduced cycle life. The oxides and hydroxides of many metals have been investigated, including Ir, Co, Mo, Ti, V, Sn, Fe, Mn, Ru, Ni, and Co. [3,6] Of the metal oxides investigated, the oxides of Ru and Mn have received the most attention.

2.2.2.1 Ruthenium oxide

Hydrated Ru oxide has many properties beneficial to capacitive performance, including high ionic and electronic conductivity, high specific capacitance, good thermal stability, and high rate capability. [3,6] Ru oxide has a conductivity on the order of 1000 S/cm. [21] Ru oxide has three distinct oxidation states within a 1.2 V potential window. The transitions between oxidation states occur quickly and reversibly. Charge storage in a Ru oxide electrode occurs largely at or near the electrode surface. This necessitates high surface area Ru oxide. Cyclic voltammetry of Ru oxide gives a rectangular shaped curve over a wide potential range of 1.4 V. [22,23] Depending on the preparation procedure, capacitance values for Ru oxide typically fall in the range of 700-900 F/g. A general redox process for hydrated Ru oxide has been proposed: [3,23]



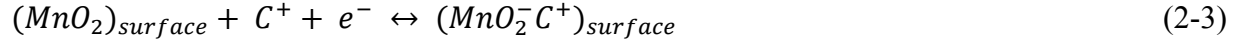
The exact mechanism of oxidation depends on the pH of the electrolyte. The performance of a Ru oxide capacitor is dependent on three main factors: effective surface area, degree of hydration, and crystallinity. [3,22] The amount of combined water in the Ru oxide structure strongly affects the ionic conductivity of the material. The presence of H₂O and OH⁻ sites in the bulk allow for increased cation mobility and thus increases the amount of material that is electrochemically active. [3] The degree of crystallinity also affects the ionic conductivity of Ru oxide. Highly crystalline Ru oxide has difficulty expanding, preventing electrolyte cations from accessing the bulk material. Amorphous Ru oxide is able to accommodate cation access into the bulk, resulting in better performance for amorphous Ru oxide compared with its crystalline counterpart. [3]

Although Ru oxide has proven to be an excellent electrode material for ECs, the cost of Ru limits the use of Ru oxide capacitors to high cost military and aerospace applications. [1] Recent research on Ru oxide has been aimed at maximizing the use of Ru oxide by making composites and developing nanostructured Ru oxide. [3,19] Composites will be discussed further in a later section.

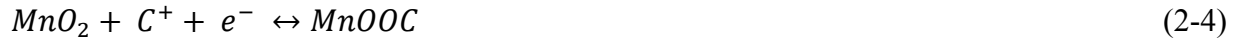
2.2.2.2 Manganese oxide

Mn oxide is inexpensive, environmentally benign, and has a high theoretical capacitance of 1100 F/g. However, Mn oxide suffers from poor electronic and ionic conductivity, which makes achieving the theoretical capacitance quite difficult. The conductivity of Mn oxide is on the order of 10⁻⁵-10⁻⁶ S/cm. [24] Low structural stability and dissolution during cycling are typical for Mn oxides and can cause reduced cycle life. Mn oxide has a variety of stable oxidation states and a number of reversible redox transitions between the states. [3,25] There are a number of irreversible reactions that can occur as well. These reactions mostly occur under negative potentials and limit the minimum operating voltage to 0 V vs. Ag/AgCl. The anodic cut-off voltage is determined by the oxygen evolution reaction. The typical voltage window for Mn oxide ECs is 0-0.8 V vs Ag/AgCl. [26]

Charge storage in Mn oxide materials is mostly Faradaic, with some contribution from the electrical double layer. Adsorption/desorption of electrolyte cations (C⁺ = Li⁺, Na⁺, K⁺, etc.) occurs at the surface: [12,20,25-30]



Adsorption/desorption at the surface is the dominant charge storage mechanism for amorphous Mn oxides, whereas intercalation/deintercalation is the dominant mechanism in crystalline Mn oxides. [30] Intercalation/deintercalation of electrolyte cations occurs in the bulk of the electrode and can be described by the following reaction: [12,20,25-30]



Both charge storage mechanisms utilize a redox reaction between the III and IV oxidation states of Mn ions. [3,26,27] The poor ionic conductivity of Mn oxide limits cation access to regions near the surface. The ionic conductivity of Mn oxide is strongly dependent on its crystal structure. Crystalline Mn oxide has better ionic and electronic conductivity than amorphous Mn oxide. However, amorphous Mn oxides have highly porous structures and, as such, higher surface areas so that a larger proportion of the material lies within the near surface region. [3]

Manganese oxide (MnO₂) has a number of stable crystal structures; these structures are built from MnO₆ octahedra. The stacking of MnO₆ octahedra can result in 1D, 2D, or 3D tunnel structures of various sizes. Figure 2-5 shows some Mn oxide crystal structures with open tunnels. [28] In general, specific capacitance and ionic conductivity increase with increasing tunnel size and dimensionality. Large open tunnel structures provide easy access to the bulk and provide sites for intercalation of electrolyte ions. [12,19,20,25,27] Ghodbane et al. directly compared capacitance performance for multiple Mn oxide crystal structures. Table 2-1 shows the crystal structures investigated. The results are summarized in Figure 2-6 and indicate that for crystalline Mn oxide, capacitance is strongly dependent on the ionic conductivity. [12]

Table 2-1: Mn oxide (MnO₂) crystal structures from Ghodbane et al. [12,25]

Type	Crystal Structure	Tunnel	Size (nm)
Pyrolusite	Rutile structure, $P42/mnm$	1 x 1	0.23 x 0.23
Ramsdellite	Orthorhombic, $Pnma$	1 x 2	0.23 x 0.46
Cryptomelane	Tetragonal, $I4/m$	2 x 2	0.46 x 0.46
Ni-todorokite	Monoclinic $P2/m$	3 x 3	0.69 x 0.69
OMS-5	Monoclinic $C2/m$	4 x 2	0.92 x 0.92
Birnessite	Birnessite, $R\bar{3}m$	Interlayer distance	0.7

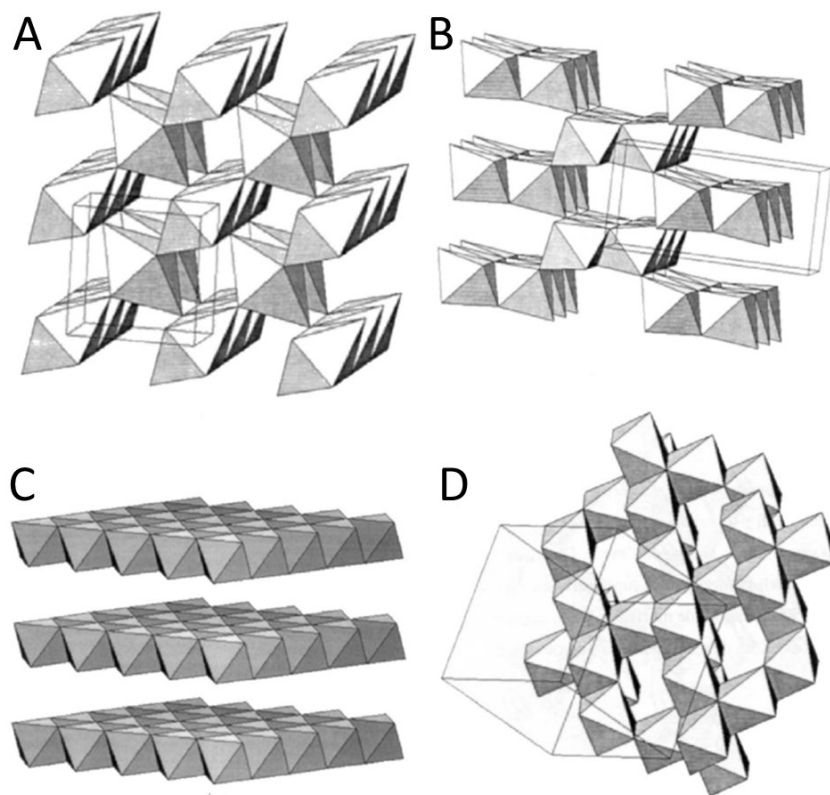


Figure 2-5: Schematic representation of Mn oxide (MnO₂) crystal structures: (A) pyrolusite β-MnO₂, (B) ramsdellite, (C) birnessite δ-MnO₂, and (D) spinel λ-MnO₂. [28]

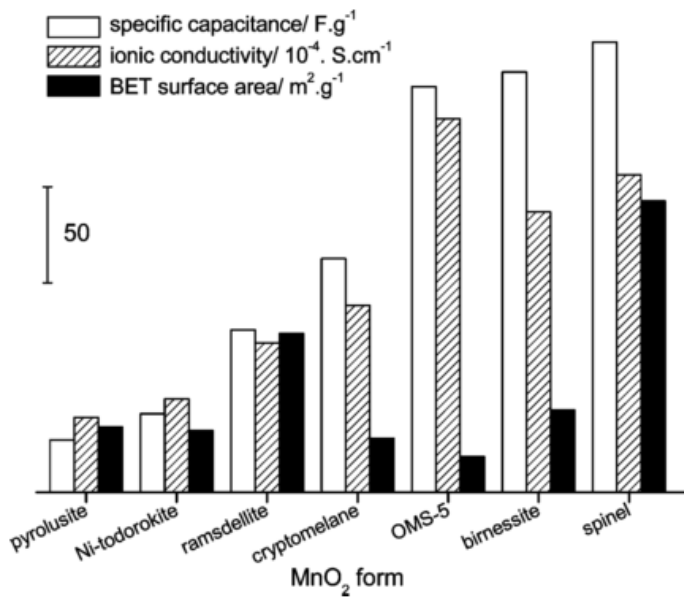


Figure 2-6: Capacitance, ionic conductivity, and specific surface area for various Mn oxide crystal structures, from Ghodbane et al. [12]

Capacitance values reported in the literature for Mn oxides are variable; most report values around 100-300 F/g. [3,25] Values approaching the theoretical capacitance are attainable through very low mass loading. Devaraj and Munichandraiah reported a specific capacitance of 1330 F/g for electrodeposited MnO₂ at a mass loading of 0.03 mg/cm². When the mass loading was increased to 0.9 mg/cm², the capacitance dropped to 300 F/g. [31] Thin layers of Mn oxide benefit from short diffusion paths for electrolyte ions, reduced electrical resistance, and high surface area to volume ratios. Poor ionic and electrical conductivity and a reduced surface area to volume ratio for thicker layers are responsible for the deviation from the theoretical capacitance. [3,25,31] For commercial applications, it is necessary to find a balance between mass loading and specific capacitance in order to maximize device performance.

Recent trends in Mn oxide ECs have been towards the fabrication of nanostructured Mn oxides. Many methods have been developed to obtain nanostructured Mn oxide; some of the structures obtained are nanosheets, [32-35] nanowires, [36-40] and nanorods, [41-45] among others. [3] By bringing feature size down to the nanoscale, enhanced surface area and reduced diffusion path lengths can be retained while simultaneously achieving high degrees of mass loading. [46]

2.2.2.3 Other oxides

The oxides of many other transition metals (e.g., Co, Ni, V, Fe, Sn) have been investigated in the literature, with varying degrees of success. Some of these oxides exhibit very high theoretical capacitance values (3750 F/g for NiO), but suffer from limitations such as high resistivity or a small potential window. Table 2-2 shows a comparison of some metal oxides. [3] Of the transition metal oxides, the oxides of Mn and Ru have the best combination of properties for EC applications.

Some mixed metal oxides have been investigated as electrochemical capacitors, many with good capacitive performance. [3,25,47-50] By combining Ru oxide with a cheap metal oxide, utilization of Ru can be improved to help reduce cost. [3] The poor electronic conductivity of Mn oxide can be improved through the addition of oxides of other transition metals such as Pb, V, Ru, Mo, or Al. Incorporation of other elements into the Mn oxide structure improves the electronic conductivity by introducing defects and additional charge carriers. [25,49,50]

Table 2-2: Comparison of various metal oxides. [3]

Material	Capacitance (F/g)	Challenges/advantages for EC application
MnO ₂	100-300	Reversible redox behavior and high theoretical capacitance, but dissolves during cycling and has poor conductivity. Many novel morphologies and composites have been developed to combat these problems.
RuO ₂	700-900	Good conductivity, cyclability, and capacitance. High cost limits wide spread use.
Co ₃ O ₄	100-600	Good reversibility, cyclability, and conductivity. Performance is strongly dependent on morphology.
NiO	150-700	Large theoretical capacitance, but has high resistivity and poor cyclability. Performance can be improved with the introduction of other transition metal oxides.
SnO ₂	70-285	Low specific capacitance in crystalline state and has a small potential window. Composites with other metal oxides can improve the potential window.
Fe ₂ O ₃ /Fe ₃ O ₄	100	Large potential window, but suffers from very poor conductivity and cyclability.

2.2.3 Conducting polymers

Conducting polymers (CPs) possess many properties beneficial to electrochemical capacitor applications, such as low cost, high conductivity, large potential window, and adjustable properties through chemical modification. [3,51] The conductivity of poly(3,4-ethylenedioxythiophene) (PEDOT) depends on a number of factors including dopant concentration and fabrication method. The conductivity of PEDOT is typically on the order of 100 S/cm. [52] Charge storage in conducting polymers is Faradaic, relying on the doping/dedoping of counter ions along the polymer chains. Charge storage in CPs is highly reversible and occurs at the surface and throughout the bulk. [3,51] CPs have good rate capability, due to their high conductivity and fast redox reactions. Typical capacitance values for CPs lie between 100 and 500 F/g. Swelling and shrinking during cycling is very problematic for many CPs; mechanical degradation leads to poor cyclability. Some CPs that have been investigated as ECs are: (PEDOT), [3,49,51,53-57] polypyrrole (PPy), [3,51,58,59] and polyaniline (PANI). [3,51,60] Because redox reactions are responsible for charge storage, some CPs exhibit nearly ideal CV curves while others exhibit significant redox peaks. [51]

2.2.3.1 Poly(3,4-ethylenedioxythiophene) (PEDOT)

Literature on PEDOT has grown rapidly over recent years because of its desirable properties. Compared with other conducting polymers PEDOT is highly conductive, has a wide potential window, has high surface area, and has high charge mobility. [51] PEDOT has been shown to have very good stability against oxidation and thermal degradation; properties that are not common in CPs. [57] Although PEDOT has a fairly low specific capacitance (90 F/g), its film forming properties and low solubility in aqueous solutions make it an excellent material for composite ECs. [51]

2.2.4 Composites

Many recent developments in ECs have been from the use of composite materials. Composites can provide improved capacitive performance through synergetic effects between two or more different materials. [3] When designing composite materials, the goal is to minimize the effects of each material's detrimental properties while maximizing their beneficial ones.

Nanoscale carbon (e.g., graphene and carbon nanotubes) and nanoscale Mn oxide composites are one common composite material that exhibits improved capacitive performance through synergetic effects. [61-66] The nanoscale carbon provides a highly conductive support to improve kinetics and rate capability, while the Mn oxide provides increased capacitance. Similar composites utilizing Ru oxide and conductive supports of carbon and/or CP have been investigated, with the aim of reducing the use of Ru while maintaining high capacitance values. [3,19]

Coating of Mn oxide electrodes with PEDOT has been shown to improve both specific capacitance and stability with cycling. The PEDOT coating provides improved electron conduction to the Mn oxide, increasing the amount of electrochemically active material. Dissolution during cycling is reduced by the PEDOT coating, since the polymer acts as a barrier between the Mn oxide and the electrolyte while still allowing cation access for charge storage. [49,53]

2.3 Electrochemical Synthesis

A wide variety of techniques have been used to synthesize materials for ECs including chemical techniques, [60,61,67,68] hydrothermal methods, [43,48,54,58,66,69] electrochemical deposition, [36,38,39,41,44,45,47,55,59,62-64,70-78], and other methods [34,42,50,79-83]. Of these techniques, electrodeposition is the most widely used. Electrodeposition is the process of depositing a coating onto a substrate from solution, using an externally supplied voltage to supply electrons. A two electrode or three electrode set-up can be used for electrodeposition. The working electrode is the substrate for electrodeposition and is usually a conductive material.

Electrodeposition is a simple and inexpensive technique and is used in a wide variety of applications. Electrodeposited films are conformal, allowing for uniform coating of complex shapes. The properties of a deposited film can be altered by changing deposition conditions such as solution composition, stir rate, time, temperature, and current/voltage. The large number of deposition conditions that can be altered allows for fine tuning of deposit properties like composition, morphology, and mass loading. [84]

The kinetics and thermodynamics of an electrodeposition reaction can be controlled through the applied current and voltage, respectively. In galvanostatic deposition, the rate of reaction can be carefully controlled. However, the cell potential can drift as the reaction proceeds and this may lead to side reactions, yielding multiple phases in the deposit. Potentiostatic deposition is much more likely to yield a single phase deposit, but the reaction rate is inconsistent. In a typical potentiostatic deposition, the cell current decays quickly as reactants are consumed at the electrode surface. [84] Some other methods used for electrodeposition are cyclic voltammetry, [62,73,76], chronoamperometry, [85] and pulsed techniques [44].

2.3.1 Electrodeposition of Mn oxide

Electrodeposition is a widely used method of preparing Mn oxide for ECs. Mn oxide can be electrodeposited either anodically or cathodically. Anodic deposition is the more popular method of deposition and occurs via the following reaction: [25]



Many studies, including previous work by our research group, [49,53,86-88] have been conducted exploring the effects of anodic deposition conditions on deposit properties such as oxidation state, morphology, and surface area. Refinement of anodic deposition techniques for Mn oxide has been aimed largely at increasing surface area through the growth of micro- and nano-scale features. [25] Figure 2-7 shows some morphologies that can be obtained through anodic electrodeposition of Mn oxide. [25] Figure 2-7A shows a 3D fibrous network, the most common morphology obtained from potentiostatic and galvanostatic methods. Fibrous micro- and nano-scale rods, fibers, and interconnected sheets can be grown through anodic deposition using either dilute electrolytes (Figure 2-7B-D) or through cyclic voltammetry (Figure 2-7E,F).

The structures shown in Figure 2-7 were obtained using template-free techniques. Mn oxide rods have also been grown using template assisted techniques like anodic Al oxide (AAO) or lyotropic liquid crystalline (LLC) phases. Deposits grown with template assisted techniques have high surface morphologies which are good for application as ECs. However, these techniques are typically much more complicated and expensive than template-free methods. [25]

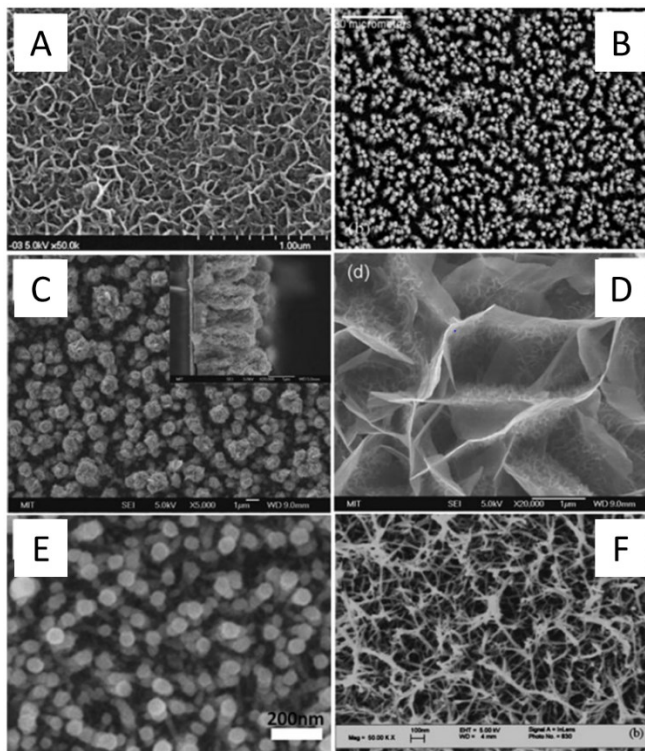


Figure 2-7: Mn oxide morphologies obtained through anodic electrodeposition. (A) 3D fibrous network, (B,C) Mn oxide rods grown from a dilute electrolyte, (D) fibrous surface of a rod from (C), (E) Mn oxide rods grown by CV, (F) interconnected nanosheets grown by CV. [25]

Cathodic deposition of Mn oxide can occur through two different mechanisms. The first mechanism involves electrogeneration of hydroxide ions from the consumption of H⁺ ions or electrolysis of water. Mn hydroxide then deposits via the following reaction:



Thermal annealing can then be used to convert Mn(OH)₂ into Mn oxide by a dehydration process. The second cathodic deposition method involves the reduction of Mn(VII) ions provided by permanganate salts. The deposition reaction occurs as follows: [25]



This reaction has been used to grow nanostructured Mn oxide by galvanostatic and pulsed electrodeposition. Deposit properties like composition and morphology are strongly dependent on the concentration of MnO₄⁻. Dilute solutions yield fibrous films with a birnessite crystal structure, while more concentrated solutions produce amorphous deposits. [25]

2.3.2 Electropolymerization of PEDOT

Electrodeposition of PEDOT can be realized through electropolymerization of EDOT from solution. Due to the low solubility of EDOT in aqueous solutions, surfactants are commonly used to improve the properties of EDOT in aqueous solutions. [89,90] Electropolymerization begins with oxidized monomers diffusing towards the electrode interface, where oligomerization takes place. Once a high density of oligomers is reached, clusters are deposited and create growing nuclei, forming PEDOT. [91] Deposition conditions strongly affect the properties of an electrodeposited PEDOT film. The conductivity, stability, and optical properties can be easily modified by varying deposition conditions like applied potential and electrolyte composition. [92]

2.3.3 Nucleation and growth

The mechanism of nucleation and growth for an electrodeposition reaction can greatly affect the morphology of a deposit. Electrochemical deposition is a good technique for the study of early stage nucleation and growth because electrodeposition allows for measurements of current-time or overpotential-time relationships. [93] Using these measured relationships, information on the mechanism of nucleation can be derived. Nucleation can occur progressively or instantaneously.

Instantaneous nucleation occurs when all of the active sites available are occupied very quickly; these nuclei then grow with no more nucleation occurring. Progressive nucleation occurs when nuclei are continuously formed during the entire deposition time. [94] Schematic diagrams for instantaneous and progressive nucleation are shown in Figure 2-8. [95] Progressive nucleation occurs on a larger number of active sites than instantaneous nucleation, resulting in more compact grains. Progressive nucleation allows for nucleation on the surface of previously deposited nuclei. [93] Some efforts have been made to try and relate deposition rate to the nucleation mechanism, but there currently is no consensus. [93-97]

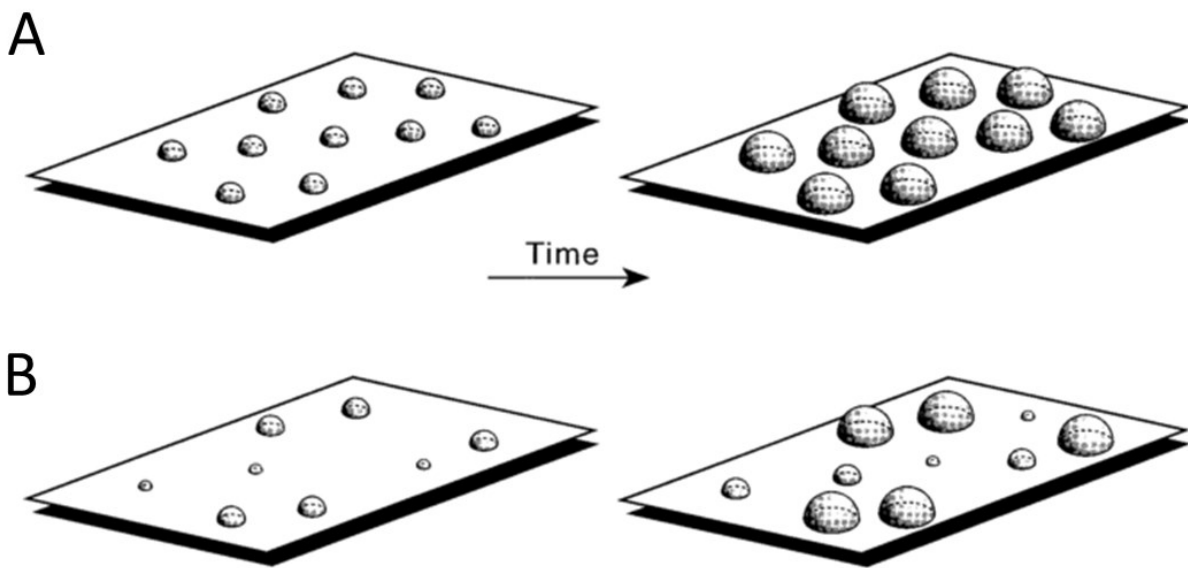


Figure 2-8: Schematic of (A) instantaneous, and (B) progressive nucleation mechanisms. [95]

Homogeneous growth occurs by two mechanisms, dominated by the kinetics of the system. Step propagation is a 2D growth mechanism and occurs when diffusion rates are sufficiently high. Growth through step propagation occurs because growth along the edges of a flat surface is thermodynamically favorable, as it minimizes total surface energy. 2D island growth occurs when diffusion is too slow to facilitate step propagation. Limited diffusion causes clustering of atoms on the surface. Sufficiently large clusters become stable and form 2D islands. [98]

For heterogeneous film growth, the mechanism is dependent on the balance between two energy terms, surface energy and elastic energy from lattice mismatch between the substrate and deposit. The first two models assume no lattice mismatch between substrate and deposit; these

models are the Frank-van der Merwe model and the Volmer-Weber model. Schematics of these models are shown in Figure 2-9. [99] If the surface energy of the substrate is equal to or higher than the sum of the surface energies of the interface and the film, the Frank-van der Merwe model applies. This model results in layer by layer growth. Volmer-Weber growth occurs in the opposite case, when the surface energy of the substrate is less than the sum of the surface energies of the interface and the film. Both of these models are driven by the reduction in surface energy. [98]

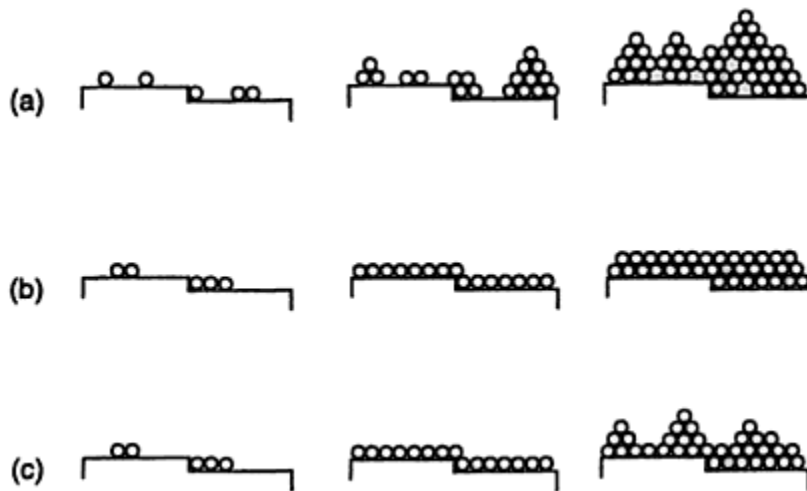


Figure 2-9: Heterogeneous growth mechanisms: (a) Volmer-Weber (b) Frank-van der Merwe, and (c) Stranski-Krastanov. [96]

The Frank-van der Merwe and Volmer-Weber models assume a perfect lattice match between the film and substrate. In reality, this condition is rarely met. For most cases of heterogeneous film growth, the elastic energy should be considered; this is done with the Stranski-Krastanov model. This model assumes that the film will completely wet the surface, like it does in Frank-van der Merwe growth. Initial growth occurs layer by layer and is dominated by the surface energy term. As a film grows thicker, elastic energy accumulates. Once the elastic energy becomes larger than the surface energy, growth switches to an island growth mechanism. [98]

2.4 Characterization Techniques

2.4.1 Materials techniques

Materials techniques are used to characterize morphology, composition, chemical state, and crystal structure.

2.4.1.1 Scanning electron microscopy

Scanning electron microscopy (SEM) is a versatile technique used in materials science. Because SEM involves the movement and detection of electrons, it must be conducted under vacuum as air particles interfere with the movement of electrons. To image a sample in the SEM, it must be conductive. Non-conducting samples can be coated with a conductive material such as C or Au to allow for imaging. SEM is achieved by focusing electrons into a sharp beam and scanning that beam across a surface. When the electron beam hits the sample, a number of interactions occur that eject electrons and photons. As the beam is scanned across the sample surface, ejected electrons are collected for each individual point on the sample. The number of detected electrons for each point corresponds to the brightness of that point; areas that emit a large number of electrons appear brighter than areas that emit only a few electrons. [98,100]

A number of different types of electrons are emitted when an electron beam interacts with a sample. Depending on the type of electron detected, different contrast effects are observed. Secondary electrons (SE) are emitted when the electron beam interacts with the electron shell of an atom, knocking electrons out of the sample. SE are fairly low energy (2-5 eV) and give information about the topography of a sample. Backscattered electrons (BSE) are emitted when the incident beam interacts with the nucleus of a sample atom. BSE are high energy (1-20 keV) and give atomic number contrast; atoms with high atomic numbers backscatter electrons more effectively than low atomic number atoms. Information on the composition of a sample can be obtained through spectroscopy of the emitted x-rays; this technique is known as energy dispersive x-ray spectroscopy (EDX). [98,100]

The resolution of an SEM image is usually 1-50 nm; some specialized instruments can achieve resolutions on the order of angstroms. The resolution is dependent on a large number of factors including the type of signal detected, spot size, accelerating voltage, beam current, and sample material. High resolution images of many materials can be obtained through the use of a field-emission electron source coupled with an in-lens detector. [100]

2.4.1.2 Transmission electron microscopy

Transmission electron microscopy (TEM) is another powerful technique in material science. TEM analysis allows for high resolution imaging; some instruments are capable of resolutions on

the order of 50 pm. TEM images are formed by accelerating an electron beam through a sample and forming an image with the transmitted beam; this is known as bright field imaging. Electron diffraction patterns can be obtained from very small areas, allowing for crystallographic analysis of small features. If a section of a diffraction pattern is used to form an image, areas meeting that specific diffraction condition will show up bright. This is known as a dark field image and is useful for determining grain size. EDX and electron energy loss spectroscopy (EELS) are TEM techniques that give information on the composition of a sample. [98]

As with SEM, TEM must be conducted within a vacuum. The main limitation associated with TEM is that samples must be electron transparent. This means samples should be no more than 200 nm thick; even thinner samples are needed if high resolution images are required.

2.4.1.3 X-ray photoelectron spectroscopy

X-ray photoelectron spectroscopy (XPS) is a powerful technique providing surface compositional and chemical state information. To perform XPS, the sample is bombarded with a beam of x-rays that has a narrow energy range. These x-rays are absorbed by the electrons associated with the atoms in the sample and some of the electrons are then ejected from the sample surface; these electrons are called photoelectrons. The energy of the ejected electrons is measured and gives information on atomic species and the types of bonds present in the sample. Photoelectrons are low energy and are only able to escape from the near surface regions of a sample. As such, XPS is a surface technique, with information collected only from the top few nanometers of the sample. [98]

2.4.2 Electrochemical techniques

In order to determine the performance of an EC, a number of electrochemical techniques are employed. Some important properties measured through these techniques are capacitance, rate capability, cycling stability, and energy/power density.

2.4.2.1 Cyclic voltammetry

Cyclic voltammetry (CV) is a versatile technique in the field of electrochemistry. Curves obtained through CV are referred to as voltammograms. The size and shape of a voltammogram gives information on redox reactions that occur at the electrode. For ECs, CV is commonly used

to measure capacitance. The capacitance can be calculated from a cyclic voltammogram using the following equation: [101]

$$C = Q/\Delta E \quad (1-8)$$

where C is the capacitance, Q is the total anodic or cathodic charge transferred, and ΔE is the potential window. To calculate the capacitance from a voltammogram, the charge transferred during a cathodic or anodic sweep is summed and divided by the potential window. An ideal capacitor experiences a linear relation between stored charge (Q) and the potential of the device (ΔE). If a capacitor is ideal it will exhibit a constant current over the entire voltage range used, giving rise to a rectangular voltammogram. An idealized voltammogram is shown in Figure 2-10. [51]

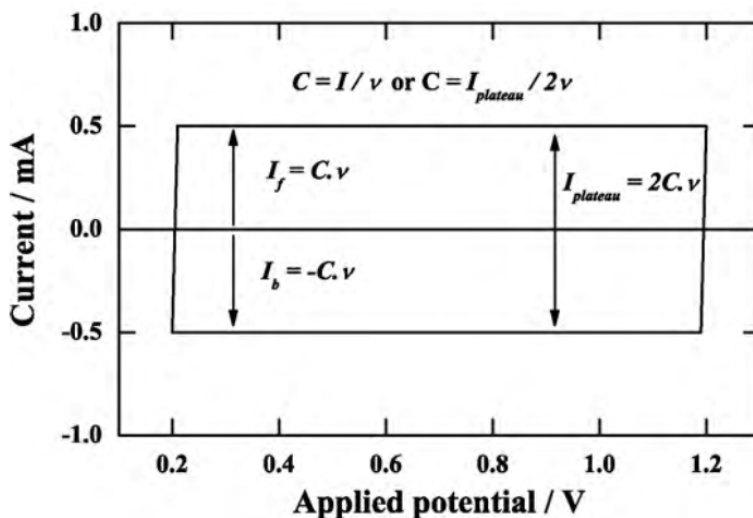


Figure 2-10: Schematic representation of an ideal cyclic voltammogram. C is capacitance, I_f is the forward sweep current, I_b is the backward sweep current, and v is the scan speed. [51]

To perform this technique, a linearly changing voltage is applied to an electrode and the resultant current is measured. The voltage is swept between an upper limit and a lower limit, which is referred to as the voltage or potential window. Depending on the system, the shape of the voltammogram can vary with the speed at which the voltage is changed (scan rate). This is because the rate of electrochemical processes can be limited by the kinetics of the system. It is possible to move the system far from equilibrium at a sufficiently high scan rate. [101]

2.4.2.2 Galvanostatic cycling

Galvanostatic cycling (GSC) is another technique used to determine the capacitance of an EC. GSC is conducted by applying a constant current (I) until an upper potential limit is reached. The current is then reversed and discharge takes place until the lower potential limit is achieved. GSC results are plotted as potential vs. time. The voltage window used for GSC is usually the same as the voltage window used for CV. Using the time taken for a full charge/discharge cycle (t), the capacitance can be calculated with the following equation: [71]

$$C = It/2\Delta E \quad (2-9)$$

An ideal capacitor experiences a linearly increasing potential during GSC (dV/dt is constant), giving rise to a triangular shaped curve. To determine the capacitance from a GSC curve, the time for one full charge and discharge cycle is measured and put into Equation 2-9. It is possible to calculate the capacitance from any sized portion of the GSC curve; however, selecting a small section of the curve can lead to misleading results. A schematic of an ideal GSC curve is shown in Figure 2-11. [39] It is common to normalize the applied current in terms of mass (A/g) or area (A/cm²).

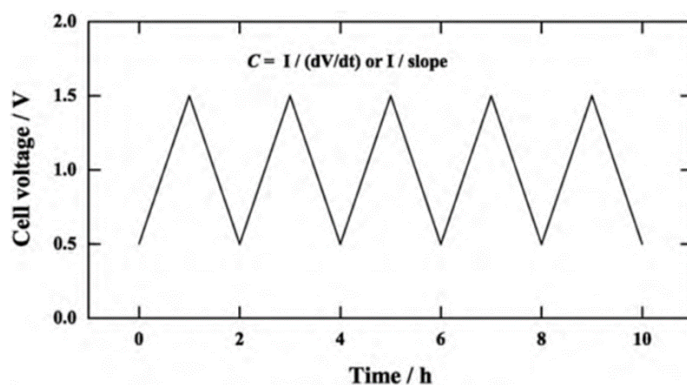


Figure 2-11: Schematic representation of a GSC curve for an ideal capacitor. C is the capacitance, V is the voltage, and t is the time. [51]

2.4.2.3 Electrochemical impedance spectroscopy

Electrochemical impedance spectroscopy (EIS) is an electrochemical technique used to study the electrochemical processes taking place at an electrode/electrolyte interface. EIS is performed by imposing a small alternating current (AC) signal on a finite direct current (DC). The frequency is then varied and the resulting impedance values are measured. Impedance results are plotted as

the imaginary component of the impedance (Z_i) vs. the real component (Z_r); this is called a Nyquist plot. A Nyquist plot can be used to determine a number of electrochemical parameters such as solution resistance, electrode kinetics, and capacitance. To relate the Nyquist plot to these electrochemical parameters, it is necessary to model an equivalent circuit to represent the dynamic characteristics of the cell. [101]

2.5 Previous Work in the Ivey Research Group

2.5.1 Electrodeposition of Mn oxide for electrochemical capacitors

The first work on Mn oxide ECs by Babakhani and Ivey was published in 2010. In this work, Mn oxide coatings were anodically electrodeposited onto Au coated Si from two different solutions, i.e., 0.01 M MnSO_4 (manganese sulfate) and 0.01 M $\text{Mn}(\text{CH}_3\text{COO})_2$ (manganese acetate). Depositions were conducted at 60°C for 10 min, with current densities ranging from 5 to 30 mA/cm^2 . The electrolyte pH was adjusted to 6.5 and agitation was supplied by a magnetic stir bar rotating at 300 RPM. After deposition, samples were dried in air at 100°C for 1 h. [87]

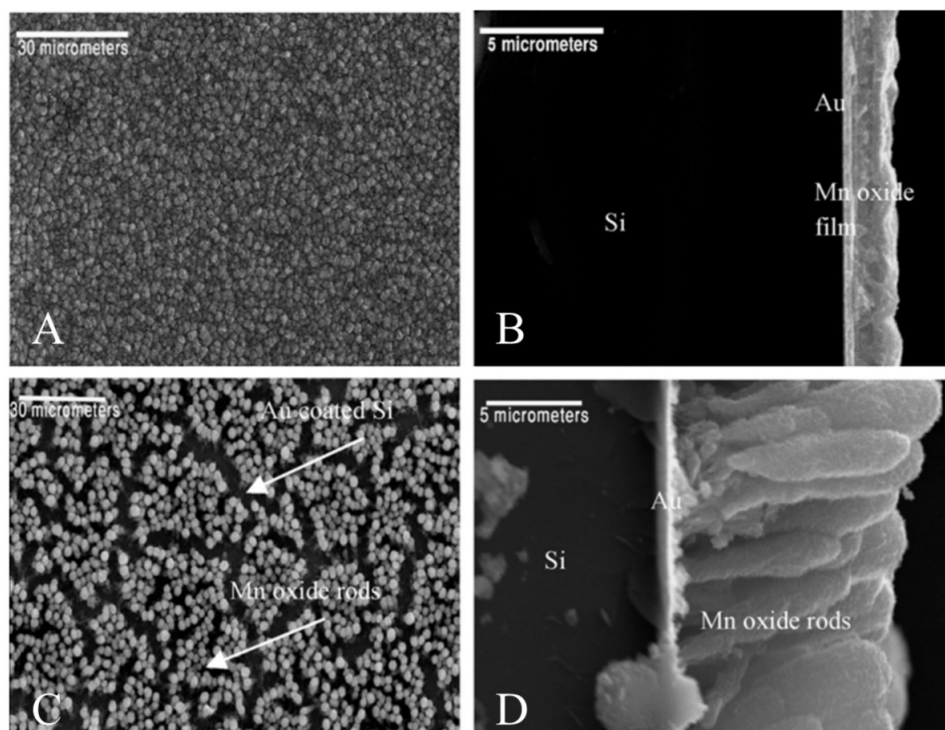


Figure 2-12: SEM SE micrographs of Mn oxide deposits prepared from (A,B) 0.01 M MnSO_4 at 30 mA/cm^2 and (C,D) 0.01 M $\text{Mn}(\text{CH}_3\text{COO})_2$ at 5 mA/cm^2 . [87]

Deposits obtained from MnSO_4 solutions were continuous porous layers, which is typical for electrodeposited Mn oxide. Deposits obtained from $\text{Mn}(\text{CH}_3\text{COO})_2$ solutions resulted in high surface area rod-like structures. The microstructures of these deposits are shown in Figure 2-12. TEM electron diffraction revealed that the Mn oxide rods were nanocrystalline and had a NaCl crystal structure (FCC with space group corresponding to $Fm\bar{3}m$) with a lattice parameter of 0.445 nm. Peak splitting of the Mn 2p XPS spectrum was used to determine that the valence of Mn in the deposit was 4+ and/or 3+. The best capacitive performance was obtained for deposits prepared from 0.01 M $\text{Mn}(\text{CH}_3\text{COO})_2$ at 5 mA/cm². For these deposits, the measured capacitance was 185 F/g at a scan speed of 5 mV/s. After 250 cycles the capacitance dropped by 25% to 139 F/g. [87]

2.5.2 Effect of electrodeposition conditions on Mn oxide deposits

The effect of varying deposition conditions on resulting Mn oxide deposit morphology and electrochemical performance were investigated using SEM, CV, and EIS. Depositions were done on Au coated Si. After deposition, deposits were dried in air at 100°C for 1 h. The conditions that were varied were current density, solution concentration, solution temperature, solution pH, and supersaturation ratio. Through varying these conditions, a number of Mn oxide nanostructures were obtained including thin sheets, rods, continuous coatings, and particles. Table 2-3 shows a summary of some electrodeposited Mn oxide nanostructures from [88]. All deposits presented in [88] were indexed to an antiferite-type crystal structure. Atomic absorption spectroscopy was used to determine the amount of Mn dissolution during cycling. The amount of Mn dissolution was dependent on deposit morphology, with rods experiencing more dissolution than thin sheets. [88]

Table 2-3: Capacitance results for various Mn oxide nanostructures. Cycled in 0.5 M Na₂SO₄ at 20 mV/s. [88]

Specific capacitance after 2nd cycle (F/g)	Capacitance decrease after 250 cycles (%)	Deposit morphology	Deposition conditions
230	12	Thin sheets	60°C, 0.01 M Mn(CH ₃ COO) ₂ , 1 mA/cm ² , pH 7.5
185	25	Rods	60°C, 0.01 M Mn(CH ₃ COO) ₂ , 5 mA/cm ² , pH 7.5
145	41	Continuous coating	60°C, 0.03 M Mn(CH ₃ COO) ₂ , 5 mA/cm ² , pH 7.5
170	19	Oxide protrusions and thin sheets within them	60°C, 0.01 M Mn(CH ₃ COO) ₂ , 5 mA/cm ² , pH 5
123	39	Small oxide particles	25°C, 0.01 M Mn(CH ₃ COO) ₂ , 5 mA/cm ² , pH 7.5

2.5.3 Improved capacitive behavior of Mn oxide/ PEDOT electrodes

Composite electrodes of Mn oxide/ PEDOT were prepared on Au coated Si via two methods: a two-step sequential method and a one-step codeposition method. For sequential deposition, Mn oxide rods were first deposited from a solution of 0.01 M Mn(CH₃COO)₂ at 60°C for 10 min at current densities ranging from 5 to 30 mA/cm². The Mn oxide deposit was then coated with PEDOT from a solution containing 0.08 M EDOT, 0.2 M lithium tetrafluoroborate (LiBF₄) and 0.14 M sodium dodecyl sulfate (SDS). LiBF₄ was used as the dopant and SDS improved the solubility of EDOT in the aqueous solution. Electropolymerization was conducted at a constant potential of 1 V vs. a saturated calomel electrode (SCE) for 10 to 60 s. One-step coelectrodeposition was conducted at current densities ranging from 10 to 30 mA/cm² using a solution containing 0.01 M Mn(CH₃COO)₂, 0.08 M EDOT, 0.2 M LiBF₄ and 0.14 M SDS. After deposition, electrodes were dried in air for 1 h at 100°C. [53]

Deposits obtained through one-step electrodeposition did not have rod-like structures, but did exhibit fairly high capacitance values (195 F/g at 20 mV/s). Coaxial core/shell rods obtained through two step deposition exhibited excellent capacitive performance. At a scan rate of 20 mV/s, the coaxial rods had a capacitance of 285 F/g and experienced only an 8% capacitance

decrease over 250 cycles. Atomic absorption measurements showed that the PEDOT coating successfully prevented dissolution of Mn oxide during cycling, improving capacitance retention. TEM diffraction was used to match the deposit crystal structure to a NaCl- type crystal structure with a lattice parameter of 0.445 nm. The Mn 2p XPS spectrum showed that the oxidation state of the deposit is a mixture of 3+ and 4+. [53]

CV curves for deposits with and without PEDOT are shown in Figure 2-13. For deposits without PEDOT, anodic and cathodic peaks are observed during cycling. These peaks result from redox transitions that occur due to ion exchange during cycling. CV curves for deposits with PEDOT are close to rectangular, indicating good capacitive performance. With the application of PEDOT, only small anodic and cathodic redox waves were observed during cycling. [53]

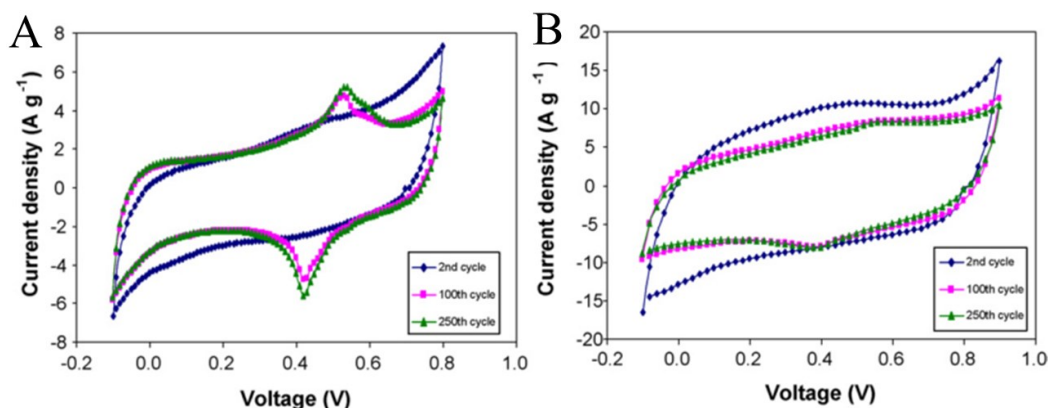


Figure 2-13: CV curves for deposits (A) without PEDOT, and (B) with PEDOT. Cycling was done in 0.5 M Na₂SO₄ at 20 mV/s. Potential is vs. SCE. [53]

2.5.4 Electrochemical behavior of Co doped Mn oxide

Co doped Mn oxide deposits were prepared from solutions containing 0.01 M Mn(CH₃COO)₂ and Co sulphate (CoSO₄) at concentrations of 0.001, 0.005 and 0.01 M. Depositions were conducted on Au coated Si at 60°C at current densities ranging from 5 to 30 mA/cm² for 300 s. Using the same procedure described in Section 2.5.3, Mn-Co oxide rods were coated with PEDOT. The crystal structure of the Mn-Co oxide deposits was matched with an antiferrotype crystal structure. XPS analysis of the Mn 3s and Co 2p spectra indicated that Mn was present as Mn⁴⁺ and Co was present as a mixture of Co²⁺ and Co³⁺. An anomalous trend in capacitance with scan rate was observed. Normally the highest capacitance values are measured

at slow scan rates, as slow scan rates give sufficient time for charge storage reactions to occur. Capacitances were measured at scan rates varying between 5 and 1000 mV/s. The highest capacitance values were obtained at a scan rate of 100 mV/s (213 F/g for Mn-Co oxide and 310 F/g for Mn-Co oxide/ PEDOT). [49]

2.6 References

- [1] R. Ko and M. Carlen, “Principles and applications of electrochemical capacitors,” *Electrochem. commun.*, vol. 45, pp. 2483–2498, 2000.
- [2] M. Winter and R. Brodd, “What are batteries, fuel cells, and supercapacitors?,” *Chem. Rev.*, no. 104, pp. 4245–4269, 2004.
- [3] G. Wang, L. Zhang, and J. Zhang, “A review of electrode materials for electrochemical supercapacitors,” *Chem. Soc. Rev.*, vol. 41, no. 2, pp. 797–828, Jan. 2012.
- [4] A. S. Aricò, P. Bruce, B. Scrosati, J. Tarascon, W. V. A. N. Schalkwijk, U. De Picardie, J. Verne, and C. Umr-, “Nanostructured materials for advanced energy conversion and storage devices,” *Nat. Mater.*, vol. 4, May, 2005.
- [5] L. L. Zhang and X. S. Zhao, “Carbon-based materials as supercapacitor electrodes,” *Chem. Soc. Rev.*, vol. 38, no. 9, pp. 2520–31, Sep. 2009.
- [6] C. Liu, F. Li, L.-P. Ma, and H.-M. Cheng, “Advanced materials for energy storage,” *Adv. Mater.*, vol. 22, no. 8, pp. E28–62, Feb. 2010.
- [7] P. Simon and Y. Gogotsi, “Materials for electrochemical capacitors,” *Nat. Mater.*, vol. 7, no. 11, pp. 845–54, Nov. 2008.
- [8] H. V. Helmholtz, *Ann. Phys.*, vol. 89, p. 21, 1853.
- [9] E. Frackowiak and F. Béguin, “Carbon materials for the electrochemical storage of energy in capacitors,” *Carbon N. Y.*, vol. 39, no. 6, pp. 937–950, May 2001.
- [10] B. E. Conway, V. Birss, and J. Wojtowicz, “The role and utilization of pseudocapacitance for energy storage by supercapacitors,” *J. Power Sources*, vol. 66, no. 1–2, pp. 1–14, May 1997.
- [11] B. E. Conway, “TECHNICAL PAPERS’ ELECTROCHEMICAL SCIENCE AND TECHNOLOGY Transition from ‘Supercapacitor’ to ‘Battery’ Behavior in Electrochemical Energy Storage,” *J. Electrochem. Soc.*, vol. 138, no. 6, 1991.

- [12] O. Ghodbane, J.-L. Pascal, and F. Favier, "Microstructural effects on charge-storage properties in MnO₂-based electrochemical supercapacitors," *ACS Appl. Mater. Interfaces*, vol. 1, no. 5, pp. 1130–9, May 2009.
- [13] M. D. Stoller, S. Park, Y. Zhu, J. An, and R. S. Ruoff, "Graphene-based ultracapacitors," *Nano Lett.*, vol. 8, no. 10, pp. 3498–502, Oct. 2008.
- [14] Y. Zhu, S. Murali, M. D. Stoller, K. J. Ganesh, W. Cai, P. J. Ferreira, A. Pirkle, R. M. Wallace, K. A. Cychosz, M. Thommes, D. Su, E. A. Stach, and R. S. Ruoff, "Carbon-Based Supercapacitors," *Science*, vol. 332, no. June, pp. 1537–1542, 2011.
- [15] E. Frackowiak, "Carbon materials for supercapacitor application," *Phys. Chem. Chem. Phys.*, vol. 9, no. 15, pp. 1774–85, Apr. 2007.
- [16] R. Ryoo, S. H. Joo, M. Kruk, and M. Jaroniec, "Ordered Mesoporous Carbons," *Adv. Mater.*, vol. 13, no. 9, pp. 677–681, May 2001.
- [17] Y. Wang, Z. Shi, Y. Huang, Y. Ma, C. Wang, M. Chen, and Y. Chen, "Supercapacitor Devices Based on Graphene Materials," *J. Phys. Chem. C*, vol. 113, no. 30, pp. 13103–13107, Jul. 2009.
- [18] H. Jiang, P. S. Lee, and C. Li, "3D carbon based nanostructures for advanced supercapacitors," *Energy Environ. Sci.*, vol. 6, no. 1, p. 41, 2013.
- [19] X. Zhao, B. M. Sánchez, P. J. Dobson, and P. S. Grant, "The role of nanomaterials in redox-based supercapacitors for next generation energy storage devices," *Nanoscale*, vol. 3, no. 3, pp. 839–55, Mar. 2011.
- [20] M. Toupin, T. Brousse, and D. Be, "Charge Storage Mechanism of MnO₂ Electrode Used in Aqueous Electrochemical Capacitor," *Chem. Mater.*, vol. 16, no. 9, pp. 3184–3190, 2004.
- [21] W. Sugimoto, H. Iwata, K. Yokoshima, Y. Murakami, and Y. Takasu, "Proton and electron conductivity in hydrous ruthenium oxides evaluated by electrochemical impedance spectroscopy: The origin of large capacitance," *J. Phys. Chem. B*, vol. 109, pp. 7330–7338, 2005.
- [22] J. P. Zheng, P. J. Cygan, and T. R. Jow, "Hydrous Ruthenium Oxide as an Electrode Material for Electrochemical Capacitors," *J. Electrochem. Soc.*, vol. 142, no. 8, pp. 2–6, 1995.
- [23] C.-C. Hu, W.-C. Chen, and K.-H. Chang, "How to Achieve Maximum Utilization of Hydrous Ruthenium Oxide for Supercapacitors," *J. Electrochem. Soc.*, vol. 151, no. 2, p. A281, 2004.

- [24] R. N. Deguzman, a Awaluddin, Y. F. Shen, Z. R. Tian, S. L. Suib, S. Ching, and C. L. Oyoung, “Electrical-Resistivity Measurements on Manganese Oxides with Layer and Tunnel Structures - Birnessites, Todorokites, and Cryptomelanes,” *Chem. Mater.*, vol. 7, no. 11, pp. 1286–1292, 1995.
- [25] W. Wei, X. Cui, W. Chen, and D. G. Ivey, “Manganese oxide-based materials as electrochemical supercapacitor electrodes,” *Chem. Soc. Rev.*, vol. 40, no. 3, pp. 1697–721, Mar. 2011.
- [26] S. Sopčić, R. Peter, M. Petravić, and Z. Mandić, “New insights into the mechanism of pseudocapacitance deterioration in electrodeposited MnO₂ under negative potentials,” *J. Power Sources*, vol. 240, pp. 252–257, Oct. 2013.
- [27] O. Ghodbane, F. Ataherian, N.-L. Wu, and F. Favier, “In situ crystallographic investigations of charge storage mechanisms in MnO₂-based electrochemical capacitors,” *J. Power Sources*, vol. 206, pp. 454–462, May 2012.
- [28] T. Brousse, M. Toupin, R. Dugas, L. Athouël, O. Crosnier, and D. Bélanger, “Crystalline MnO₂ as Possible Alternatives to Amorphous Compounds in Electrochemical Supercapacitors,” *J. Electrochem. Soc.*, vol. 153, no. 12, p. A2171, 2006.
- [29] C.-C. Ji, M.-W. Xu, S.-J. Bao, C.-J. Cai, R.-Y. Wang, and D.-Z. Jia, “Effect of alkaline and alkaline–earth cations on the supercapacitor performance of MnO₂ with various crystallographic structures,” *J. Solid State Electrochem.*, vol. 17, no. 5, pp. 1357–1368, Jan. 2013.
- [30] P. Ragupathy, H. N. Vasana, and N. Munichandraiah, “Synthesis and Characterization of Nano-MnO₂ for Electrochemical Supercapacitor Studies,” *J. Electrochem. Soc.*, vol. 155, no. 1, p. A34, 2008.
- [31] S. Devaraj and N. Munichandraiah, “High Capacitance of Electrodeposited MnO₂ by the Effect of a Surface-Active Agent,” *Electrochem. Solid-State Lett.*, vol. 8, no. 7, p. A373, 2005.
- [32] M. Kundu and L. Liu, “Direct growth of mesoporous MnO₂ nanosheet arrays on nickel foam current collectors for high-performance pseudocapacitors,” *J. Power Sources*, vol. 243, pp. 676–681, Dec. 2013.
- [33] M. Kundu, C. C. A. Ng, D. Y. Petrovykh, and L. Liu, “Nickel foam supported mesoporous MnO₂ nanosheet arrays with superior lithium storage performance,” *Chem. Commun. (Camb)*, vol. 49, no. 76, pp. 8459–61, Oct. 2013.
- [34] M. Yano, S. Suzuki, M. Miyayama, and M. Ohgaki, “Electrode properties and microstructures of MnO₂ nanosheet thin films as cathodes for electrochemical capacitors,” *Solid State Ionics*, vol. 233, pp. 32–37, Feb. 2013.

- [35] J. Xiao, S. Yang, L. Wan, F. Xiao, and S. Wang, "Electrodeposition of manganese oxide nanosheets on a continuous three-dimensional nickel porous scaffold for high performance electrochemical capacitors," *J. Power Sources*, vol. 245, pp. 1027–1034, Jan. 2014.
- [36] H. Liu, B. Lu, S. Wei, M. Bao, Y. Wen, and F. Wang, "Electrodeposited highly-ordered manganese oxide nanowire arrays for supercapacitors," *Solid State Sci.*, vol. 14, no. 7, pp. 789–793, Jul. 2012.
- [37] Z. Sun, S. Firdoz, E. Y.-X. Yap, L. Li, and X. Lu, "Hierarchically structured MnO₂ nanowires supported on hollow Ni dendrites for high-performance supercapacitors," *Nanoscale*, vol. 5, no. 10, pp. 4379–87, May 2013.
- [38] C.-L. Ho and M.-S. Wu, "Manganese Oxide Nanowires Grown on Ordered Macroporous Conductive Nickel Scaffold for High-Performance Supercapacitors," *J. Phys. Chem. C*, vol. 115, no. 44, pp. 22068–22074, Nov. 2011.
- [39] J. Duay, S. A. Sherrill, Z. Gui, E. Gillette, S. B. Lee, and U. States, "Self-Limiting Electrodeposition Properties," *ACS Nano*, vol. 7, no. 2, pp. 1200–1214, 2013.
- [40] L. Wang, D. Deng, and K. Y. S. Ng, "Facile one-step synthesis of MnO₂ nanowires on graphene under mild conditions for application in supercapacitors," *J. Mater. Sci.*, vol. 48, no. 18, pp. 6410–6417, May 2013.
- [41] T. Yousefi, A. N. Golikand, M. Hossein Mashhadizadeh, and M. Aghazadeh, "Facile synthesis of α -MnO₂ one-dimensional (1D) nanostructure and energy storage ability studies," *J. Solid State Chem.*, vol. 190, pp. 202–207, Jun. 2012.
- [42] S. Santhanagopalan, A. Balram, and D. D. Meng, "Scalable High-Power Redox Capacitors with Aligned Nanoforests of Crystalline MnO₂ Nanorods by High Voltage Electrophoretic Deposition," *ACS Nano*, vol. 7, no. 3, pp. 2114–2125, 2013.
- [43] Z. Song, W. Liu, M. Zhao, Y. Zhang, G. Liu, C. Yu, and J. Qiu, "A facile template-free synthesis of α -MnO₂ nanorods for supercapacitor," *J. Alloys Compd.*, vol. 560, pp. 151–155, May 2013.
- [44] S. H. Lee, H. Lee, M. S. Cho, J.-D. Nam, and Y. Lee, "Morphology and composition control of manganese oxide by the pulse reverse electrodeposition technique for high performance supercapacitors," *J. Mater. Chem. A*, vol. 1, no. 46, p. 14606, 2013.
- [45] S. Chen, T. Zhai, X.-H. Lu, M.-Z. Zhang, Z.-Y. Li, C.-W. Xu, and Y. Tong, "Large-area manganese oxide nanorod arrays as efficient electrocatalyst for oxygen evolution reaction," *Int. J. Hydrogen Energy*, vol. 37, no. 18, pp. 13350–13354, Sep. 2012.
- [46] J. Yang, L. Lian, H. Ruan, F. Xie, and M. Wei, "Nanostructured porous MnO₂ on Ni foam substrate with a high mass loading via a CV electrodeposition route for supercapacitor application," *Electrochim. Acta*, vol. 136, pp. 189–194, Aug. 2014.

- [47] Z. G. Ye, X. L. Zhou, H. M. Meng, X. Z. Hua, Y. H. Dong, and A. H. Zou, "The Electrochemical Characterization of Electrochemically Synthesized MnO₂-Based Mixed Oxides for Supercapacitor Applications," *Adv. Mater. Res.*, vol. 287–290, pp. 1290–1298, Jul. 2011.
- [48] P. Xu, K. Ye, D. Cao, J. Huang, T. Liu, K. Cheng, J. Yin, and G. Wang, "Facile synthesis of cobalt manganese oxides nanowires on nickel foam with superior electrochemical performance," *J. Power Sources*, vol. 268, pp. 204–211, Dec. 2014.
- [49] B. Babakhani and D. G. Ivey, "Investigation of electrochemical behavior of Mn–Co doped oxide electrodes for electrochemical capacitors," *Electrochim. Acta*, vol. 56, no. 13, pp. 4753–4762, May 2011.
- [50] J. Kang, A. Hirata, L. Kang, X. Zhang, Y. Hou, L. Chen, C. Li, T. Fujita, K. Akagi, and M. Chen, "Enhanced supercapacitor performance of MnO₂ by atomic doping," *Angew. Chem. Int. Ed. Engl.*, vol. 52, no. 6, pp. 1664–7, Feb. 2013.
- [51] G. a. Snook, P. Kao, and A. S. Best, "Conducting-polymer-based supercapacitor devices and electrodes," *J. Power Sources*, vol. 196, no. 1, pp. 1–12, Jan. 2011.
- [52] Q. Pei, G. Zuccarello, M. Ahlskog, and O. Inganäs, "Electrochromic and highly stable poly(3,4-ethylenedioxythiophene) switches between opaque blue-black and transparent sky blue," *Polymer*, vol. 35, no. 7, pp. 1347–1351, 1994.
- [53] B. Babakhani and D. G. Ivey, "Improved capacitive behavior of electrochemically synthesized Mn oxide/PEDOT electrodes utilized as electrochemical capacitors," *Electrochim. Acta*, vol. 55, no. 12, pp. 4014–4024, Apr. 2010.
- [54] S.-B. Yoon and K.-B. Kim, "Effect of poly(3,4-ethylenedioxythiophene) (PEDOT) on the pseudocapacitive properties of manganese oxide (MnO₂) in the PEDOT/MnO₂/multiwall carbon nanotube (MWNT) composite," *Electrochim. Acta*, vol. 106, pp. 135–142, Sep. 2013.
- [55] R. Liu and S. Lee, "MnO₂/poly (3, 4-ethylenedioxythiophene) coaxial nanowires by one-step coelectrodeposition for electrochemical energy storage," *J. Am. Chem. Soc.*, vol. 130, pp. 2942–2943, 2008.
- [56] K. S. Ryu, Y.-G. Lee, Y.-S. Hong, Y. J. Park, X. Wu, K. M. Kim, M. G. Kang, N.-G. Park, and S. H. Chang, "Poly(ethylenedioxythiophene) (PEDOT) as polymer electrode in redox supercapacitor," *Electrochim. Acta*, vol. 50, no. 2–3, pp. 843–847, Nov. 2004.
- [57] J. Hong, I.-H. Yeo, and W. Paik, "Conducting Polymer with Metal Oxide for Electrochemical Capacitor: Poly(3,4-ethylenedioxythiophene) RuO_x Electrode," *J. Electrochem. Soc.*, vol. 148, no. 2, p. A156, 2001.

- [58] a. Bahloul, B. Nessark, E. Briot, H. Groult, a. Mauger, K. Zaghbi, and C. M. Julien, "Polypyrrole-covered MnO₂ as electrode material for supercapacitor," *J. Power Sources*, vol. 240, pp. 267–272, Oct. 2013.
- [59] R. K. Sharma, a. C. Rastogi, and S. B. Desu, "Manganese oxide embedded polypyrrole nanocomposites for electrochemical supercapacitor," *Electrochim. Acta*, vol. 53, no. 26, pp. 7690–7695, Nov. 2008.
- [60] Y. Huo, H. Zhang, J. Jiang, and Y. Yang, "A three-dimensional nanostructured PANI/MnO_x porous microsphere and its capacitive performance," *J. Mater. Sci.*, vol. 47, no. 19, pp. 7026–7034, Jun. 2012.
- [61] L. Deng, Z. Hao, J. Wang, G. Zhu, L. Kang, Z.-H. Liu, Z. Yang, and Z. Wang, "Preparation and capacitance of graphene/multiwall carbon nanotubes/MnO₂ hybrid material for high-performance asymmetrical electrochemical capacitor," *Electrochim. Acta*, vol. 89, pp. 191–198, Feb. 2013.
- [62] L. Li, C. Chen, J. Xie, Z. Shao, and F. Yang, "The preparation of carbon nanotube/MnO₂ composite fiber and its application to flexible micro-supercapacitor," *J. Nanomater.*, vol. 2013, pp. 2–6, 2013.
- [63] Q. Cheng, J. Tang, J. Ma, H. Zhang, N. Shinya, and L.-C. Qin, "Graphene and nanostructured MnO₂ composite electrodes for supercapacitors," *Carbon N. Y.*, vol. 49, no. 9, pp. 2917–2925, Aug. 2011.
- [64] G. Yu, L. Hu, M. Vosgueritchian, and H. Wang, "Solution-processed graphene/MnO₂ nanostructured textiles for high-performance electrochemical capacitors," *Nano Lett.*, vol. 11, pp. 2905–2911, 2011.
- [65] Y. Hou, Y. Cheng, T. Hobson, and J. Liu, "Design and synthesis of hierarchical MnO₂ nanospheres/carbon nanotubes/conducting polymer ternary composite for high performance electrochemical electrodes," *Nano Lett.*, vol. 10, no. 7, pp. 2727–33, Jul. 2010.
- [66] Z. Lei, F. Shi, and L. Lu, "Incorporation of MnO₂-Coated Carbon Nanotubes between Graphene Sheets as Supercapacitor Electrode," *Appl. Mater. Interfaces*, vol. 4, pp. 1058–1064, 2012.
- [67] C. Yuan, L. Hou, L. Yang, D. Li, L. Shen, F. Zhang, and X. Zhang, "Facile interfacial synthesis of flower-like hierarchical α -MnO₂ sub-microspherical superstructures constructed by two-dimension mesoporous nanosheets and their application in electrochemical capacitors," *J. Mater. Chem.*, vol. 21, no. 40, p. 16035, 2011.
- [68] P.-C. Gao, A.-H. Lu, and W.-C. Li, "Dual functions of activated carbon in a positive electrode for MnO₂-based hybrid supercapacitor," *J. Power Sources*, vol. 196, no. 8, pp. 4095–4101, Apr. 2011.

- [69] J. C. Zhao, B. H. Tang, L. Sun, J. Zheng, J. Cao, and J. L. Xu, "Effect of loading amount on capacitance performances of MnO₂ /ordered mesoporous carbon composites," *Mater. Technol.*, vol. 27, no. 4, pp. 328–332, Sep. 2012.
- [70] L. Yuan, X. Lu, X. Xiao, T. Zhai, J. Dai, F. Zhang, B. Hu, and X. Wang, "Flexible Solid-State Supercapacitors Based on Carbon Nanoparticles / MnO₂ Nanorods Hybrid Structure," *ACS Nano*, vol. 6, no. 1, pp. 656–661, 2012.
- [71] X. Lu, D. Zheng, T. Zhai, Z. Liu, Y. Huang, S. Xie, and Y. Tong, "Facile synthesis of large-area manganese oxide nanorod arrays as a high-performance electrochemical supercapacitor," *Energy Environ. Sci.*, vol. 4, no. 8, p. 2915, 2011.
- [72] M. Yu, T. Zhai, X. Lu, X. Chen, S. Xie, W. Li, C. Liang, W. Zhao, L. Zhang, and Y. Tong, "Manganese dioxide nanorod arrays on carbon fabric for flexible solid-state supercapacitors," *J. Power Sources*, vol. 239, pp. 64–71, Oct. 2013.
- [73] Y. Zhang, J. Li, F. Kang, F. Gao, and X. Wang, "Fabrication and electrochemical characterization of two-dimensional ordered nanoporous manganese oxide for supercapacitor applications," *Int. J. Hydrogen Energy*, vol. 37, no. 1, pp. 860–866, Jan. 2012.
- [74] M. Chigane, M. Ishikawa, and M. Izaki, "Preparation of Manganese Oxide Thin Films by Electrolysis/Chemical Deposition and Electrochromism," *J. Electrochem. Soc.*, vol. 148, no. 7, p. D96, 2001.
- [75] M. Chigane and M. Ishikawa, "Manganese oxide thin film preparation by potentiostatic electrolyses and electrochromism," *J. Electrochem. Soc.*, vol. 147, no. May 2010, pp. 2246–2251, 2000.
- [76] H. Ashassi-Sorkhabi, E. Asghari, and P. La'le Badakhshan, "Potentiostatic and cyclic voltammetric deposition of nanostructured manganese oxide for supercapacitor applications," *Curr. Appl. Phys.*, vol. 14, no. 2, pp. 187–191, Feb. 2014.
- [77] X. Lang, A. Hirata, T. Fujita, and M. Chen, "Nanoporous metal/oxide hybrid electrodes for electrochemical supercapacitors," *Nat. Nanotechnol.*, vol. 6, no. 4, pp. 232–6, Apr. 2011.
- [78] J. Xu, Z. Li, D. Han, B. Deng, J. Li, and Y. Jiang, "The mechanism of specific capacitance improvement of supercapacitors based on MnO₂ at an elevated operating temperature," *Thin Solid Films*, vol. 520, no. 18, pp. 5952–5959, Jul. 2012.
- [79] M. J. Tadjer, M. a. Mastro, J. M. Rojo, A. B. Mojena, F. Calle, F. J. Kub, and C. R. Eddy, "MnO₂-Based Electrochemical Supercapacitors on Flexible Carbon Substrates," *J. Electron. Mater.*, vol. 43, no. 4, pp. 1188–1193, Feb. 2014.

- [80] X. Zhang, X. Liu, B. Li, Q. Chu, Y. Wang, X. Zhao, and X. Wang, "Rapid microwave synthesis of δ -MnO₂ microspheres and their electrochemical property," *J. Mater. Sci. Mater. Electron.*, vol. 24, no. 7, pp. 2189–2196, Feb. 2013.
- [81] S. Komaba, T. Tsuchikawa, A. Ogata, N. Yabuuchi, D. Nakagawa, and M. Tomita, "Nano-structured birnessite prepared by electrochemical activation of manganese(III)-based oxides for aqueous supercapacitors," *Electrochim. Acta*, vol. 59, pp. 455–463, Jan. 2012.
- [82] S. Komaba, A. Ogata, and T. Tsuchikawa, "Enhanced supercapacitive behaviors of birnessite," *Electrochem. commun.*, vol. 10, no. 10, pp. 1435–1437, Oct. 2008.
- [83] T. Zhou, S. Mo, S. Zhou, W. Zou, Y. Liu, and D. Yuan, "Mn₃O₄/worm-like mesoporous carbon synthesized via a microwave method for supercapacitors," *J. Mater. Sci.*, vol. 46, no. 10, pp. 3337–3342, Jan. 2011.
- [84] G. H. A. Therese and P. V. Kamath, "Electrochemical Synthesis of Metal Oxides and Hydroxides," *Chem. Mater.*, vol. 12, no. 5, pp. 1195–1204, May 2000.
- [85] A. D. Cross, A. Morel, T. F. Hollenkamp, and S. W. Donne, "Chronoamperometric Versus Galvanostatic Preparation of Manganese Oxides for Electrochemical Capacitors," *J. Electrochem. Soc.*, vol. 158, no. 10, p. A1160, 2011.
- [86] W. Wei, X. Cui, X. Mao, W. Chen, and D. G. Ivey, "Morphology evolution in anodically electrodeposited manganese oxide nanostructures for electrochemical supercapacitor applications—Effect of supersaturation ratio," *Electrochim. Acta*, vol. 56, no. 3, pp. 1619–1628, Jan. 2011.
- [87] B. Babakhani and D. G. Ivey, "Anodic deposition of manganese oxide electrodes with rod-like structures for application as electrochemical capacitors," *J. Power Sources*, vol. 195, no. 7, pp. 2110–2117, Apr. 2010.
- [88] B. Babakhani and D. G. Ivey, "Effect of electrodeposition conditions on the electrochemical capacitive behavior of synthesized manganese oxide electrodes," *J. Power Sources*, vol. 196, no. 24, pp. 10762–10774, Dec. 2011.
- [89] L. Pigani, A. Heras, Á. Colina, R. Seeber, and J. López-Palacios, "Electropolymerisation of 3,4-ethylenedioxythiophene in aqueous solutions," *Electrochem. commun.*, vol. 6, no. 11, pp. 1192–1198, Nov. 2004.
- [90] N. Sakmeche, S. Aeiyaich, and J. Aaron, "Improvement of the electrosynthesis and physicochemical properties of poly (3, 4-ethylenedioxythiophene) using a sodium dodecyl sulfate micellar aqueous medium," *Langmuir*, vol. 1, no. 28, pp. 2566–2574, 1999.
- [91] M. A. Valle, P. Cury, and R. Schrebler, "Solvent effect on the nucleation and growth mechanisms of poly (thiophene)," *Electrochim. Acta*, vol. 48, pp. 397–405, 2002.

- [92] M. Morvant and J. Reynolds, "In situ conductivity studies of poly (3, 4-ethylenedioxythiophene)," *Synth. Met.*, vol. 92, pp. 57–61, 1998.
- [93] A. Milchev and L. Heerman, "Electrochemical nucleation and growth of nano- and microparticles: some theoretical and experimental aspects," *Electrochim. Acta*, vol. 48, no. 20–22, pp. 2903–2913, Sep. 2003.
- [94] M. R. Majidi, K. Asadpour-Zeynali, and B. Hafezi, "Reaction and nucleation mechanisms of copper electrodeposition on disposable pencil graphite electrode," *Electrochim. Acta*, vol. 54, no. 3, pp. 1119–1126, Jan. 2009.
- [95] J. Booth, R. G. Compton, and J. H. Atherton, "Mechanism of Solid / Liquid Interfacial Reactions . Atomic Force Microscopy Studies of the Self-Passivating Reaction between Solid p -Chloranil and Aqueous Phase N , N -Dimethylphenylenediamine," vol. 5647, no. 010, pp. 3980–3985, 2010.
- [96] B. J. Hwang, R. Santhanam, and Y.-L. Lin, "Nucleation and Growth Mechanism of Electropolymerization of Polypyrrole on Gold/Highly Oriented Pyrolytic Graphite Electrode," *J. Electrochem. Soc.*, vol. 147, no. 6, p. 2252, 2000.
- [97] A. Milchev, "Electrochemical alloy formation—theory of progressive and instantaneous nucleation without overlap," *Electrochim. Acta*, vol. 42, no. 10, pp. 1533–1536, Jan. 1997.
- [98] Z. Guo and L. Tan, *Fundamentals and Applications of Nanomaterials*. Norwood: Artech House, 2009.
- [99] R. J. Stokes and D. F. Evans, *Fundamentals of Interfacial Engineering*. New York: Wiley, 1997.
- [100] J. Goldstein, D. Newbury, D. Joy, C. Lyman, P. Echlin, E. Lifshin, L. Sawyer, and J. Michael, *Scanning Electron Microscopy and X-Ray Microanalysis*, Third. New York: Springer Science, 2003.
- [101] T. B. Reddy, *Linden's Handbook of Batteries*, Fourth Edi. New York: McGraw-Hill Education, 2011.

Chapter 3: Electrodeposition of Mn Oxide Rods on Ni foam

3.1 Introduction

As society moves away from fossil fuels towards renewable energy sources, energy storage is becoming increasingly important. Electrochemical supercapacitors are gaining an increasing amount of attention because of their high power density and long cycle life. Electrochemical supercapacitors bridge the power/energy gap between batteries and conventional capacitors. Applications for electrochemical supercapacitors include hybrid and electric vehicles, portable electronics, and renewable energy grids. [1-4]

Many materials exhibit super capacitance including transition metal oxides, carbon materials, and conducting polymers. [4,5] Of these materials, Mn oxide is of particular interest because it is environmentally benign, inexpensive, and has a large theoretical capacitance (1100-1300 F/g). Because of Mn oxide's poor electronic and ionic conductivity, it is difficult to achieve the theoretical capacitance while maintaining a reasonable level of mass loading. Another challenge for Mn oxide is dissolution during cycling. There are multiple ways of addressing the dissolution problem, including application of a protective coating or by modifying the electrolyte. Being a transition metal, Mn forms oxides in a variety of stable compositions and crystal structures. The electrochemical properties of Mn oxide are dependent on its atomic and crystal structure, as well as a number of other factors including morphology, porosity, and defect chemistry. By altering these structural parameters, it is possible to modify and optimize the electrochemical properties of a Mn oxide deposit [4,5].

As described in previous work [6-8] (see Section 2.5), our research group has developed a template-free anodic electrodeposition process to deposit high surface area, rod-like Mn oxide onto Au coated Si. Images of the rods are shown in Figure 3-1. This template free process is an excellent method for the easy production of high surface area Mn oxide deposits. Template assisted methods such as ones using anodic alumina oxide can be quite complicated and are impractical for large scale applications. [5,6] Electropolymerization of 3,4-ethylenedioxythiophene (EDOT) was used to coat Babakhani and Ivey's deposits with polyethylenedioxythiophene (PEDOT). Addition of this conductive polymer coating increased the specific capacitance of the deposits from 185 F/g to 285 F/g at a scan rate of 20 mV/s. The PEDOT coating also reduced dissolution during cycling and improved capacitance retention after

250 cycles from 75% without PEDOT to 92% with PEDOT. This increase in performance was attributed to the PEDOT shell providing an interconnected network that facilitated charge-transfer and electron conduction, and reduced dissolution during cycling. [7] Although the specific capacitances obtained by Babakhani and Ivey are quite high, depositing on Au coated Si has two main issues. Firstly, Au coated silicon is not a realistic substrate to use in practical applications because of cost and mechanical strength. Secondly, planar surfaces do not allow for much mass loading.

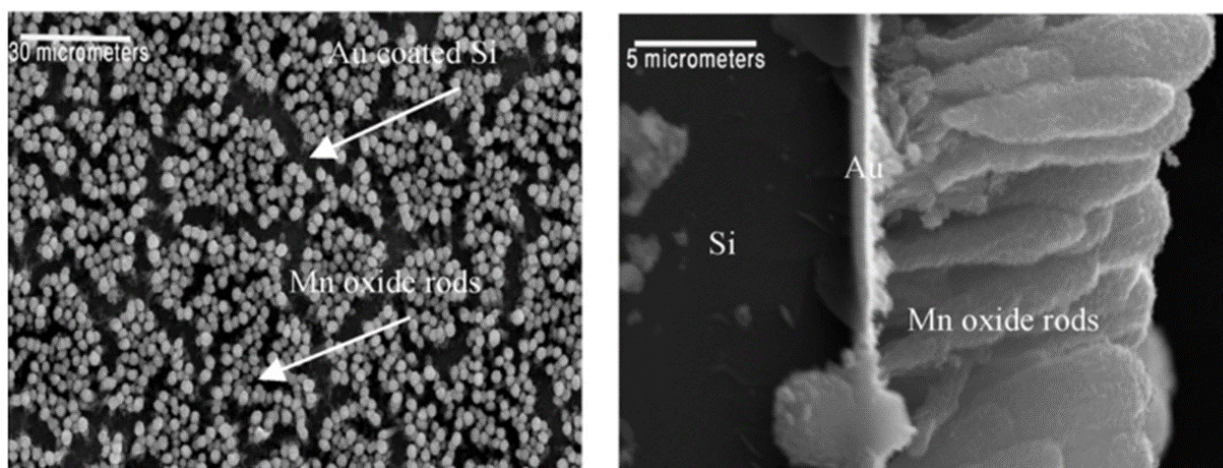


Figure 3-1: SEM SE images (plan view and cross section) of Mn oxide rods on Au coated Si, The deposits were prepared from 0.01 M $\text{Mn}(\text{CH}_3\text{COO})_2$ at 60°C at a current density of 5 mA/cm^2 for 10 min. [6]

Mass loading is an important parameter affecting capacitive performance. There is typically a trade-off between mass loading and specific capacitance. This is largely because of Mn oxide's poor electronic conductivity; thicker deposits are highly resistive which reduces electron access to parts of the deposit. It is important to consider mass loading when comparing capacitive performance; capacitance values in this work are reported in units of F/g as well as F/cm^2 (using the geometric area).

The purpose of this work is to apply the deposition process developed by Babakhani and Ivey to a more practical substrate. Nickel foam was selected as the substrate because it is highly conductive and very porous. When used as a scaffold for Mn oxide, nickel foam enhances the conductivity of the deposit while also facilitating electrolyte access. Because of the high porosity of the nickel foam, it is possible to obtain high degrees of mass loading without compromising

specific capacitance. This allows for higher nominal areal capacitance than for deposits on planar surfaces.

3.2 Experimental

3.2.1 Mn oxide deposition

Ni foam disks, 1.8 cm in diameter, were ultrasonically cleaned in acetone and then ethanol for 10 min each. Preliminary depositions were done using the same cell set up used by Babakhani and Ivey. [6-8] However, their cell configuration resulted in deposits that were nonuniform. To improve deposit uniformity, a new cell was developed and used for the majority of this work. Unless otherwise mentioned, all deposits were conducted using the new cell configuration. A schematic of the deposition apparatus is shown in Figure 3-2. Using conductive Cu tape, a Ni foam sample was attached to the bottom of the rotating shaft. To remove air trapped in the porosity of the foam, electrolyte was flushed through the Ni foam before deposition. During deposition, the sample was rotated at 75-200 RPM at a distance of 1 cm away from the Pt mesh counter electrode. Mn oxide was anodically electrodeposited onto Ni foam using a solution composed of 0.01 M $\text{Mn}(\text{C}_2\text{H}_3\text{O}_2)_2$ (Mn acetate), 0.02 M $\text{NH}_4(\text{C}_2\text{H}_3\text{O}_2)$ (ammonium acetate), and 10% $\text{C}_2\text{H}_6\text{OS}$ (dimethyl sulfoxide (DMSO)). Depositions were done at 60°C for 2.5-10 min with a current density of 5-20 mA/cm². Current density was calculated using the geometric area of the Ni foam. The initial deposition conditions were taken from Babakhani and Ivey's previous work, as these conditions resulted in well defined rod structures on Au coated Si. [6-8] The deposition conditions were then varied to apply the deposition process to Ni foam. Ammonium acetate and DMSO were added to the electrolyte to improve deposit uniformity and reproducibility. After deposition, samples were rinsed with deionized water and dried in air at 100°C for 60 min and then stored in a vacuum desiccator. The mass of the deposits was measured using a Mettler-Toledo UMX2 ultra-microbalance with an accuracy of 0.1 µg.

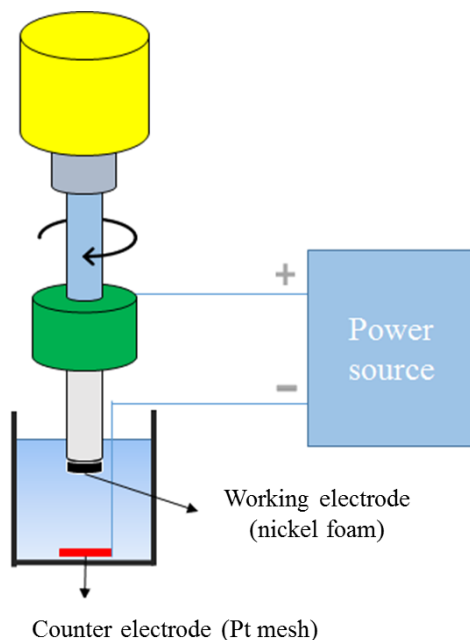


Figure 3-2: Cell schematic for Mn oxide deposition on Ni foam.

3.2.2 Electropolymerization of PEDOT

Electropolymerization of PEDOT was conducted using a 3 electrode set up, with Pt mesh as the counter electrode and a saturated calomel electrode (SCE) as the reference electrode. The working and counter electrodes were placed vertically 2 cm apart. The electrolyte was composed of 0.08 M EDOT, 0.2 M LiF₄B, and 0.14 M sodium dodecyl sulfate. It is important that the deposition electrolyte is freshly prepared, as solutions older than 24 h produce poor quality deposits. Electropolymerization was done at a constant potential of 1 V vs SCE for 45 s at 25°C. The conditions and solution composition used for electropolymerization of PEDOT were taken from Babakhani and Ivey's previous work, as these conditions provided the greatest improvement to capacitive performance. [7]

3.2.3 Materials characterization

The morphology of the deposits was investigated using a Tescan Vega-3 scanning electron microscope (SEM) operated at 20 kV. A Zeiss Orion He ion microscope (HIM), operated at an accelerating voltage of 31 kV, was used for higher resolution, surface sensitive imaging. Samples imaged using HIM were deposited on Au coated Si, to make imaging easier. These deposits were prepared at 5 mA/cm² and 60°C for 5 min using the solution of Mn acetate, ammonium acetate,

and DMSO. The PEDOT coating was prepared at 1 V for 45 s. These conditions produced Mn oxide and Mn oxide/PEDOT deposits with similar microstructures to those generated on Ni foam.

A Phillips CM-20 field emission transmission electron microscope (TEM), operated at 200 kV, was used for higher resolution imaging as well as crystallographic analysis. To prepare samples for TEM analysis, deposits were scraped off the substrate and ultrasonically suspended in ethanol. A few drops of the suspension were then placed on a C-coated Cu grid and allowed to dry.

X-ray photoelectron spectroscopy (XPS) was used to determine the chemical state of Mn oxide deposits. The XPS instrument was a Kratos AXIS Ultra X-ray photoelectron spectrometer, utilizing a monochromatic Al source, and operated at 210 W with a pass energy of 20 eV. XPS spectra were calibrated using the C 1s peak located at a binding energy of 285 eV.

3.2.4 Electrochemical characterization

Electrochemical testing was conducted using a Biologic SP-300 potentiostat. All electrochemical tests were conducted using an electrolyte of 0.5 M Na₂SO₄, with a Pt counter electrode and a SCE reference electrode; all reported potentials are with respect to SCE. Cyclic voltammetry (CV) and galvanostatic cycling (GSC) were used to determine capacitive performance of Mn oxide deposits. All CV and GSC measurements were made between 0 and 0.9 V. Extended cycling was done using CV for up to 500 cycles at a scan speed of 20 mV/s. GSC measurements were conducted at charge/discharge rates varying from 0.5 to 20 mA/cm².

3.3 Results and discussion

3.3.1 Mn oxide deposition conditions

To apply the deposition process developed by Babakhani and Ivey to Ni foam, some of the deposition conditions were modified. Preliminary experiments were done using a solution containing only Mn(C₂H₃O₂)₂ and this resulted in deposits with poor uniformity. After reviewing the literature, NH₄(C₂H₃O₂) (ammonium acetate) and DMSO were selected as additives and greatly improved the uniformity and reproducibility of the deposits. All subsequent deposits are

fabricated from electrolytes containing 0.01 M $\text{Mn}(\text{C}_2\text{H}_3\text{O}_2)_2$, 0.02 M $\text{NH}_4(\text{C}_2\text{H}_3\text{O}_2)$, and 10% $\text{C}_2\text{H}_6\text{OS}$ (DMSO).

To determine the optimal current density, depositions were done at various current densities between 5 and 20 mA/cm^2 for 2.5 min. The morphologies of these deposits are shown in Figure 3-3. As mentioned in the experimental section, preliminary depositions were conducted using Babakhani and Ivey's cell configuration. The deposits prepared at varying current densities (Figure 3-3) were also prepared using Babakhani and Ivey's cell. [6-8]. Depositing at 5 and 10 mA/cm^2 resulted in a thin layer of Mn oxide across the Ni surface. Although this layer was quite fibrous, the morphology of these deposits did not allow for a large degree of mass loading before cracking and delamination of the layer occurred. Depositing at 15 mA/cm^2 resulted in a very fibrous morphology, with some areas that had small rod-like structures. At 20 mA/cm^2 , rods were grown on the Ni foam surface. Depositing at 20 mA/cm^2 resulted in the most desirable morphology; this is the current density that was used for the remaining experiments. Note that this current density is significant higher than the current density (5 mA/cm^2) utilized by Babakhani and Ivey to fabricate similar rod-like structures on planar Au substrates. This is due to the porous nature of the Ni foam, which means that the actual current density is significantly less than 20 mA/cm^2 .

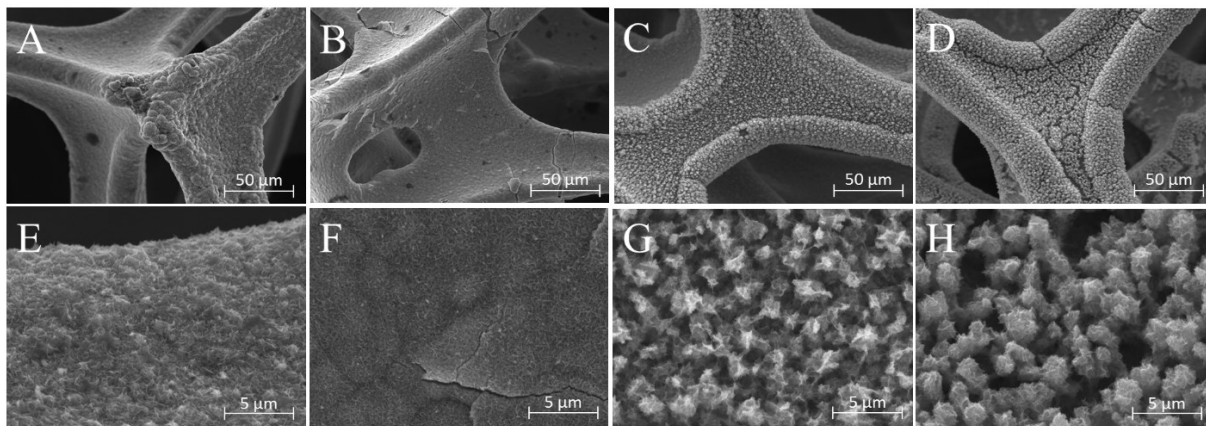


Figure 3-3: SEM SE images of Mn oxide deposits prepared using the $\text{Mn}(\text{C}_2\text{H}_3\text{O}_2)_2$ electrolyte with $\text{NH}_4(\text{C}_2\text{H}_3\text{O}_2)$ and DMSO as additives, at various current densities: (A, E) 5 mA/cm^2 , (B, F) 10 mA/cm^2 , (C, G) 15 mA/cm^2 , and (D, H) 20 mA/cm^2 . Depositions were conducted for 5 min.

Although the addition of $\text{NH}_4(\text{C}_2\text{H}_3\text{O}_2)$ and DMSO helped to improve the uniformity of deposits, depositions using Babakhani and Ivey's cell configuration resulted in variations in agitation

speed across the sample surface. [8] To reduce these variations, the configuration shown in Figure 3-2 was developed. By rotating the sample instead of relying on external stirring, the agitation speed was much more uniform across the sample surface. Deposits prepared at different rotation speeds for 2.5 min at 20 mA/cm² are shown in Figure 3-4. A rotation speed of 75 RPM resulted in the best morphology. At 75 RPM, Mn oxide is deposited as rods that cover the majority of the sample surface. If the rotation speed is reduced to 50 RPM the resulting deposits are non-uniform, with many areas of the foam receiving no deposition. Increasing rotation speed to 100 RPM resulted in rods that quickly grew laterally, fusing together into a thick layer of Mn oxide.

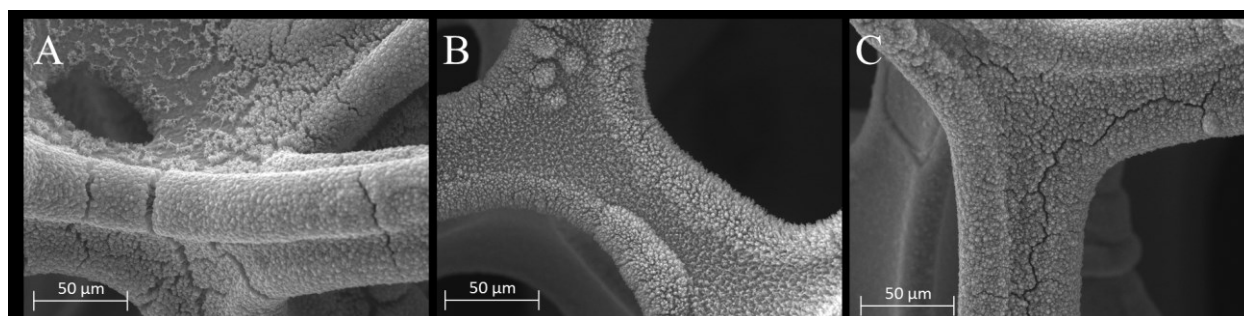


Figure 3-4: SEM SE images of Mn oxide deposits prepared at varying rotation speeds: (A) 50 RPM, (B) 75 RPM, and (C) 100 RPM. The current density and deposition time were 20 mA/cm² and 2.5 min, respectively.

To achieve different degrees of mass loading, samples were prepared at various deposition times. The average mass of deposited Mn oxide was 1.5, 3, and 5 mg/cm² for deposition times of 2.5, 5, and 10 min, respectively. The microstructures of these deposits are shown in Figure 3-5. With a deposition time of 2.5 min, the deposit consists of Mn oxide rods across the majority of the sample. The packing of the rods is not very tight for the 2.5 min sample, which means that a large portion of the Ni foam surface is not utilized. Increasing deposition time to 5 min does not change the structure of individual rods drastically, but results in tighter packing of the rods. Because of their similar structure, it is expected that the 2.5 and 5 min samples exhibit similar specific capacities. Cyclic voltammetry at 10 mV/s gives specific capacities of 133 and 130 F/g for 2.5 and 5 min deposits, respectively. A deposition time of 10 min results in a deposit that is composed of Mn oxide rods that have fused together to create a thick layer of Mn oxide. Because of a volume change upon drying, this thick layer cracks and peels during drying. The specific capacitance for the 10 min deposit was 57 F/g at 10 mV/s. The drop in capacitance as the

deposition time is increased from 5 to 10 min can be attributed to the thickness of the deposit as well as delamination of the deposit from the current collector. Deposits at 2.5, 5 and 10 min exhibited areal capacities of 220, 330 and 250 mF/cm², respectively. Because the 5 min sample exhibited the highest areal capacitance, it was selected as the optimum deposition time.

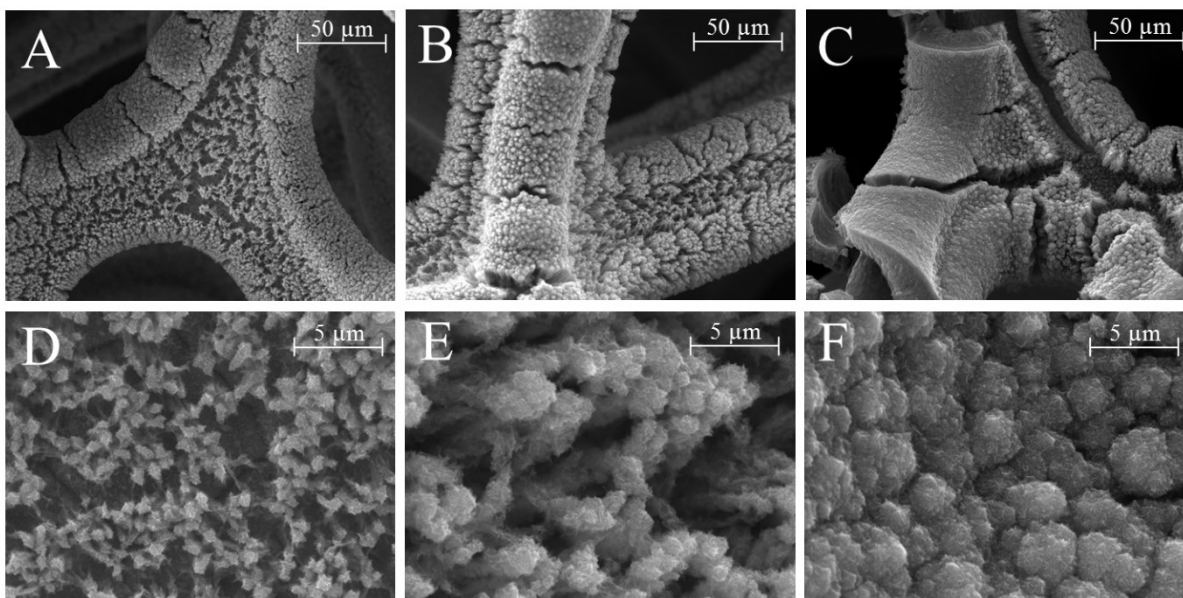


Figure 3-5: SEM SE images of Mn oxide deposits prepared with varying deposition times: (A, D) 2.5 min, (B, E) 5 min, and (C, F) 10 min. Deposition current density was 20 mA/cm² and rotation speed was 75 RPM.

For the optimum electrodeposition conditions of 5 min deposition time, 75 RPM rotation speed, and a current density of 20 mA/cm², the morphology consists of Mn oxide rods across the majority of the sample surface. Trapped air bubbles during deposition create areas that allow for imaging of the rods from the side; one such area is shown in Figure 3-6A. The rods are around 10 μm in length, tapered towards the substrate, and about 2 μm wide at their largest width. Edges of the Ni foam act as current risers, resulting in denser packing of rods in these areas. The rods themselves are very fibrous; they appear to be composed of many thin sheets. The formation mechanism will be discussed in detail in Chapter 4. The fibrous structure of the rods increases the surface area of the deposit, improving capacitive performance. Deposition of Mn oxide extends into the porosity of the Ni foam; one such area is shown in Figure 3-6B. It is unclear how deep into the Ni foam the deposit extends. Mn oxide has been observed as deep into the foam as SEM imaging allows; which is about four layers deep. SEM imaging becomes more difficult in areas deep within porosity. The morphology of the deposit within the Ni foam

porosity varies from continuous coatings to well defined rods. The porous structure of the Ni foam affects the agitation and effective current density that different areas of the Ni foam experience during deposition. These variations in conditions give rise to a variety of microstructures in areas deep within the porosity of the foam.

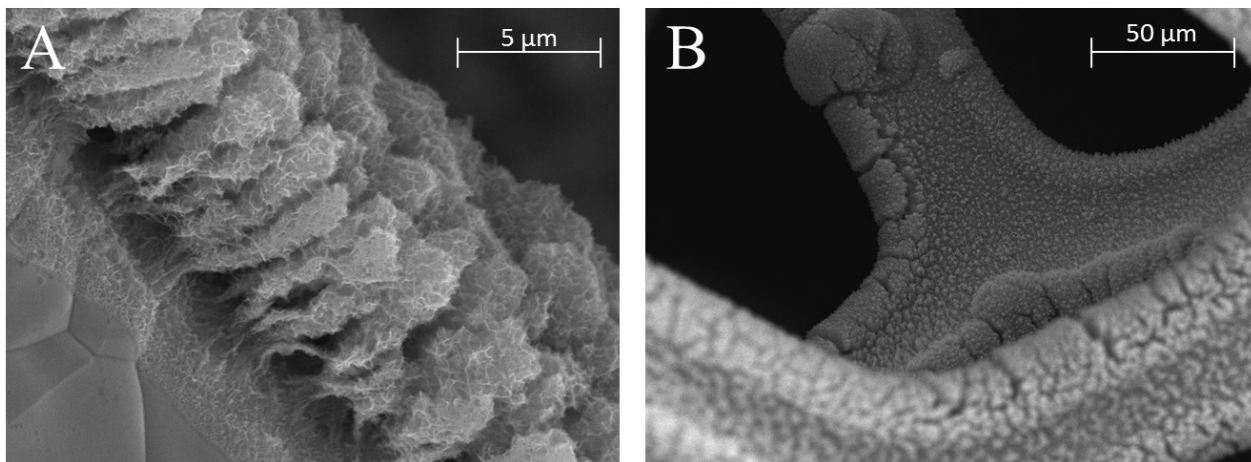


Figure 3-6: SEM SE images of Mn oxide deposits. (A) Side view of Mn oxide rods, (B) Mn oxide deposit within the Ni foam porosity. Mn oxide deposits were prepared at 20 mA/cm² for 5 min at 75 RPM.

3.3.2 PEDOT deposition

The electropolymerization process used by Babakhani and Ivey to produce coaxial core/shell Mn oxide/PEDOT rods was applied to the Mn oxide deposits on Ni foam produced in this work. Figure 3-7 shows the morphology of Mn oxide deposits with and without the addition of PEDOT. SEM imaging showed no noticeable difference between deposits with and without the PEDOT coating. Helium ion microscopy (HIM) was used to view the microstructures at much higher magnification. Images of deposits on Au coated Si are shown in Figure 3-8. The HIM images clearly show a difference in structure between the coated and uncoated samples. The image of the uncoated sample shows the thin sheet structure of the rods (Figure 3-8A). Figure 3-8B shows the Mn oxide rods conformally coated by porous PEDOT.

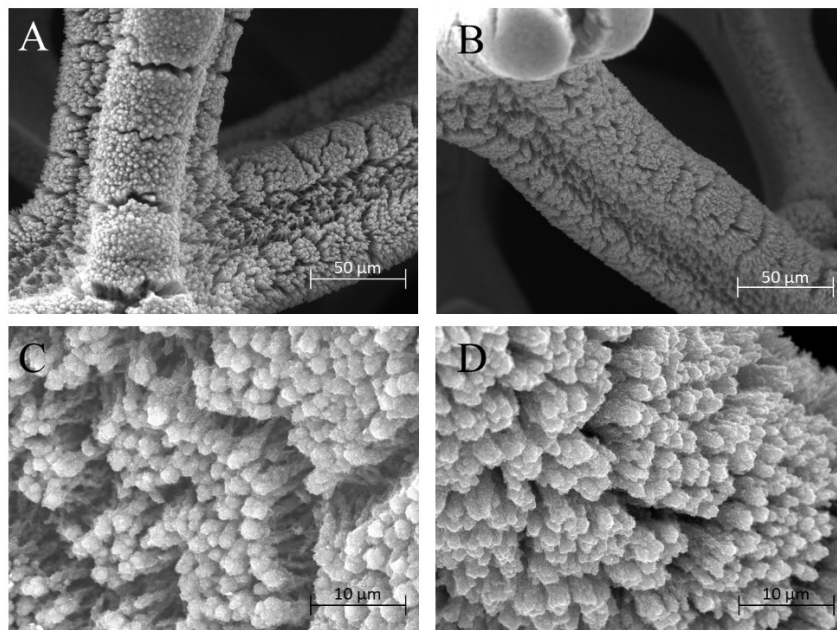


Figure 3-7: SEM SE images of Mn oxide deposits: (A,C) without PEDOT, (B,D) with PEDOT. Mn oxide deposits were prepared using 20 mA/cm^2 for 5 min at 75 RPM. The PEDOT coating was prepared at 1 V for 45 s.

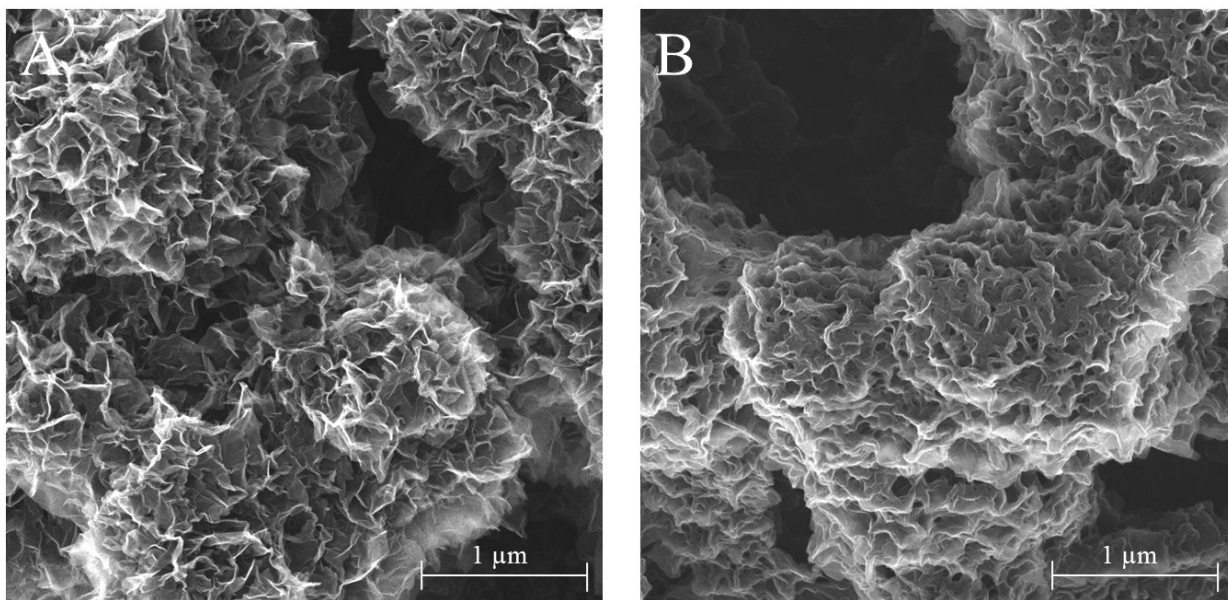


Figure 3-8: HIM SE images of Mn oxide deposits: (A) without PEDOT, (B) with PEDOT. Mn oxide deposits were prepared on Au coated Si at 5 mA/cm^2 for 5 min. The PEDOT coating was prepared at 1 V for 45 s.

3.3.3 Transmission electron microscopy

TEM results for as deposited and cycled (500 cycles at 20 mV/s) Mn oxide deposits, prepared at 20 mA/cm² and 75 RPM for 5 min, are shown in Figure 3-9. Figure 3-9A shows a cluster of Mn oxide sheets. A selected area electron diffraction pattern was obtained from the area in Figure 3-9A. The diffraction pattern shown in Figure 3-9B consists of three weak intensity rings, which indicates that the structure is poorly crystalline. The diffraction pattern can be indexed to a cubic spinel $Fd\bar{3}m$ Mn₃O₄ structure as well as a hexagonal birnessite $R\bar{3}m$ MnO₂ structure. The d spacings for the rings are 0.240, 0.209, and 0.140 nm, which respectively correspond to the (311), (400), and (440) planes of the cubic spinel structure. The 0.240 nm and 0.140 nm match with the (006) and (119) planes of the hexagonal birnessite structure. The 0.209 nm ring matches with the birnessite diffraction data, but does not have Miller indices assigned. A faint spot is present at a d spacing of 0.165 nm, which is consistent with the (511) plane of the cubic spinel structure and the (301) plane of the hexagonal birnessite structure. It should be noted that X-ray diffraction was also done on these samples, but yielded no significant peaks because of poor crystallinity. The diffraction data are shown in the Appendix.

The bright field image for the cycled deposit (Figure 3-9C) shows a cluster of Mn oxide sheets very similar to the as deposited sample. The diffraction pattern obtained from these sheets consists of three rings at d spacings of 0.241, 0.211, and 0.140 nm, which are very similar to the values for the as deposited sample. The rings for the cycled sample are more defined, indicating a more crystalline structure. For the cycled sample, as with the as deposited sample, the diffracted rings can be indexed to the cubic spinel structure (Mn₃O₄) as well as the hexagonal birnessite structure (MnO₂). The dark field image in Figure 3-9E shows many nanograins about 5 nm in diameter.

High resolution images of as deposited and cycled deposits are shown in Figure 3-10. Figure 3-10A (as deposited Mn oxide) was generated using a large enough objective aperture to include all three rings shown in Figure 3-9B and shows Mn oxide sheets. The sheet in the center of the image is folded in such a way that allows part of the sheet to be viewed edge on. Using this image, the thickness of the sheet was determined to be about 3 nm. Other sheets are up to 5 nm in thickness. Lattice planes are observed on a few parts of the sheet, i.e., the crystalline portions, with a lattice spacing of about 0.52 nm. The observed lattice planes are likely the (111) planes of

the cubic spinel structure, or the (002) planes of the hexagonal birnessite structure; these planes have d values of 0.49 nm and 0.72 nm, respectively. Any differences in d spacings between the images and the diffraction database may be due to distortion of the sheets.

Figure 3-10B is a high resolution image of a cycled deposit; this image was also generated by including all three rings, shown in Figure 3-9D, in the objective aperture. Figure 3-10B shows a few agglomerated Mn oxide sheets, with one sheet viewed edge on. Along the length of this sheet, lattice planes are observed with a spacing of ~ 0.6 nm which is relatively close to the (002) plane spacing for the hexagonal birnessite structure ($d = 0.72$ nm) and the (111) plane spacing for the cubic spinel structure ($d = 0.49$ nm).

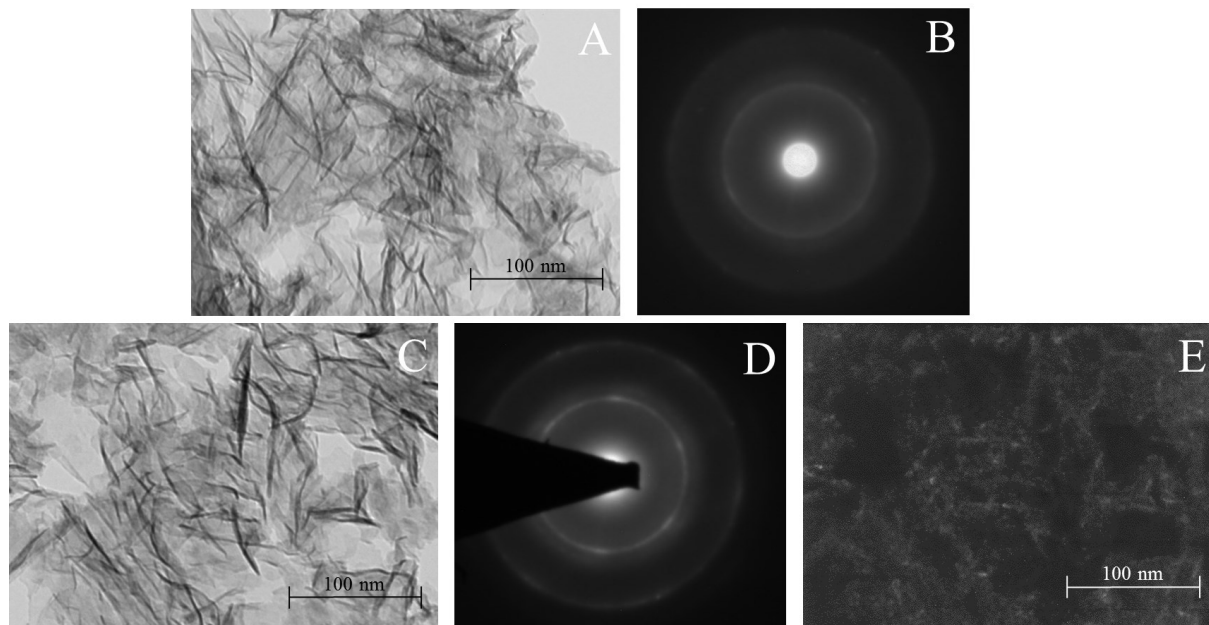


Figure 3-9: TEM results for Mn oxide deposits. (A,B) as deposited, (C-E) cycled 500 times at 20 mV/s. (A,C) Bright field images, (B,D) diffraction patterns from the regions shown in A and C, (E) dark field image. The samples were deposited at 20 mA/cm² for 10 min, with a rotation speed of 75 RPM.

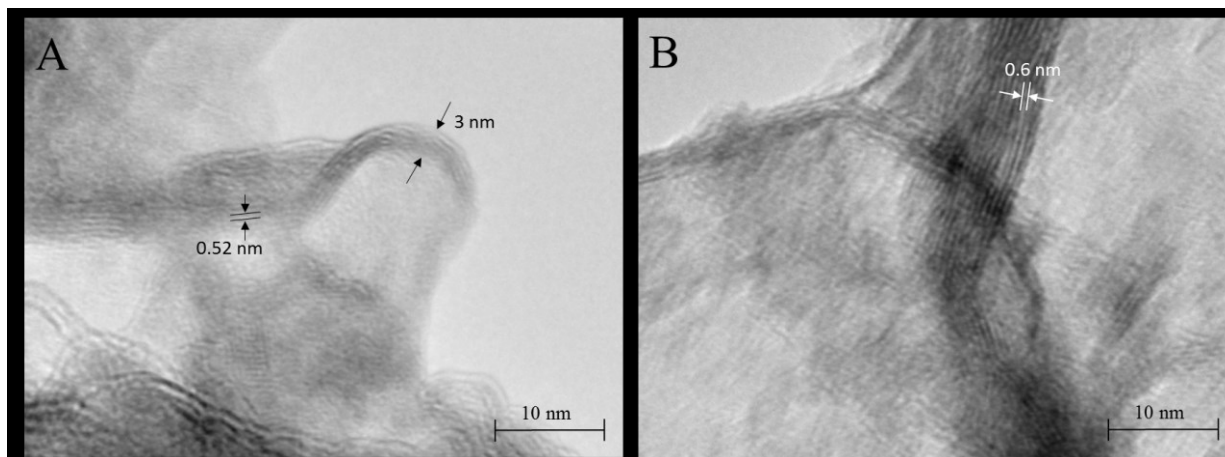


Figure 3-10: High resolution TEM image of Mn oxide deposits. (A) as deposited, and (B) cycled at 20 mV/s for 500 cycles. The samples were prepared at 20 mA/cm² for 10 min, with a rotation speed of 75 RPM.

3.3.4 X-Ray photoelectron spectroscopy

The Mn 3s XPS spectra for as deposited and cycled Mn oxide deposits prepared at 20 mA/cm² and 75 RPM for 5 min are shown in Figure 3-11. The cycled sample was cycled 500 times using CV at a scan rate of 20 mV/s. Peak splitting of the Mn 3s spectrum was used to determine the oxidation state of the Mn oxide deposits. The separation of the Mn 3s peak increases with decreasing Mn valence due to fewer unpaired electrons in the 3d orbital. Peak splitting values from Chigane *et al.* [9] and Gorlin and Jaramillo [10] have been compiled and plotted in Figure 3-12. Because curve fitting is used to determine the peak positions, there can be some variability in the measured peak splitting which depends on how the simulated curves are fit to the experimental data. Considering this variability, the measured peak splitting for the as deposited sample falls in the range of 4.7-5.1 eV. Comparing this range of values with the plot in Figure 3-12 shows that peak splitting could correspond to a range of average oxidation states. The as deposited sample contains a mixture of Mn⁴⁺, Mn³⁺, and possibly Mn²⁺. Peak splitting of 4.2-4.5 eV was measured for the cycled sample, indicating a Mn oxidation state of Mn⁴⁺. With cycling, the Mn³⁺ present in the as deposited sample is oxidized; after 500 cycles the deposit is composed almost entirely of MnO₂ (Mn⁴⁺).

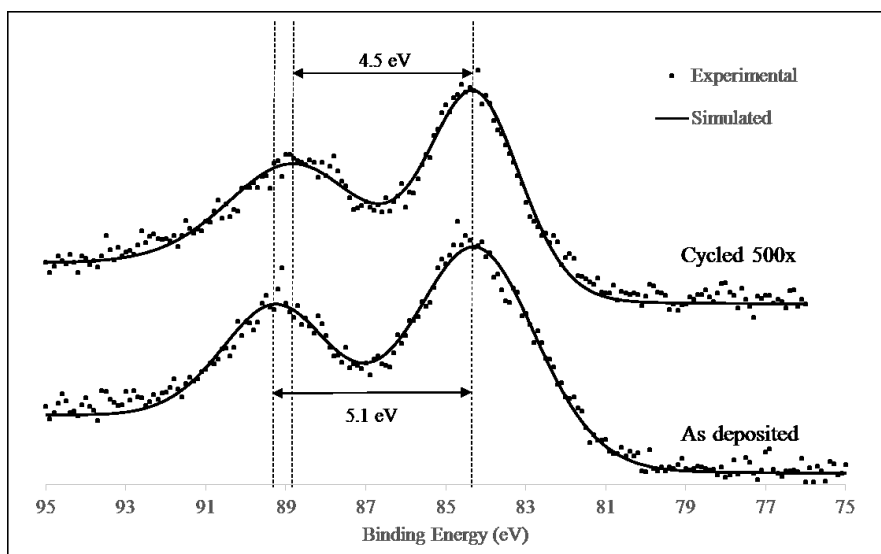


Figure 3-11: XPS Mn 3s spectra for as deposited and cycled Mn oxide (500 cycles). Mn oxide deposits were prepared at 20 mA/cm² for 5 min at 75 RPM.

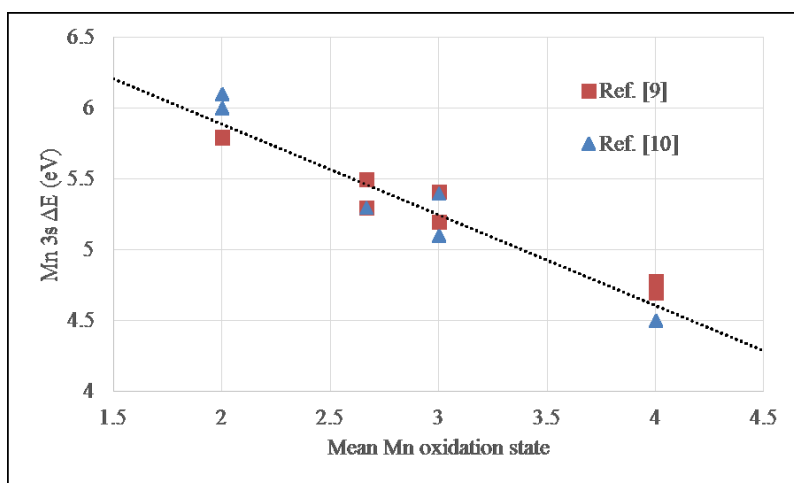


Figure 3-12: Mn 3s XPS peak splitting as a function of Mn oxidation state in MnO_x. Data were compiled from [9,10].

The combination of XPS and TEM results suggests that the cycled sample has a hexagonal birnessite MnO₂ crystal structure. The electron diffraction pattern for the cycled sample can be indexed to both the cubic spinel Mn₃O₄ structure and the hexagonal birnessite MnO₂ structure. If the deposit had a spinel structure, a Mn oxidation state of 2.67+ should be observed. However, XPS results indicate that the deposit is essentially entirely composed of Mn⁴⁺ ions, which is characteristic of MnO₂. For the as deposited sample, the combination of XPS and TEM results is less conclusive. Because XPS results for the as deposited sample indicate a range of possible oxidation states, the as deposited Mn oxide cannot be identified with certainty.

3.3.5 Cyclic voltammetry

Cyclic voltammograms for Mn oxide and Mn oxide/PEDOT deposits at varying scan speeds are shown in Figure 3-13. For deposits without PEDOT, the measured capacitance drops significantly with increasing scan speed. At scan speeds of 5 and 10 mV/s, anodic and cathodic waves are observed at around 0.5 and 0.35 V, respectively. It is believed that these waves are caused by cation deintercalation during oxidation and cation insertion during reduction. [11] With increasing scan speed, Faradaic reactions occurring in the bulk become suppressed because of the poor ionic conductivity of the deposit. The loss of the anodic and cathodic waves at scan speeds of 20 mV/s and higher demonstrate this. At sufficiently high scan speeds, the bulk is no longer electrochemically active; this is reflected as decreased capacitance at fast scan speeds. Capacitance values with varying scan speed are shown in Figure 3-14.

Application of PEDOT improves capacitive performance in terms of capacitance values as well as the shape of the voltammogram. Maximum capacitance values were 159 F/g (500 mF/cm²) and 120 F/g (290 mF/cm²) at 5 mV/s with and without PEDOT, respectively. The specific capacitance values for deposits on Ni foam are significantly lower than those reported by Babakhani and Ivey for deposits on planar Au substrates. Babakhani reported specific capacitances of 285 and 195 F/g for deposits with and without PEDOT, respectively, at a scan rate of 20 mV/s. Although higher specific capacities are achieved on Au, the smaller surface area of the planar Au limits the mass loading of Mn oxide to 0.15-0.20 mg/cm² before excessive deposit thickness causes cracking and delamination. Deposits on Au coated Si had areal capacitances of 57 and 39 mF/cm² with and without PEDOT respectively. [7] The porosity of the Ni foam allows for high degrees of mass loading. For deposits on Ni foam, a mass loading of 3 mg/cm² is possible without compromising specific capacitance. At 5 mV/s, Ni foam samples exhibited areal capacitances of 500 and 290 mF/cm² for deposits with and without PEDOT. Several studies in the literature have focused on achieving high areal capacitance on planar surfaces with Mn oxide and Mn oxide composites, and these typically achieve values around 100-300 mF/cm². [11-13] Mn oxide and Mn oxide composites prepared using high surface area substrates such as Ni foam have capacitances ranging from 100-2790 mF/cm² with most values in the 500-1000 mF/cm² range. [14-17]

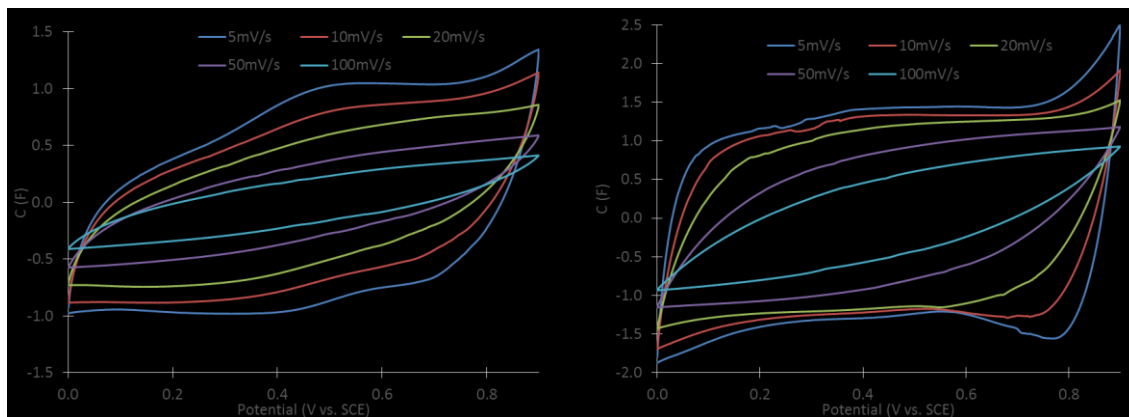


Figure 3-13: CV curves at varying scan speeds for deposits: (A) Without PEDOT and (B) with PEDOT. Mn oxide deposits were prepared at 20 mA/cm^2 for 5 min at 75 RPM. The PEDOT coating was prepared at 1 V for 45 s.

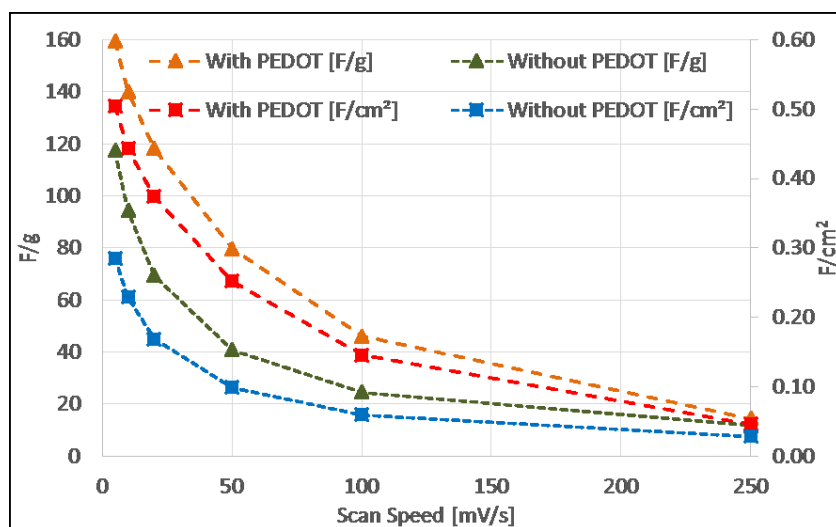


Figure 3-14: Capacitance values at various scan speeds. Mn oxide deposits were prepared at 20 mA/cm^2 for 5 min at 75 RPM. The PEDOT coating was prepared at 1 V for 45 s.

Deposits on Ni foam with PEDOT exhibit rectangular CV curves up to a scan speed of 20 mV/s , indicating nearly ideal capacitive behavior. Coating of the Mn oxide deposit with PEDOT increases the electronic conductivity, allowing more of the deposit to be electrochemically active. Mn oxide has a conductivity of around 10^{-6} - 10^{-5} S/cm , while PEDOT has a conductivity on the order of 100 S/cm . [18,19] Compared with samples without PEDOT, the response to increasing scan speed is slightly improved; the drop in capacitance with increasing scan rate is less drastic for samples with PEDOT. Although PEDOT coats the surface of the Mn oxide, it is porous enough for electrolyte ions to access the Mn oxide deposit. The mass of deposited PEDOT is 0.5 - 1 mg/cm^2 .

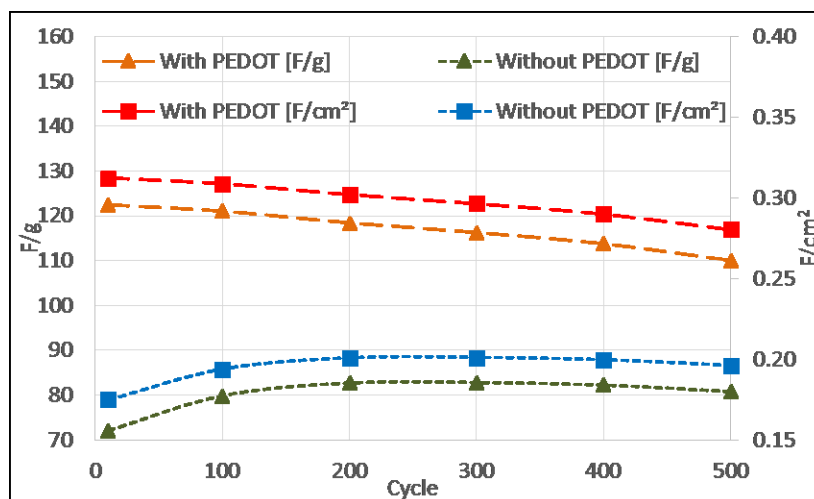


Figure 3-15: Capacitance values as a function of cycle number, at a scan rate of 20 mV/s. Mn oxide deposits were prepared at 20 mA/cm² for 5 min at 75 RPM. The PEDOT coating was prepared at 1 V for 45 s.

Deposits without PEDOT exhibit good cyclability, as shown in Figure 3-15. Mn oxide deposits without PEDOT experienced a 13% capacitance increase over 500 cycles, while deposits with PEDOT experienced a 9% capacitance drop over 500 cycles. Deposits with and without PEDOT on Au coated Si from Babakhani and Ivey's work experienced capacitance drops of 9% and 25%, respectively, after 250 cycles. Deposits with PEDOT have similar capacitance retention on planar Au and Ni foam, but deposits without PEDOT have vastly different cycling behavior. [7]

As shown in Figure 3-15, there is an increase in capacitance over the first 200 cycles for deposits on Ni foam without PEDOT. The capacitance then remains fairly constant up to 500 cycles. Figure 3-16 shows deposit morphologies after 500 cycles. Deposits without PEDOT experience significant microstructural changes during cycling. Dissolution and redeposition of Mn oxide causes fusing of rods and significant cracking and peeling of the deposit, as shown in Figure 3-16A. Peeling of the deposit would be expected to result in a loss of mass and capacitance; however, this is not the case. There was no significant mass change due to cycling and only a slight drop in capacitance from 200 to 500 cycles. Figure 3-16C shows a crack and some peeling of the Mn oxide deposit. The areas above and below the crack experienced dissolution during cycling; the rods present before cycling have been dissolved. The cracking of the Mn oxide layer exposed the underlying Ni substrate. Mn oxide then redeposited onto the bare Ni during cycling, resulting in a very fibrous and sheet-like morphology within the crack (indicated with an arrow in Figure 3-16C).

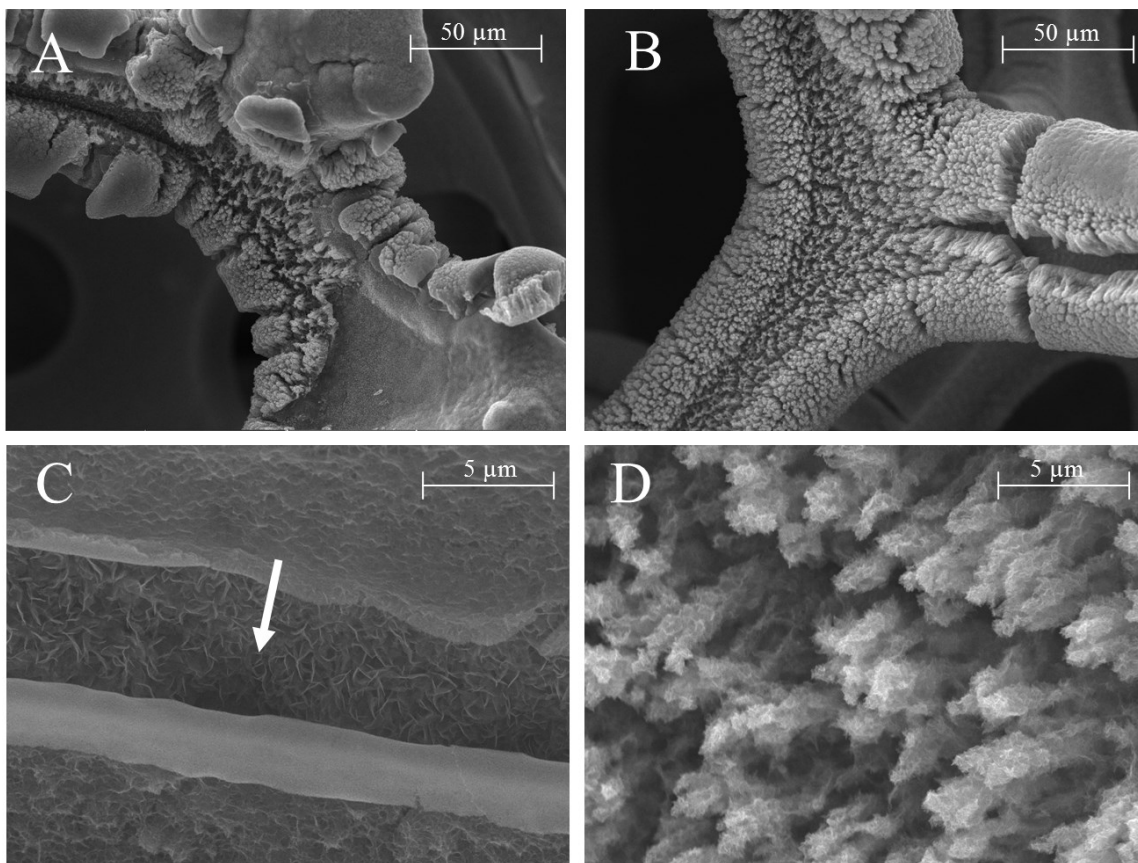


Figure 3-16: SEM SE images of Mn oxide deposits after 500 cycles: (A,C) Without PEDOT and (B,D) with PEDOT. Note the regions of Mn oxide redeposition for the uncoated Mn oxide sample, indicated by the arrow in (C). Mn oxide deposits were prepared at 20 mA/cm² for 5 min at 75 RPM. The PEDOT coating was prepared at 1 V for 45 s.

It is proposed that the discrepancy between morphology and cycling performance can be explained by a combination of two factors: a change in oxidation state and the dissolution and redeposition of Mn oxide. As explained in Section 3.3.4, Mn³⁺ that is present in the as deposited sample is oxidized to Mn⁴⁺ during cycling. This change in Mn oxidation state can help to improve capacitive performance. Dissolution and redeposition during cycling also affects capacitive performance during cycling. Material dissolved into the electrolyte near the surface of the sample can become redeposited deeper within the porosity of the foam, increasing overall coverage. The morphology of redeposited Mn oxide is not rod-like, but fibrous, similar to the surface of the rods. Over the first few hundred cycles Mn oxide is redeposited in areas that have exposed Ni; this is accompanied by an increase in capacitance. Microstructural changes, such as fusing of rods, account for the capacitance decrease between cycles 200 and 500. Deposits on planar Au, from Babakhani and Ivey's work, did not show the same capacitance increase with

cycling. [7] Deposits on Au coated Si did not have any exposed areas to allow for redeposition during cycling. These deposits experienced dissolution without redeposition, which explains why the capacitance of deposits on Ni foam improved with cycling, while deposits on Au coated Si experienced a capacitance decrease.

Although capacitance decreased for the PEDOT coated samples on cycling, the capacitance at cycle 500 was still significantly higher for deposits with PEDOT compared with those without PEDOT. After 500 cycles, the capacitance values were 110 F/g (0.28 F/cm^2) and 81 F/g (0.20 F/cm^2) with and without PEDOT, respectively, at a scan rate of 20 mV/s. For the PEDOT coated samples a fairly constant capacitance drop occurred with increasing cycle number, with about a 9% drop after 500 cycles. SEM imaging revealed no observable redeposition of Mn oxide; the PEDOT coating successfully prevented dissolution of the Mn oxide. The deposit had only small microstructural changes after cycling, as shown in Figure 3-16B. A small amount of deposit cracking was observed during cycling and was localized to regions closest to the counter electrode. The decrease in capacitance may be attributed to mechanical degradation of the PEDOT layer during cycling. [4]

3.3.6 Galvanostatic cycling

Galvanostatic cycling (GSC) was performed to measure capacitance values at charge/discharge rates varying from 0.5 to 20 mA/cm². GSC curves are shown in Figure 3-17 and capacitance results are summarized in Figure 3-18. Samples without PEDOT exhibit triangular GSC curves up to a charge/discharge rate of 2 mA/cm². At faster charge/discharge rates the curves diverge from the ideal triangular shape, indicating poor performance at fast charge/discharge rates. GSC curves for the PEDOT sample were nearly ideal up to a charge/discharge rate of 20 mA/cm². The addition of PEDOT greatly improves capacitive performance at elevated charge/discharge rates.

In both samples, with and without PEDOT, a sudden decrease in voltage is observed after switching from a charge cycle to a discharge cycle. This is due to the intrinsic resistance (IR) of the electrochemical system. Electrolyte resistance, contact resistance, and resistance of the electrode all contribute to the IR drop. The magnitude of the IR drop increases with increasing charge/discharge rate. The magnitude of the IR drop is reduced with the addition of PEDOT, especially at charge/discharge rates above 5 mA/cm². The addition of PEDOT improves the rate capability of the Mn oxide deposit by reducing the electronic resistance of the electrode.

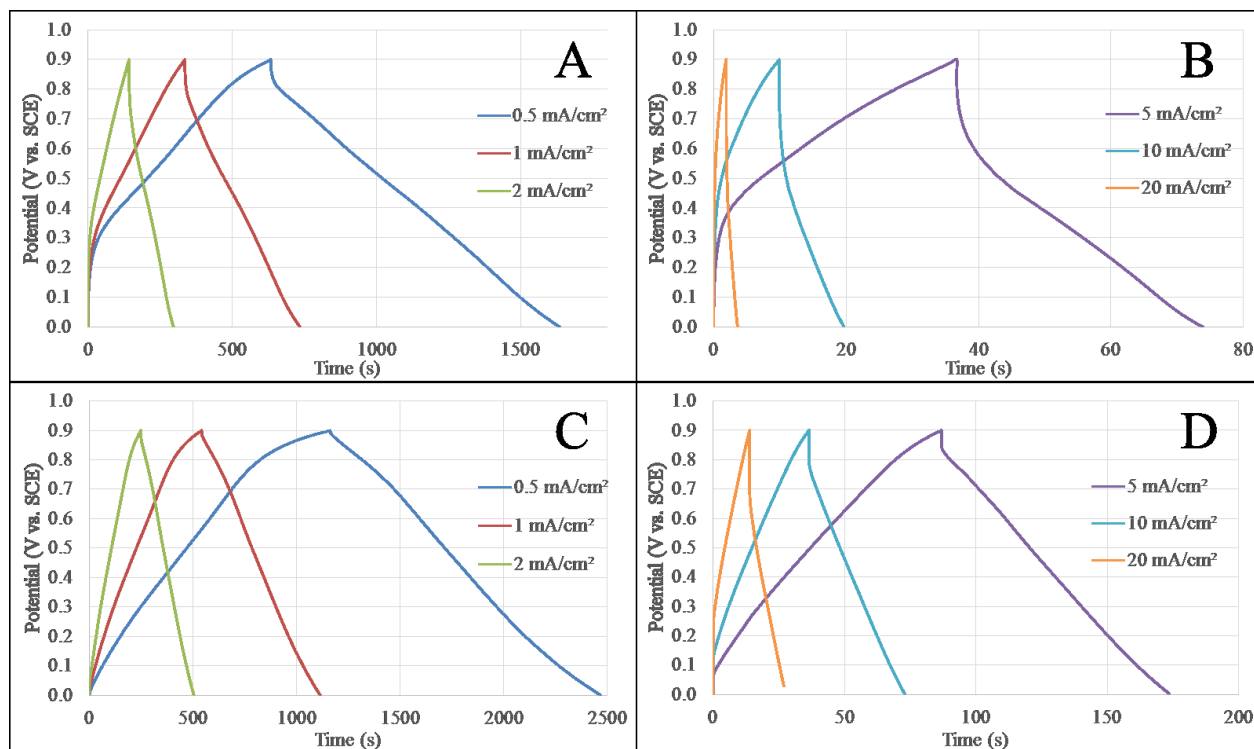


Figure 3-17: GSC curves for Mn oxide deposits on Ni foam at varying charge/discharge rates: (A,B) without PEDOT, (C,D) with PEDOT. Mn oxide deposits were prepared at 20 mA/cm² for 5 min at 75 RPM. The PEDOT coating was prepared at 1 V for 45 s.

The maximum capacitance values were obtained at 0.5 mA/cm², with capacitance values of 217 and 144 F/g (690 and 450 mF/cm²) for deposits with and without PEDOT, respectively. Typical areal capacitances reported in the literature are 100-300 mF/cm² for planar surfaces and 500-1000 mF/cm² for high surface area substrates. [11-17] Capacitance values drop with increasing charge/discharge rate. At 20 mA/cm² capacitance values are 97 and 13 F/g (310 and 40 mF/cm²) for deposits with and without PEDOT; respectively. For comparison, at 20 mA/cm² Yang *et al.* reported an areal capacitance of 864 mF/cm² for thick Mn oxide deposits electrodeposited on Ni foam. [11] Increasing the charge discharge rate from 0.5 to 20 mA/cm² results in a 91% decrease in capacitance for samples without PEDOT. With PEDOT, the rate capability is improved, with a 55% decrease in capacitance between 0.5 and 20 mA/cm². The slope of the linear portion of the GSC curve has units of V/s; this slope can be used to directly compare capacitances measured through GSC and CV. For example, the 2 mA/cm² GSC curve for the sample with PEDOT has a slope of 3.6 mV/s, which is relatively close to 5 mV/s. At 2 mA/cm², the capacitance measured is

177 F/g, which is similar to the 150 F/g value measured through CV at 5 mV/s. Comparing results in this way shows that the measured capacitances are consistent using both GSC and CV.

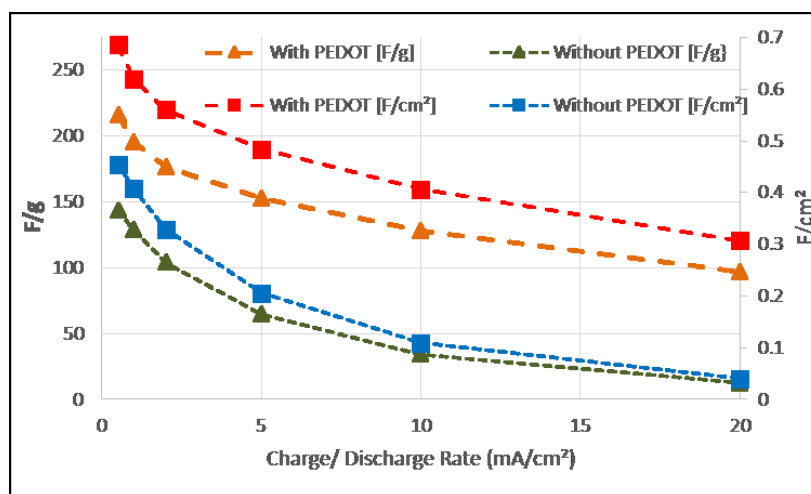


Figure 3-18: Capacitance values as a function of constant current charge/discharge rate. Mn oxide deposits were prepared at 20 mA/cm² for 5 min at 75 RPM. The PEDOT coating was prepared at 1 V for 45 s.

3.3.7 Annealing of Mn oxide deposits

Mn oxide deposits (no PEDOT) were annealed at elevated temperature to see if changing the crystallinity and/or chemical state of the deposit would improve capacitive performance. After drying for 1 h at 100°C, Mn oxide deposits on Ni foam were annealed at 350°C for 1 h in air or a reducing atmosphere of forming gas (95% N₂ 5% H₂). TEM analysis was done to determine the crystallinity of annealed deposits (Figure 3-19). The bright field images show many thin sheets; the fibrous morphology of the deposits is retained after annealing. The diffraction pattern from the sample annealed in air consists of four weak intensity rings that match with a Mn₃O₄ cubic spinel Fd-3m structure (PDF#013-0162) with a lattice parameter of 0.842 nm. The diffracted rings have d spacings of 0.257, 0.220, 0.175, and 0.147 nm which correspond to the (311), (400), (422), and (440) planes, respectively, of the cubic spinel structure. A few bright regions <20 nm in diameter are observed in the dark field image, and correspond to diffracting nanoscale grains. The grain size has increased relative to the as deposited Mn oxide.

The diffraction pattern for the sample annealed in forming gas was indexed to a tetragonal I41/amd Mn₃O₄ crystal structure (PDF#018-0803) with lattice parameters of a= 0.578 and c= 0.933 nm. The diffraction pattern consists of 8 rings; rings located at d spacings of 0.505, 0.320,

0.285, 0.257, 0.211, and 0.150 nm correspond to the (101), (112), (103), (211), (220), and (224) planes, respectively, of the tetragonal spinel structure. Rings at 0.183 nm and 0.159 nm match the tetragonal spinel diffraction database, but Miller indices have not been assigned. The diffraction pattern for the sample annealed in forming gas is much sharper than the diffraction patterns for the as deposited and air annealed samples, indicating an increased degree of crystallinity. The dark field image shows a number of bright regions, many more than the air annealed, as deposited, and cycled samples. The grain size is close to 20 nm.

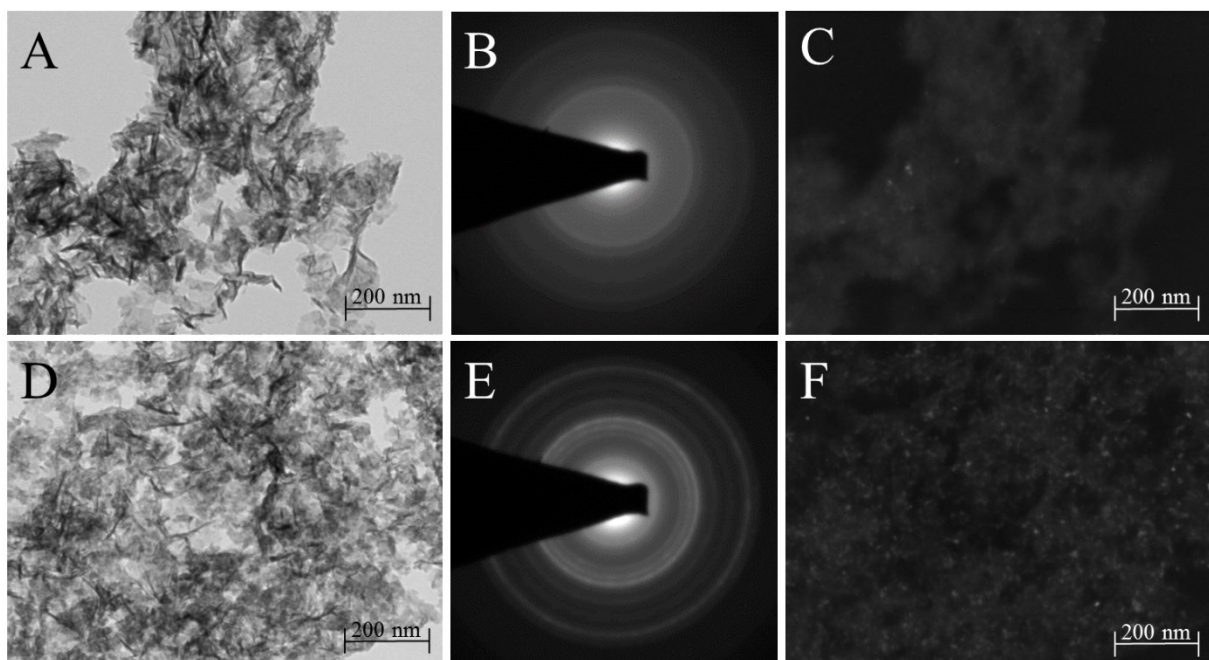


Figure 3-19: TEM results for Mn oxide deposits annealed for 1 h at 350°C in (A-C) air and (D-E) forming gas (95% N₂ + 5% H₂). (A,B) Bright field images, (B,E) selected area diffraction patterns, and (C,F) dark field images using part of the innermost rings. Mn oxide deposits were prepared at 20 mA/cm² for 5 min at 75 RPM.

CV curves were used to determine the capacitance of deposits annealed in air and forming gas for 1 h at 350°C. CV curves are shown in Figure 3-20. Capacitance measured at a scan rate of 10 mV/s was 93 F/g (230 mF/cm²) and 56 F/g (170 mF/cm²) for deposits annealed in air and forming gas, respectively. The former value is similar to that obtained for as deposited Mn oxide samples, while the latter value is considerably lower. As such, annealing in air had very little effect on the deposit.

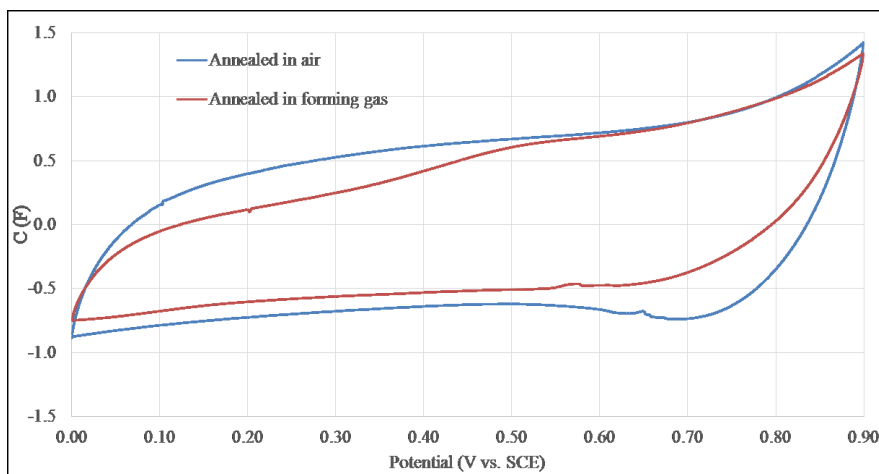


Figure 3-20: CV curves for deposits annealed in air and forming gas (95% N₂ 5% H₂) for 1 h at 350°C. Scan speed of 10 mV/s. Mn oxide deposits were prepared at 20 mA/cm² for 5 min at 75 RPM.

3.4 Conclusions

A previously developed template-free electrodeposition process, to deposit high surface area Mn oxide and Mn oxide/PEDOT rods (~2 μm in diameter and several μm in length) onto planar gold substrates, has been successfully modified to achieve similar structures on highly porous Ni foam substrates. Transmission electron microscopy (TEM) revealed that the deposits were poorly crystalline. Diffraction results for the as deposited sample showed a poorly crystalline structure and the diffraction rings could be indexed to a Mn₃O₄ cubic spinel structure as well as a MnO₂ hexagonal birnessite structure. Cycled samples had improved crystallinity and were indexed to a hexagonal birnessite MnO₂ crystal structure. High resolution TEM imaging of as deposited and cycled samples showed that the rods were composed of thin sheets (<5 nm in thickness) and the sheets were composed of nanocrystals (~5 nm in diameter).

X-ray photoelectron spectroscopy (XPS) showed a mixed valence for the as deposited Mn oxide, corresponding to a combination of Mn⁴⁺, Mn³⁺, and possibly Mn²⁺. With cycling, the Mn²⁺/Mn³⁺ ions are oxidized and after 500 cycles the deposit is mostly MnO₂ (Mn⁴⁺).

The IR drops observed during galvanostatic cycling (GSC) for deposits without PEDOT were significantly larger than those with PEDOT, indicating that the application of PEDOT improved the electronic conductivity of the electrode. Capacitance was measured using both cyclic voltammetry (CV) and GSC, with similar results. The maximum capacitance values for deposits

with and without PEDOT were 217 and 144 F/g (690 and 450 mF/cm²), respectively, measured with GSC at a charge/discharge rate of 0.5 mA/cm². The maximum capacitances measured through CV were 159 F/g and 120 F/g (500 mF/cm² and 290 mF/cm²) at 5 mV/s with and without PEDOT, respectively. CV and GSC results both showed that the addition of PEDOT improved the rate capability of the electrode. Previous work for Mn oxide deposits on planar Au substrates, with and without PEDOT, exhibited specific capacitances of 285 and 195 F/g at 20 mV/s, respectively, which are higher than those for deposits on Ni foam. However, because planar Au substrates do not allow for much mass loading, the areal capacitances for deposits on Au coated Si were relatively low (57 and 39 mF/cm² with and without PEDOT, respectively).

Mn oxide deposits (without PEDOT) were annealed at 350°C for 1 h in air and forming gas (95% N₂ 5% H₂). At a scan speed of 10 mV/s capacitances of 93 F/g (230 mF/cm²) and 56 F/g (170 mF/cm²) were measured for deposits annealed in air and forming gas, respectively. Annealed deposits showed an increase in crystallinity compared with the as deposited Mn oxide. The sample annealed in air retained its cubic spinel structure, while the sample annealed in forming gas transformed into a tetragonal Mn₃O₄ spinel structure.

The addition of PEDOT reduced dissolution and redeposition during cycling. Capacitance retention after 500 cycles for deposits with and without PEDOT was 91% and 113%, respectively. Although deposits without PEDOT exhibited better capacitance retention, deposits with PEDOT had larger capacitances after 500 cycles. After 500 cycles, capacitance values measured by CV at 20 mV/s were 110 F/g (280 mF/cm²) and 81 F/g (200 mF/cm²) with and without PEDOT, respectively. The capacitance increase during cycling for deposits without PEDOT can be explained by a combination of a change in oxidation state (from Mn³⁺ to Mn⁴⁺) and the dissolution and redeposition of Mn oxide, resulting in improved coverage of the Ni foam.

3.5 References

- [1] P. Simon and Y. Gogotsi, "Materials for electrochemical capacitors," *Nat. Mater.*, vol. 7, no. 11, pp. 845–54, Nov. 2008.
- [2] R. Ko and M. Carlen, "Principles and applications of electrochemical capacitors," *Electrochem. Commun.*, vol. 45, pp. 2483–2498, 2000.

- [3] W. Wei, X. Cui, W. Chen, and D. G. Ivey, "Manganese oxide-based materials as electrochemical supercapacitor electrodes," *Chem. Soc. Rev.*, vol. 40, no. 3, pp. 1697–721, Mar. 2011.
- [4] G. Wang, L. Zhang, and J. Zhang, "A review of electrode materials for electrochemical supercapacitors," *Chem. Soc. Rev.*, vol. 41, no. 2, pp. 797–828, Jan. 2012.
- [5] W. Wei, X. Cui, X. Mao, W. Chen, and D. G. Ivey, "Morphology evolution in anodically electrodeposited manganese oxide nanostructures for electrochemical supercapacitor applications—Effect of supersaturation ratio," *Electrochim. Acta*, vol. 56, no. 3, pp. 1619–1628, Jan. 2011.
- [6] B. Babakhani and D. G. Ivey, "Anodic deposition of manganese oxide electrodes with rod-like structures for application as electrochemical capacitors," *J. Power Sources*, vol. 195, no. 7, pp. 2110–2117, Apr. 2010.
- [7] B. Babakhani and D. G. Ivey, "Improved capacitive behavior of electrochemically synthesized Mn oxide/PEDOT electrodes utilized as electrochemical capacitors," *Electrochim. Acta*, vol. 55, no. 12, pp. 4014–4024, Apr. 2010.
- [8] B. Babakhani and D. G. Ivey, "Effect of electrodeposition conditions on the electrochemical capacitive behavior of synthesized manganese oxide electrodes," *J. Power Sources*, vol. 196, no. 24, pp. 10762–10774, Dec. 2011.
- [9] M. Chigane, M. Ishikawa, and M. Izaki, "Preparation of Manganese Oxide Thin Films by Electrolysis/Chemical Deposition and Electrochromism," *J. Electrochem. Soc.*, vol. 148, no. 7, p. D96, 2001.
- [10] Y. Gorlin and T. F. Jaramillo, "A bifunctional nonprecious metal catalyst for oxygen reduction and water oxidation," *J. Am. Chem. Soc.*, vol. 132, pp. 13612–13614, 2010.
- [11] Y. Hou, Y. Cheng, T. Hobson, and J. Liu, "Design and synthesis of hierarchical MnO₂ nanospheres/carbon nanotubes/conducting polymer ternary composite for high performance electrochemical electrodes," *Nano Lett.*, vol. 10, no. 7, pp. 2727–33, Jul. 2010.
- [12] M. Yu, T. Zhai, X. Lu, X. Chen, S. Xie, W. Li, C. Liang, W. Zhao, L. Zhang, and Y. Tong, "Manganese dioxide nanorod arrays on carbon fabric for flexible solid-state supercapacitors," *J. Power Sources*, vol. 239, pp. 64–71, Oct. 2013.
- [13] S. Devaraj and N. Munichandraiah, "High Capacitance of Electrodeposited MnO₂ by the Effect of a Surface-Active Agent," *Electrochem. Solid-State Lett.*, vol. 8, no. 7, p. A373, 2005.

- [14] Z. Sun, S. Firdoz, E. Y.-X. Yap, L. Li, and X. Lu, "Hierarchically structured MnO₂ nanowires supported on hollow Ni dendrites for high-performance supercapacitors," *Nanoscale*, vol. 5, no. 10, pp. 4379–87, May 2013.
- [15] J. Xiao, S. Yang, L. Wan, F. Xiao, and S. Wang, "Electrodeposition of manganese oxide nanosheets on a continuous three-dimensional nickel porous scaffold for high performance electrochemical capacitors," *J. Power Sources*, vol. 245, pp. 1027–1034, Jan. 2014.
- [16] P. Xu, K. Ye, D. Cao, J. Huang, T. Liu, K. Cheng, J. Yin, and G. Wang, "Facile synthesis of cobalt manganese oxides nanowires on nickel foam with superior electrochemical performance," *J. Power Sources*, vol. 268, pp. 204–211, Dec. 2014.
- [17] J. Yang, L. Lian, H. Ruan, F. Xie, and M. Wei, "Nanostructured porous MnO₂ on Ni foam substrate with a high mass loading via a CV electrodeposition route for supercapacitor application," *Electrochim. Acta*, vol. 136, pp. 189–194, Aug. 2014.
- [18] Q. Pei, G. Zuccarello, M. Ahlskog, and O. Inganäs, "Electrochromic and highly stable poly(3,4-ethylenedioxythiophene) switches between opaque blue-black and transparent sky blue," *Polymer (Guildf)*, vol. 35, no. 7, pp. 1347–1351, 1994.
- [19] R. N. Deguzman, A. Awaluddin, Y. F. Shen, Z. R. Tian, S. L. Suib, S. Ching, and C. L. Oyoung, "Electrical-Resistivity Measurements on Manganese Oxides with Layer and Tunnel Structures - Birnessites, Todorokites, and Cryptomelanes," *Chem. Mater*, vol. 7, no. 11, pp. 1286–1292, 1995.

Chapter 4: Nucleation and Growth of Mn Oxide Rods

4.1 Introduction

Previous work by our group has characterized the effect of deposition conditions on the growth of electrodeposited Mn oxide. [1,2] These studies were mainly interested in the resulting morphology and capacitive performance of the deposits; they did not investigate the early stages of nucleation. The effect of current density, solution concentration, temperature, pH, and supersaturation ratio were investigated in the previous work. By varying these conditions, a variety of microstructures were achieved, including sheets, rods and continuous coatings. The growth of rods occurred within a narrow range for each of these parameters. For a more detailed background on the previous work, see Section 2.5. The purpose of this chapter is to characterize the nucleation and growth of template free, electrodeposited Mn oxide rods at various stages of nucleation and growth.

4.1.1 Nucleation and growth

The mechanism of nucleation and growth during an electrodeposition reaction can greatly affect the final morphology of the deposit. Electrochemical deposition is a good technique for the study of the early stages of nucleation and growth because electrodeposition allows for measurements of current-time or overpotential-time relationships. [3] Nucleation can occur progressively or instantaneously. Instantaneous nucleation occurs when all the active sites available are activated very quickly; these nuclei then grow with no more nucleation occurring. Progressive nucleation occurs when nuclei are continuously formed during the entire deposition time. [4]

4.1.2 Anodic electrodeposition of Mn oxide

Anodic electrodeposition of Mn oxide can occur through two different electrochemical processes: hydrolysis and disproportionation. [5,6] Deposition processes have been studied mostly in acidic electrolytes. [7-11] The initial step of deposition is electrochemical oxidation of Mn^{2+} , producing aqueous Mn^{3+} (Reaction (4-1)). The stability of Mn^{3+} determines the deposition process and is highly dependent on pH. In highly acidic solutions Mn^{3+} is relatively stable and is able to undergo oxidation or disproportionation to form MnO_2 . In dilute acidic solutions Mn^{3+} is relatively unstable and readily undergoes hydrolysis via Reaction (4-2). [2,11] In reality,

deposition of Mn oxide occurs simultaneously through both hydrolysis and disproportionation, with the reaction preference being shifted by solution pH. Deposition through the hydrolysis pathway is a three step electrochemical-chemical-electrochemical process: [7]



The overall reaction for both hydrolysis and disproportionation mechanisms is as follows: [7]



Deposition through the hydrolysis pathway initially occurs through a solid intermediate, MnOOH. Paul and Cartwright proposed that the solid intermediate formed a porous layer on the growing MnO₂ deposit. Using electrical impedance spectroscopy and rotating ring-disk experiments, they estimated the thickness of this layer to be 2-10 μm. [7,13] MnOOH is an electronically resistive layer through which Mn²⁺ ions must diffuse before deposition can occur. Although it is known that the conversion of MnOOH to MnO₂ can be sluggish, studies claim that ion diffusion (either Mn²⁺ or H⁺) through the MnOOH layer is the rate determining step for deposition via the hydrolysis pathway. [7,9-11,14]

Disproportionation has been shown to occur in highly acidic electrolytes. [6,11] Manganese oxide deposition via the disproportionation mechanism occurs through the following reactions:



As with the hydrolysis pathway, the initial step in disproportionation is electrochemical oxidation of Mn²⁺ to form Mn³⁺. In highly acidic environments, Mn³⁺ is stable enough to diffuse to the edge of the double layer, where it can undergo disproportionation into Mn²⁺ and Mn⁴⁺ (Reaction (4-6)). [15] Mn⁴⁺ quickly hydrolyses to form MnO₂; this can occur at the electrode surface or in solution. [12,14] The rate limiting step for deposition through disproportionation is the disproportionation step itself, i.e., Reaction (4-6). [5] There are a few studies that have

investigated Mn oxide deposition in basic electrolytes. Huynh *et al.* [5] recently investigated the nucleation and growth of electrodeposited Mn oxide from a solution with a pH of 8.0. They showed that nucleation occurred progressively and that deposition occurred through a disproportionation pathway. [5] This result seems to contradict the pH dependence established from previous literature. The mechanisms behind electrodeposition of Mn oxide are not completely understood and require additional work, especially in alkaline environments.

4.2 Experimental

4.2.1 Mn oxide deposition

Pieces of Au coated Si (1.6 cm x 0.8 cm) were ultrasonically cleaned in acetone and then ethanol for 10 min each to remove any surface contamination from handling and wafer dicing. A wafer piece was placed in the cell, 2 cm away from the Pt mesh counter electrode. Deposition was conducted at 60°C, with a current density of 5 mA/cm² in a solution containing 0.01 M Mn(C₂H₃O₂)₂ (Mn acetate), 0.02 M NH₄(C₂H₃O₂) (ammonium acetate) and 10% C₂H₆OS (dimethyl sulfoxide (DMSO)). These conditions were chosen from Babakhani and Ivey's previous work because they result in well defined Mn oxide rods. [1,2] The solution used by Babakhani and Ivey did not contain ammonium acetate or DMSO; these chemicals were added to help improve reproducibility and deposit uniformity. The deposition solution was used at its natural pH of 7.5. During deposition, agitation was introduced by a magnetic stir bar rotating at 250 RPM. To study the nucleation and growth processes, depositions were conducted for a variety of times ranging from 0.5 s to 10 min. After deposition, samples were rinsed with deionized water and stored in a vacuum desiccator before further analysis.

4.2.2 Scanning electron microscopy

High resolution imaging was conducted using two scanning electron microscopes (SEM). The microscopes were a Hitachi S-4800 SEM and a Zeiss Sigma SEM. Both microscopes have field emission electron guns; the Hitachi SEM is equipped with a cold field emission electron source and the Zeiss SEM utilizes a Schottky field emission electron source. Both instruments were operated at an accelerating voltage of 2 kV and used an in-lens secondary electron (SE) detector for imaging.

4.2.3 Transmission electron microscopy

A Phillips CM-20 field emission transmission electron microscope (TEM), operated at 200 kV, was used for high resolution imaging as well as crystallographic analysis. A Hitachi HF-3300 cold field emission TEM, operated at 300 kV, was also used for some of the high resolution imaging. To prepare samples for TEM analysis, deposits were scraped off the substrate and ultrasonically suspended in ethanol. A few drops of the suspension were then placed on a lacey C coated, Cu grid and allowed to dry.

4.2.4 X-ray photoelectron spectroscopy

X-ray photoelectron spectroscopy (XPS) was used to determine the chemical state of Mn oxide deposits. The XPS instrument was a Kratos AXIS Ultra X-ray photoelectron spectrometer, utilizing a monochromatic Al source, and operated at 210 W with a pass energy of 20 eV. XPS spectra were calibrated using the C 1s peak located at a binding energy of 285 eV. Deposits prepared for XPS analysis were done on Pt coated Si because there is an overlap between the Mn 3s and Au 4f signals. SEM imaging showed no morphological difference between deposits on Au and Pt.

4.3 Results and Discussion

4.3.1 Scanning electron microscopy

SEM images of the initial stages of nucleation (1-4 s deposition times) are shown in Figure 4-1. Initial nucleation occurs as thin sheets along Au grain boundaries (Figure 4-1A). At this stage, the sheets are less than 5 nm thick. Gold grain boundaries and triple points act as preferred nucleation sites for heterogeneous nucleation because of their high energy. Some sheets also form away from the grain boundaries, possibly along other high energy defects such as twins. Once the grain boundaries are covered, nucleation of the thin sheets spreads from the grain boundaries; after about 2 seconds, sheets have formed across the surface of the Au grains. At this point, new sheets begin to nucleate on already deposited sheets. Nucleation of sheets on one another eventually leads to the formation of particles, like the one shown in Figure 4-1D. Because these particles are composed of many nanoscale sheets that have nucleated on one another, they have a very fibrous morphology. The fibrous morphology of the deposit is retained throughout all stages of deposition.

The morphology of deposits formed between 5 and 10 s is shown in Figure 4-2. As sheets continue to nucleate on one another, the morphology of the Mn oxide changes from sheet-like to round particles. This transition occurs quickly at a deposition time of around 5 s and is shown in Figure 4-2A. A schematic of the formation of round particles from agglomeration of sheets is shown in Figure 4-3. A small degree of crystallization occurs during this time as well, as indicated by TEM electron diffraction (see Section 3.3.2). At 6 s the entire Au surface is covered with round particles. As deposition proceeds, new sheets continue to nucleate and grow on one another, forming progressively more and more particles.

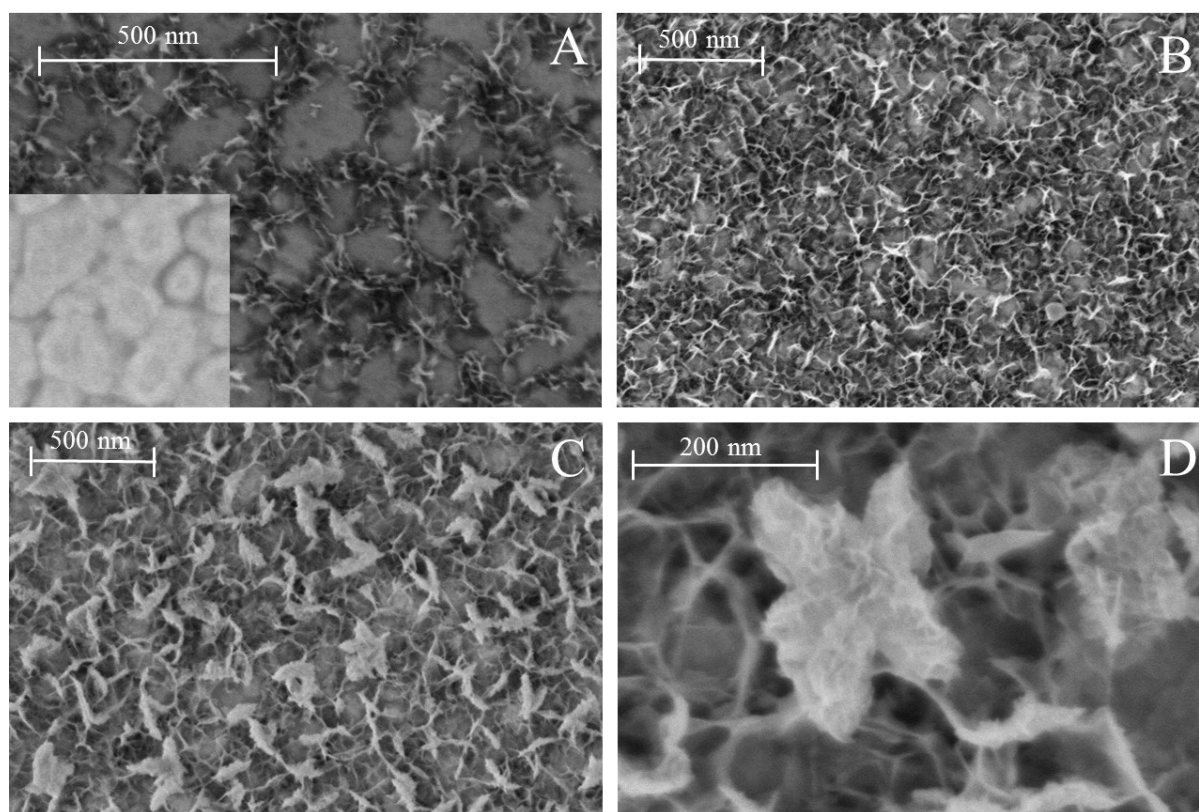


Figure 4-1: SEM SE micrographs of the early stages of nucleation and growth of Mn oxide. Deposition times were (A) 1 s (bare Au inset at same magnification), (B) 2 s and (C, D) 4 s.

After 8 s, most of the particles are 25-200 nm in size; however, some particles larger than 500 nm have formed as well (black circles in Figure 4-2C). The sheets composing these larger particles have the same thickness as the sheets present in the earlier stages of deposition (<5 nm); however, the sheets are longer and appear tangled with one another (Figure 4-2D). There are relatively few particles that are of intermediate size, between 200-500 nm, which suggests that growth in this size range occurs quickly. It is unclear why certain particles begin to accelerate in

growth. This acceleration may be attributed to local changes in pH. A decrease in H^+ concentration (an increase in pH) would drive Reaction 4-4 to the right, increasing production of MnO_2 . The orientation of the electric field may also increase the deposition rate for select particles; larger particles extend further away from the sample surface and can experience an increased potential.

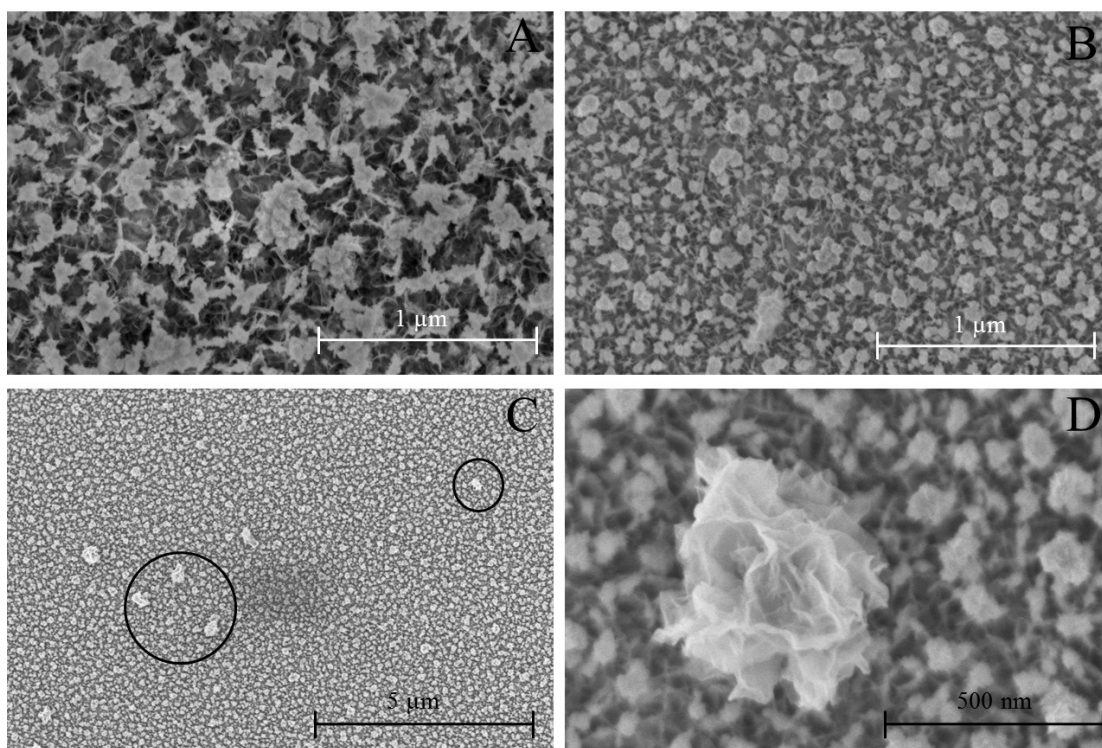


Figure 4-2: SEM SE micrographs of Mn oxide deposition: (A) 5 s, (B) 6 s, (C) 8 s, and (D) 10 s. The circled areas in (C) show larger particles that have experienced accelerated growth. (D) is a high magnification image of one such particle after a deposition time of 10 s.

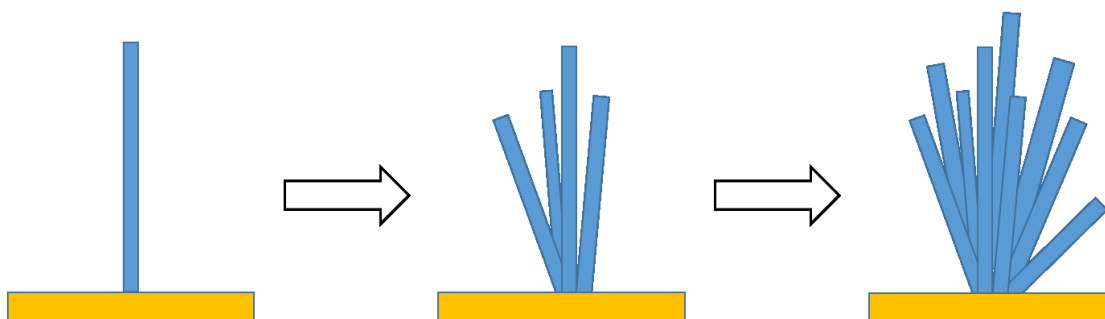


Figure 4-3: Schematic representation of the formation of round particles from coalescing sheets. When a sheet is formed, preferred nucleation sites are introduced at the base of the sheet. New sheets will form heterogeneously at these nucleation sites. As more sheets continue to form alongside each other, they agglomerate and eventually form into round particles.

The accelerated growth of larger particles is initially omnidirectional, until the particle reaches a size of 750-1000 nm. Once a particle reaches this size, the majority of growth occurs in the direction perpendicular to the sample surface; this perpendicular growth is what leads to the formation of vertical rods. It is suspected that directional growth of rods occurs because of the direction of the applied electric field. The particles begin to resemble rods at a deposition time of around 30 s. The morphologies for 30 s and 60 s deposits are shown in Figure 4-4. Particles between rods continue to nucleate and grow and some form into new rods. The rods grow in patches, with new rods forming preferentially in proximity to existing rods. As new rods continue to form, the existing rods continue to grow mostly perpendicular to the surface, but with some lateral growth as well.

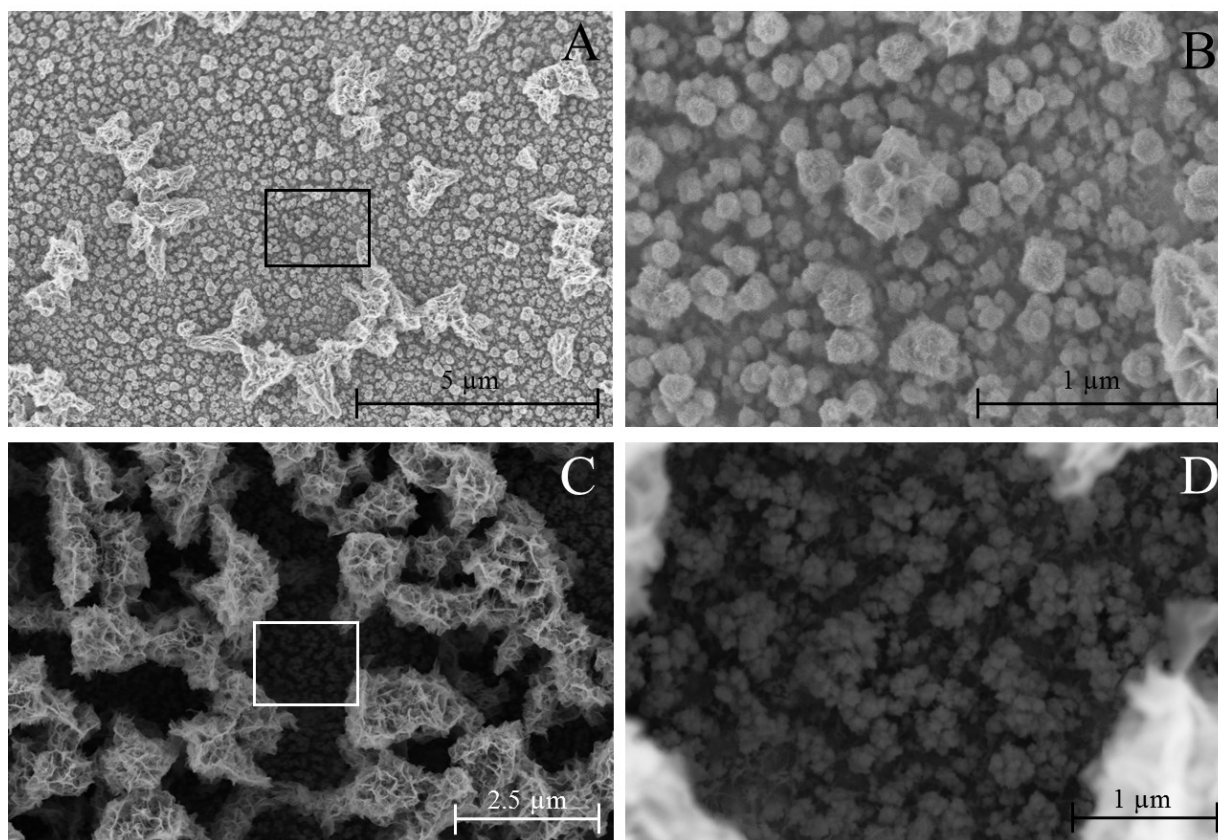


Figure 4-4: SEM SE micrographs of Mn oxide rod formation. Deposition times were (A, B) 30 s and (C, D) 60 s. The boxes in A and C show the fields of view for B and D, respectively.

Figure 4-5 shows the deposit morphology after 5 min. Coverage with rods is nearly complete and there is no longer any space for new rods to form (Figure 4-5A). Figure 4-5B and C show the fibrous morphology of the rod's surface. This fibrous morphology increases the effective surface area of the rods. A cross section view of the Mn oxide rods is shown in Figure 4-5D. The rods are 15-20 μm in length and about 2 μm wide. The bases of the rods are narrower than the tips, giving the rods a slightly petal shape. This occurs because during the vertical growth of the rods, there is also some lateral growth. The lateral growth of the rods causes some rods to be 'squeezed out'; the close packing of neighboring rods can stop the growth of other nearby rods. The circled area in Figure 4-5D shows a rod that has been 'squeezed out' and has only experienced partial growth. After 5 minutes of deposition, the rods that have not been squeezed out are all approximately the same height, even though they formed at different times. The rods all end up approximately the same height because of the poor electronic conductivity of Mn oxide. As the rods get longer, there is an increase in electronic resistance between the current collector (Au layer) and the area where deposition is occurring (top of the rod). This increase in resistance causes an increase in overpotential at the rod surface which reduces the deposition rate. This leads to preferential growth of shorter rods, which has a self-limiting effect on rod height. A schematic of this effect is shown in Figure 4-6. If deposition is continued past 5 min, the lateral growth of rods reaches a point where the tops of the rods begin to fuse. This fusing of rods hinders electrolyte access to areas closer to the Au surface, reducing the effective surface area. Depositions extending past 5 min also experience delamination. A schematic representation of the nucleation and growth of the Mn oxide rods is shown in Figure 4-7.

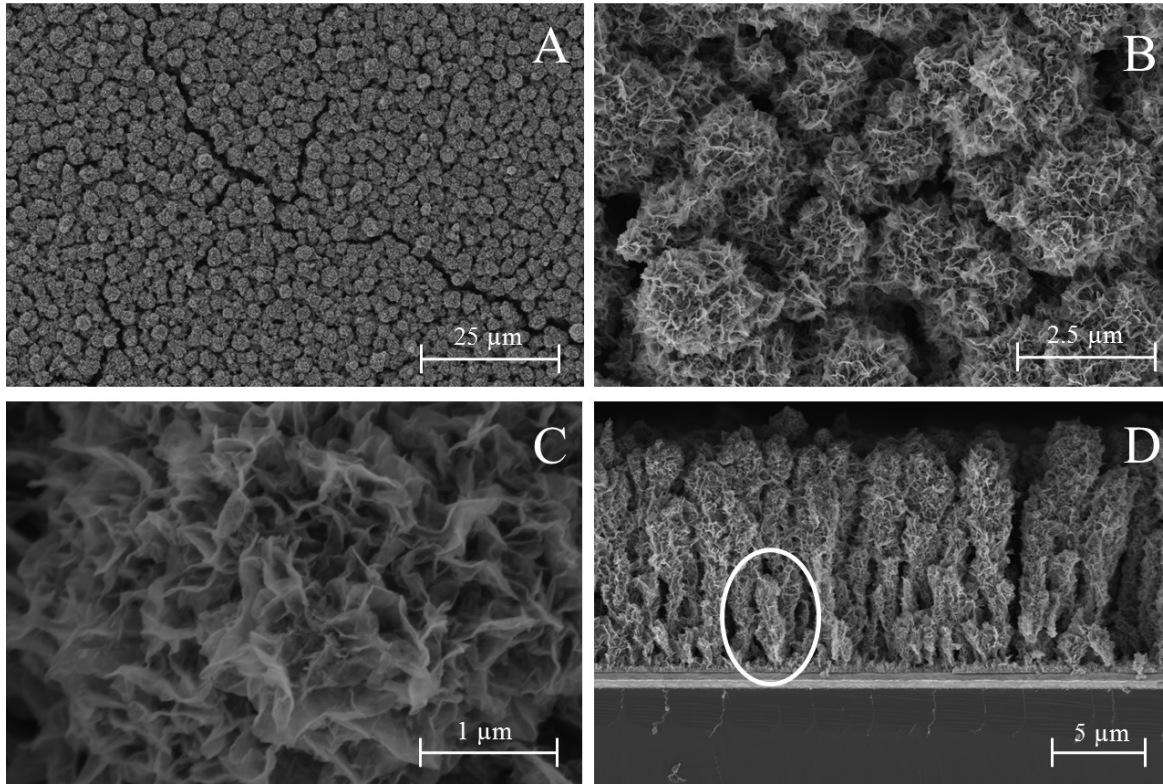


Figure 4-5: SEM SE micrographs showing the Mn oxide rod structure after 5 min deposition. (A-C) are plan view images at successively higher magnifications. (D) is a cross section image. The white circle in (D) shows a rod that has been squeezed out by the growth of neighboring rods.

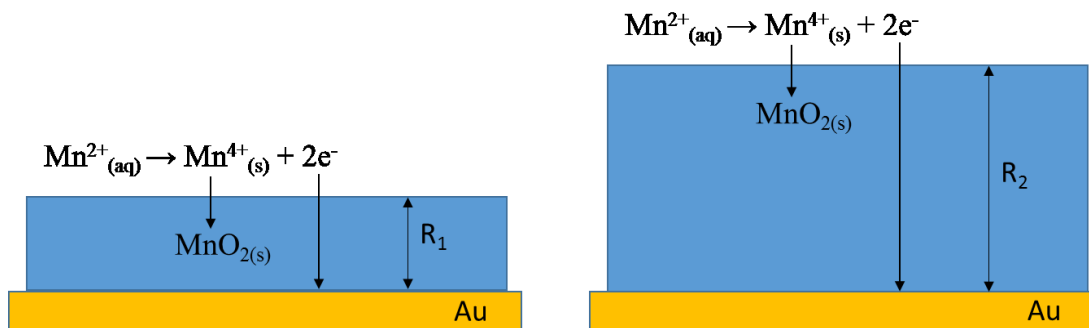


Figure 4-6: Schematic illustrating the effect of increasing deposit height on the resistance of the deposit. As deposition occurs, Mn ions from the solution lose two electrons, each in separate steps: oxidation of Mn^{2+} to Mn^{3+} and oxidation of Mn^{3+} to Mn^{4+} . After each of these steps, the released electron must travel through the Mn oxide deposit to the Au current collector. As the electron passes through the Mn oxide, it experiences some resistance, R . As deposition proceeds, the height and, consequently, the resistance of the oxide layer increases ($R_2 > R_1$). Because Mn oxide is poorly conductive, small changes in deposit height cause large changes in the deposit resistance. An increase in deposit resistance causes a decrease in the potential at the surface of the deposit, which reduces deposition rate. This effect causes shorter rods to grow more quickly than longer rods, and ultimately leads to rods that are uniform in height.

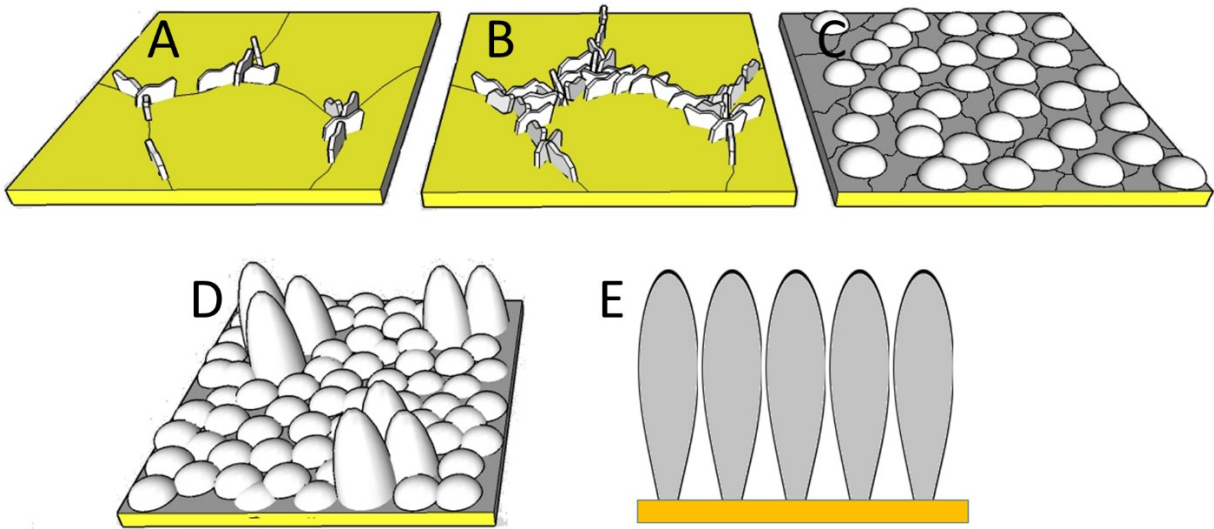


Figure 4-7: Schematic representation of the nucleation and growth process of Mn oxide rods. (A) Nucleation initiates as thin sheets along grain boundaries and triple points. (B) New sheets continue to nucleate, spreading away from the grain boundaries until sheets cover the gold surface. (C) As more sheets form, they begin to agglomerate into round particles. (C) and (D) are at a lower magnification than (A) and (B). (D) Shortly after the transition from sheet-like to round particles, some particles begin to accelerate in growth. At first the accelerated growth is omnidirectional, but once the particle is about 1 μm in diameter, growth is primarily away from the sample surface. As deposition continues, new rods form from the round particles between existing rods. (E) After about 5 min of deposition, the Au surface is covered with petal shaped Mn oxide rods.

4.3.2 X-ray photoelectron spectroscopy

The oxidation states of the 3 and 6 s deposits were determined by peak splitting of the Mn 3s XPS spectrum. The spectra are shown in Figure 4-8. The peak splitting for both deposits was measured to be 5.3 eV. This peak splitting suggests that Mn has an oxidation state of 3+; however, an oxidation state of 2.67+ is also possible (see Section 3.3.4, Figure 3-12). An oxidation state of 2.67+ corresponds to a spinel structure, which contains a mixture of Mn^{2+} and Mn^{3+} ions (2 Mn^{3+} :1 Mn^{2+}). The absence of Mn^{4+} at the early stages of deposition suggest that deposition is not occurring through the disproportionation pathway. TEM results in Section 4.3.3 indicate that the 6 s deposit has a spinel structure and that the structure of the 3 s deposit is an amorphous precursor to this spinel structure. Combining the XPS and TEM results leads to the conclusion that 3 and 6 s deposits have a Mn_3O_4 structure with an oxidation state of 2.67+.

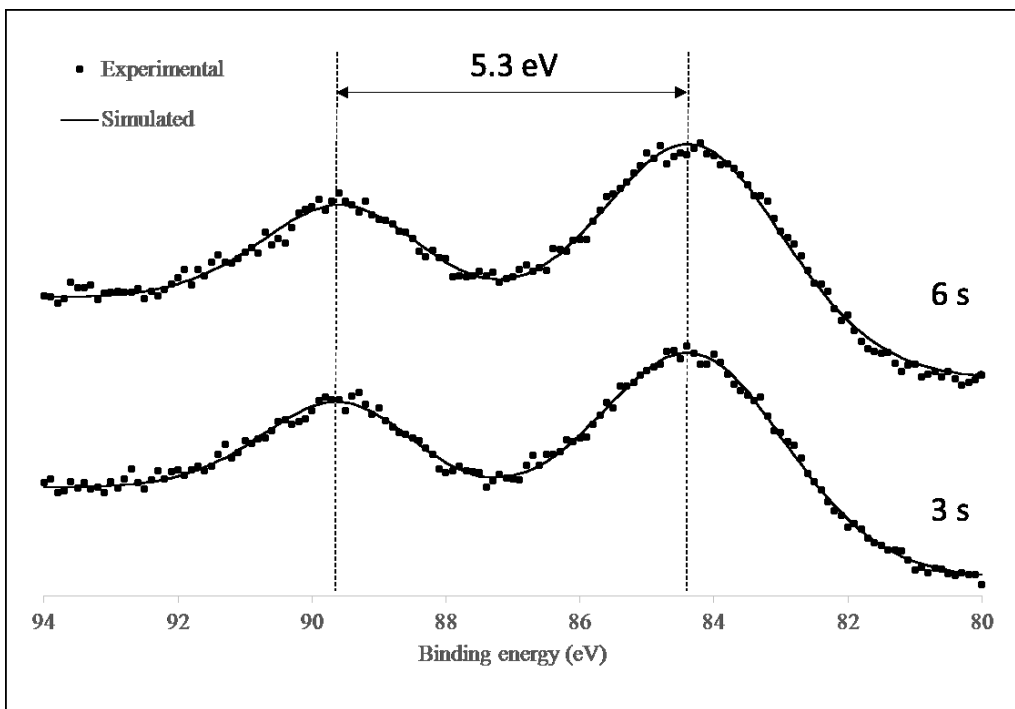


Figure 4-8: Mn 3s XPS spectra for 3 and 6 s Mn oxide deposits prepared on Pt coated Si.

4.3.3 Transmission electron microscopy

Figure 4-9 shows TEM results for Mn oxide deposits after deposition times of 3 s and 6 s. Figure 4-9A shows a bright field image of a cluster of Mn oxide sheets/particles prepared with a deposition time of 3 s. The sheets and particles cluster together during TEM sample preparation due to van der Waals forces. Figure 4-9B is a selected area electron diffraction (SAED) pattern obtained from the area in Figure 4-9A. The diffraction pattern from the 3 s deposit consists of two diffuse low intensity rings, suggesting that the deposit is amorphous at this stage of deposition. The diffuse rings in Figure 4-9B correspond to d spacing values of 0.269 and 0.157 nm and are consistent with the major reflections for a number of MnO_x crystal structures. A portion of the inner ring was used to generate the dark field image shown in Figure 4-9C. Because the deposit is essentially amorphous at this stage of deposition, the dark field image shows no crystalline regions.

A bright field image of a deposit prepared after 6 s is shown in Figure 4-9D; the deposit exhibits agglomerated sheets/particles. Figure 4-9E shows a SAED pattern of the area shown in the bright field image. Three rings are observed, at d spacing values of 0.246, 0.216 and 0.153 nm, which can be indexed to a Mn_3O_4 cubic spinel Fd-3m structure (PDF#013-0162) with a lattice

parameter of 0.842 nm. Note, that this is the same diffraction pattern and crystal structure as determined for the longer term depositions in Chapter 3 (e.g., see Figure 3-9). The diffuse rings from the 3 s deposit have similar d spacings to 2 of the 3 rings for the 6 s sample, so the amorphous structure is likely a precursor to the formation of the cubic spinel phase. The diffracted rings in Figure 4-9E are sharper than the ones obtained from the 3 s sample (Figure 4-9B), but are still quite diffuse. A few faint spots are also observed (circled in white); these spots correspond to a lattice spacing of 0.126 nm and are consistent with the (642) plane of the cubic spinel structure. The weak and diffuse nature of the diffraction pattern indicates that the deposit is poorly crystalline at this stage of deposition. Part of the innermost ring was used to generate the dark field image shown in Figure 4-9F. Figure 4-9F shows some crystalline areas with grains that are ~5 nm in diameter, suggesting that crystallization occurs between deposition times of 3 s and 6 s. The majority of the visible grains in the dark field image in Figure 4-9F are along the edges of the Mn oxide particle, likely because these areas are thinner than the center of the agglomerated particle.

Figure 4-10 shows high resolution images of sheets from 3 s and 6 s deposits. Figure 4-10B (6 s) shows a combination of crystalline and amorphous regions, while Figure 4-10A (3 s) shows a completely amorphous structure, confirming that crystallization begins between 3 s and 6 s of deposition. The crystalline region circled in white is about 5 nm across, which is the same size as the bright regions in the dark field image. The bright areas in Figure 4-9F are crystalline regions within an amorphous matrix. The interplanar spacings were measured from the crystalline region in Figure 4-10B 0.26 and 0.29 nm. These planar spacings and the angle between planes are consistent with the (311) and (220) planes of the cubic spinel structure, respectively.

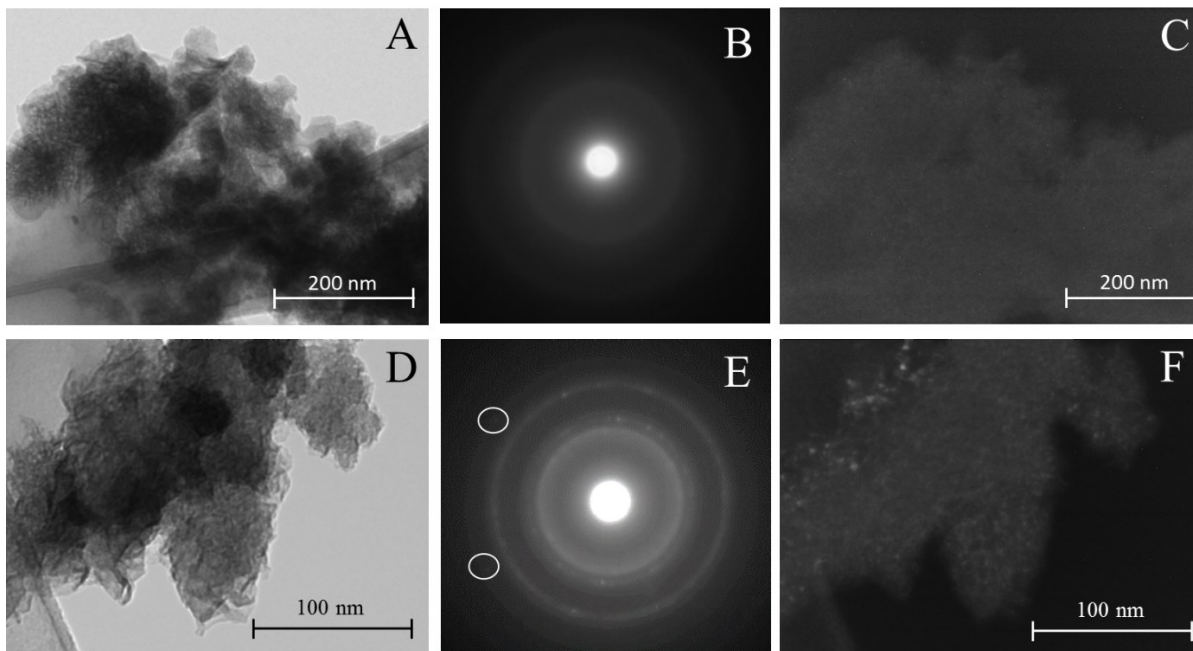


Figure 4-9: TEM results for Mn oxide deposits after deposition times of 3 s (A-C) and 6 s (D-F). Bright field images are shown in A and D, B and E are SAED patterns, and C and F are dark field images.

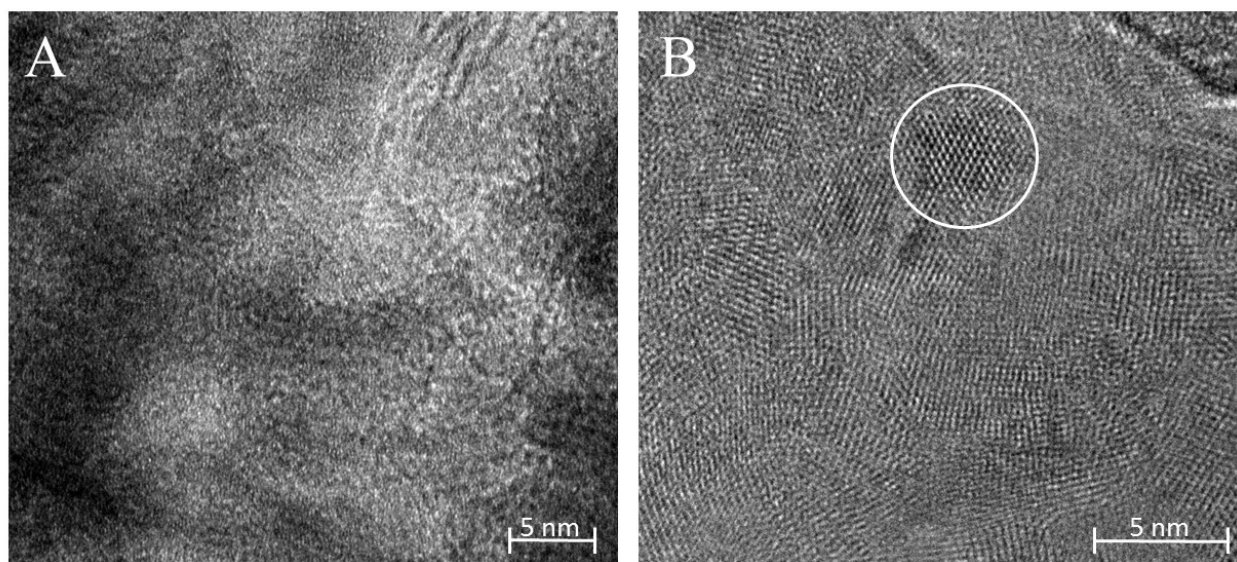


Figure 4-10: High resolution images Mn oxide sheets after a deposition times of 3s (A) and 6 s (B). A shows an amorphous structure while B shows a mixture of crystalline (one example is circled in white) and amorphous regions.

4.4 Conclusions

The nucleation and growth of electrodeposited Mn oxide rods have been characterized using field emission scanning electron microscopy (SEM) and transmission electron microscopy (TEM). SEM imaging shows that nucleation initiates as thin sheets along grain boundaries on the Au surface. The sheet like surface morphology is maintained through all stages of electrodeposition, but the size of the sheets varies. As deposition proceeds past the initial stages of nucleation, the morphology changes to a layer of rounded Mn oxide particles, 25-200 nm in diameter. Some particles accelerate in growth, primarily in the direction of the applied electric field; these growing particles eventually form into rods oriented in the direction of the applied electric field. New rods continue to grow from the particles in the areas between existing rods. Growth of new rods continues until the entire sample surface is covered, which happens at around 5 min of deposition. The rods are 15 to 20 μm long and about 2 μm wide and have a sheet like morphology.

Electron diffraction patterns for 3 and 6 s deposits show a transition from an amorphous structure to a nanocrystalline structure. The 6 s deposit can be indexed to a Mn_3O_4 cubic spinel structure with a lattice parameter of 0.842 nm. Dark field and high resolution imaging showed that 6 s deposits have nanocrystalline areas with grain sizes less than 5 nm. Peak splitting of the Mn 3s x-ray photoelectron spectroscopy (XPS) spectrum was used to determine the oxidation state of Mn oxide deposits. In conjunction with the TEM results, it was determined that the oxidation state of 3 s and 6 s deposits was 2.67+, i.e., a mixed $\text{Mn}^{2+}/\text{Mn}^{3+}$ oxidation state.

4.5 References

- [1] B. Babakhani and D. G. Ivey, "Effect of electrodeposition conditions on the electrochemical capacitive behavior of synthesized manganese oxide electrodes," *J. Power Sources*, vol. 196, no. 24, pp. 10762–10774, Dec. 2011.
- [2] B. Babakhani and D. G. Ivey, "Anodic deposition of manganese oxide electrodes with rod-like structures for application as electrochemical capacitors," *J. Power Sources*, vol. 195, no. 7, pp. 2110–2117, Apr. 2010.
- [3] A. Milchev and L. Heerman, "Electrochemical nucleation and growth of nano- and microparticles: some theoretical and experimental aspects," *Electrochim. Acta*, vol. 48, no. 20–22, pp. 2903–2913, Sep. 2003.

- [4] M. R. Majidi, K. Asadpour-Zeynali, and B. Hafezi, "Reaction and nucleation mechanisms of copper electrodeposition on disposable pencil graphite electrode," *Electrochim. Acta*, vol. 54, no. 3, pp. 1119–1126, Jan. 2009.
- [5] M. Huynh, D. K. Bediako, Y. Liu, and D. G. Nocera, "Nucleation and Growth Mechanisms of an Electrodeposited Manganese Oxide Oxygen Evolution Catalyst," *J. Phys. Chem. C*, vol. 118, no. 30, pp. 17142–17152, Jul. 2014.
- [6] M. F. Dupont and S. W. Donne, "Nucleation and Growth of Electrodeposited Manganese Dioxide for Electrochemical Capacitors," *Electrochim. Acta*, vol. 120, pp. 219–225, Feb. 2014.
- [7] R. L. Paul and A. Cartwright, "The Mechanism of the Deposition of Manganese Dioxide Part 2. Electrode Impedance Studies," vol. 201, pp. 113–122, 1986.
- [8] C. Batchelor-McAuley, L. Shao, G. G. Wildgoose, M. L. H. Green, and R. G. Compton, "An electrochemical comparison of manganese dioxide microparticles versus α and β manganese dioxide nanorods: mechanistic and electrocatalytic behaviour," *New J. Chem*, vol. 32, no. 7, p. 1195, 2008.
- [9] S. Nijjer, J. Thonstad, and G. . Haarberg, "Oxidation of manganese(II) and reduction of manganese dioxide in sulphuric acid," *Electrochim. Acta*, vol. 46, no. 2–3, pp. 395–399, Nov. 2000.
- [10] Z. Rogulski, H. Siwek, I. Paleska, and a. Czerwiński, "Electrochemical behavior of manganese dioxide on a gold electrode," *J. Electroanal. Chem*, vol. 543, no. 2, pp. 175–185, Feb. 2003.
- [11] C. J. Clarke, G. J. Browning, and S. W. Donne, "An RDE and RRDE study into the electrodeposition of manganese dioxide," *Electrochim. Acta*, vol. 51, no. 26, pp. 5773–5784, Aug. 2006.
- [12] W. H. Kao and V. J. Weibel, "Electrochemical oxidation of manganese (II) at a platinum electrode," *J. Appl. Electrochem*, vol. 22, pp. 21–27, 1992.
- [13] R. L. Paul and A. Cartwright, "The Mechanism of the Deposition of Manganese Dioxide, Part 3. Rotating Ring-Disc Studies," *J. Electroanal. Chem*, vol. 201, pp. 123–131, 1986.
- [14] Z. Rogulski, M. Chotkowski, and A. Czerwi, "Electrochemical behavior of MnO₂ / RVC system," *J. New Mater. Electrochem. Syst*, vol. 9, pp. 401–408, 2006.
- [15] M. Dupont, A. F. Hollenkamp, and S. W. Donne, "Electrochemically active surface area effects on the performance of manganese dioxide for electrochemical capacitor applications," *Electrochim. Acta*, vol. 104, pp. 140–147, Aug. 2013.

Chapter 5: Conclusions and Recommendations

5.1 Conclusions

5.1.1 Nickel foam work

- A process previously developed by our research group to electrodeposit high surface area Mn oxide rods onto Au coated Si substrates has successfully been applied to a more practical substrate; Ni foam. The rods are composed of many thin sheets, each only a few nm wide; this gives the rods a very fibrous, high surface area morphology. The rods themselves are about 2 μm in diameter and several μm in length.
- X-ray photoelectron spectroscopy (XPS) was used to determine that the oxidation state of as deposited samples; a mixture of Mn^{2+} and Mn^{3+} was found. During cycling, oxidation occurs and after 500 cycles the deposit has an oxidation state of Mn^{4+} .
- High resolution transmission electron microscopy (TEM) imaging showed that the nanoscale sheets composing the Mn oxide rods are nanocrystalline. Electron diffraction showed that as deposited samples have a crystal structure that is either cubic spinel or hexagonal birnessite. In conjunction with XPS results, electron diffraction showed that after 500 cycles the deposit has a hexagonal birnessite MnO_2 crystal structure.
- Capacitance was measured using cyclic voltammetry as well as galvanostatic cycling, with consistent results between the two techniques. Maximum capacitance values for deposits with and without PEDOT were 217 and 144 F/g (690 and 450 mF/cm^2), respectively, measured with galvanostatic cycling at a charge/discharge rate of 0.5 mA/cm^2 .
- During cycling, dissolution and redeposition caused significant microstructural changes to Mn oxide deposits, including cracking and peeling. The application of the PEDOT coating successfully prevented dissolution of Mn oxide deposits for up to 500 cycles. Capacitance retention after 500 cycles for deposits with and without PEDOT was 91% and 113%, respectively. Although deposits without PEDOT exhibited better capacitance retention, deposits with PEDOT still had a larger capacitance after 500 cycles.
- Deposits annealed in air and forming gas (95% N_2 5% H_2) at 350°C for 1 h exhibited capacitances of 93 and 56 F/g (230 and 170 mF/cm^2), respectively, measured with cyclic

voltammetry at 10 mV/s. Annealed deposits showed an increase in crystallinity compared with the as deposited Mn oxide – cubic spinel for the air annealed samples and tetragonal spinel for the forming gas annealed samples.

5.1.2 Nucleation and growth work

- The nucleation and growth process behind the formation of electrodeposited Mn oxide rods has been characterized using field emission electron microscopy. Deposits were prepared and imaged at various deposition times ranging from 0.5 s to 5 min.
- Electron diffraction of a 3 s deposit showed an amorphous crystal structure. After 6 s of deposition, dark field imaging revealed crystalline regions ~5 nm in diameter. In conjunction with XPS results, electron diffraction determined that the crystal structure of these regions was a cubic spinel.
- XPS showed that the oxidation state of both the 3 s and 6 s deposits is likely 2.67+ ($\text{Mn}^{2+}/\text{Mn}^{3+}$), which is in agreement with electron diffraction patterns which were indexed to a cubic spinel structure.
- A model to describe the stages of nucleation and growth of electrodeposited Mn oxide rod has been proposed.

5.2 Recommendations

- Extended cycling beyond 1000 cycles should be done to determine the long term cyclability of deposits with and without PEDOT.
- More work into the annealing of deposits may result in improved performance. Annealing time, temperature and atmosphere can be varied to obtain different crystal structures.
- Deposition conditions for the application of PEDOT can be modified and optimized for Ni foam. The procedure used in this work was taken from previous work by our group without modification and applied to Ni foam. As with the Mn oxide deposition, the conditions used for application of PEDOT can be varied to try and optimize the performance of deposits.

- X-ray photoelectron spectroscopy can be repeated with longer sample times. The spectra obtained for this thesis are quite noisy and more accurate results would help identify the structure of deposits.
- Electron energy loss spectroscopy (EELS) in the TEM may be able to provide information on the oxidation state of deposits with sufficient spatial resolution (nanometer scale) to differentiate between the crystalline and amorphous regions in 6 s deposits. Some work in this area has been initiated.
- TEM analysis should be done on cycled and uncycled samples that have been coated with PEDOT. The capacitance increase for uncoated samples is not observed for PEDOT coated samples. It is unknown whether the samples with PEDOT undergo the same crystallinity and oxidation state changes during cycling that uncoated samples do.
- Accurately measuring the Mn:O composition ratio of deposits could give insight into the identity of the Mn oxide. This could be done using quantitative energy dispersive x-ray spectroscopy with standards.

References

- R. Ko and M. Carlen, "Principles and applications of electrochemical capacitors," *Electrochem. commun.*, vol. 45, pp. 2483–2498, 2000.
- P. Simon and Y. Gogotsi, "Materials for electrochemical capacitors," *Nat. Mater.*, vol. 7, no. 11, pp. 845–54, Nov. 2008.
- G. Wang, L. Zhang, and J. Zhang, "A review of electrode materials for electrochemical supercapacitors," *Chem. Soc. Rev.*, vol. 41, no. 2, pp. 797–828, Jan. 2012.
- W. Wei, X. Cui, W. Chen, and D. G. Ivey, "Manganese oxide-based materials as electrochemical supercapacitor electrodes," *Chem. Soc. Rev.*, vol. 40, no. 3, pp. 1697–721, Mar. 2011.
- Z. Sun, S. Firdoz, E. Y.-X. Yap, L. Li, and X. Lu, "Hierarchically structured MnO₂ nanowires supported on hollow Ni dendrites for high-performance supercapacitors," *Nanoscale*, vol. 5, no. 10, pp. 4379–87, May 2013.
- J. Xiao, S. Yang, L. Wan, F. Xiao, and S. Wang, "Electrodeposition of manganese oxide nanosheets on a continuous three-dimensional nickel porous scaffold for high performance electrochemical capacitors," *J. Power Sources*, vol. 245, pp. 1027–1034, Jan. 2014.
- J. Yang, L. Lian, H. Ruan, F. Xie, and M. Wei, "Nanostructured porous MnO₂ on Ni foam substrate with a high mass loading via a CV electrodeposition route for supercapacitor application," *Electrochim. Acta*, vol. 136, pp. 189–194, Aug. 2014.
- P. Xu, K. Ye, D. Cao, J. Huang, T. Liu, K. Cheng, J. Yin, and G. Wang, "Facile synthesis of cobalt manganese oxides nanowires on nickel foam with superior electrochemical performance," *J. Power Sources*, vol. 268, pp. 204–211, Dec. 2014.
- B. Babakhani and D. G. Ivey, "Effect of electrodeposition conditions on the electrochemical capacitive behavior of synthesized manganese oxide electrodes," *J. Power Sources*, vol. 196, no. 24, pp. 10762–10774, Dec. 2011.
- B. Babakhani and D. G. Ivey, "Anodic deposition of manganese oxide electrodes with rod-like structures for application as electrochemical capacitors," *J. Power Sources*, vol. 195, no. 7, pp. 2110–2117, Apr. 2010.
- B. Babakhani and D. G. Ivey, "Improved capacitive behavior of electrochemically synthesized Mn oxide/PEDOT electrodes utilized as electrochemical capacitors," *Electrochim. Acta*, vol. 55, no. 12, pp. 4014–4024, Apr. 2010.
- R. Ko and M. Carlen, "Principles and applications of electrochemical capacitors," *Electrochem. commun.*, vol. 45, pp. 2483–2498, 2000.

M. Winter and R. Brodd, "What are batteries, fuel cells, and supercapacitors?," *Chem. Rev.*, no. 104, pp. 4245–4269, 2004.

A. S. Aricò, P. Bruce, B. Scrosati, J. Tarascon, W. V. A. N. Schalkwijk, U. De Picardie, J. Verne, and C. Umr-, "Nanostructured materials for advanced energy conversion and storage devices," *Nat. Mater.*, vol. 4, May, 2005.

L. L. Zhang and X. S. Zhao, "Carbon-based materials as supercapacitor electrodes," *Chem. Soc. Rev.*, vol. 38, no. 9, pp. 2520–31, Sep. 2009.

C. Liu, F. Li, L.-P. Ma, and H.-M. Cheng, "Advanced materials for energy storage," *Adv. Mater.*, vol. 22, no. 8, pp. E28–62, Feb. 2010.

H. V. Helmholtz, *Ann. Phys.*, vol. 89, p. 21, 1853.

E. Frackowiak and F. Béguin, "Carbon materials for the electrochemical storage of energy in capacitors," *Carbon N. Y.*, vol. 39, no. 6, pp. 937–950, May 2001.

B. E. Conway, V. Birss, and J. Wojtowicz, "The role and utilization of pseudocapacitance for energy storage by supercapacitors," *J. Power Sources*, vol. 66, no. 1–2, pp. 1–14, May 1997.

B. E. Conway, "TECHNICAL PAPERS' ELECTROCHEMICAL SCIENCE AND TECHNOLOGY Transition from 'Supercapacitor' to 'Battery' Behavior in Electrochemical Energy Storage," *J. Electrochem. Soc.*, vol. 138, no. 6, 1991.

O. Ghodbane, J.-L. Pascal, and F. Favier, "Microstructural effects on charge-storage properties in MnO₂-based electrochemical supercapacitors," *ACS Appl. Mater. Interfaces*, vol. 1, no. 5, pp. 1130–9, May 2009.

M. D. Stoller, S. Park, Y. Zhu, J. An, and R. S. Ruoff, "Graphene-based ultracapacitors," *Nano Lett.*, vol. 8, no. 10, pp. 3498–502, Oct. 2008.

Y. Zhu, S. Murali, M. D. Stoller, K. J. Ganesh, W. Cai, P. J. Ferreira, A. Pirkle, R. M. Wallace, K. A. Cyhosh, M. Thommes, D. Su, E. A. Stach, and R. S. Ruoff, "Carbon-Based Supercapacitors," *Science*, vol. 332, no. June, pp. 1537–1542, 2011.

E. Frackowiak, "Carbon materials for supercapacitor application," *Phys. Chem. Chem. Phys.*, vol. 9, no. 15, pp. 1774–85, Apr. 2007.

R. Ryoo, S. H. Joo, M. Kruk, and M. Jaroniec, "Ordered Mesoporous Carbons," *Adv. Mater.*, vol. 13, no. 9, pp. 677–681, May 2001.

Y. Wang, Z. Shi, Y. Huang, Y. Ma, C. Wang, M. Chen, and Y. Chen, "Supercapacitor Devices Based on Graphene Materials," *J. Phys. Chem. C*, vol. 113, no. 30, pp. 13103–13107, Jul. 2009.

H. Jiang, P. S. Lee, and C. Li, "3D carbon based nanostructures for advanced supercapacitors," *Energy Environ. Sci.*, vol. 6, no. 1, p. 41, 2013.

X. Zhao, B. M. Sánchez, P. J. Dobson, and P. S. Grant, "The role of nanomaterials in redox-based supercapacitors for next generation energy storage devices," *Nanoscale*, vol. 3, no. 3, pp. 839–55, Mar. 2011.

M. Toupin, T. Brousse, and D. Be, "Charge Storage Mechanism of MnO₂ Electrode Used in Aqueous Electrochemical Capacitor," *Chem. Mater.*, vol. 16, no. 9, pp. 3184–3190, 2004.

W. Sugimoto, H. Iwata, K. Yokoshima, Y. Murakami, and Y. Takasu, "Proton and electron conductivity in hydrous ruthenium oxides evaluated by electrochemical impedance spectroscopy: The origin of large capacitance," *J. Phys. Chem. B*, vol. 109, pp. 7330–7338, 2005.

J. P. Zheng, P. J. Cygan, and T. R. Jow, "Hydrous Ruthenium Oxide as an Electrode Material for Electrochemical Capacitors," *J. Electrochem. Soc.*, vol. 142, no. 8, pp. 2–6, 1995.

C.-C. Hu, W.-C. Chen, and K.-H. Chang, "How to Achieve Maximum Utilization of Hydrous Ruthenium Oxide for Supercapacitors," *J. Electrochem. Soc.*, vol. 151, no. 2, p. A281, 2004.

R. N. Deguzman, a Awaluddin, Y. F. Shen, Z. R. Tian, S. L. Suib, S. Ching, and C. L. Oyoung, "Electrical-Resistivity Measurements on Manganese Oxides with Layer and Tunnel Structures - Birnessites, Todorokites, and Cryptomelanes," *Chem. Mater.*, vol. 7, no. 11, pp. 1286–1292, 1995.

Peter, M. Petravić, and Z. Mandić, "New insights into the mechanism of pseudocapacitance deterioration in electrodeposited MnO₂ under negative potentials," *J. Power Sources*, vol. 240, pp. 252–257, Oct. 2013.

O. Ghodbane, F. Ataherian, N.-L. Wu, and F. Favier, "In situ crystallographic investigations of charge storage mechanisms in MnO₂-based electrochemical capacitors," *J. Power Sources*, vol. 206, pp. 454–462, May 2012.

T. Brousse, M. Toupin, R. Dugas, L. Athouël, O. Crosnier, and D. Bélanger, "Crystalline MnO₂ as Possible Alternatives to Amorphous Compounds in Electrochemical Supercapacitors," *J. Electrochem. Soc.*, vol. 153, no. 12, p. A2171, 2006.

C.-C. Ji, M.-W. Xu, S.-J. Bao, C.-J. Cai, R.-Y. Wang, and D.-Z. Jia, "Effect of alkaline and alkaline-earth cations on the supercapacitor performance of MnO₂ with various crystallographic structures," *J. Solid State Electrochem.*, vol. 17, no. 5, pp. 1357–1368, Jan. 2013.

P. Ragupathy, H. N. Vasan, and N. Munichandraiah, "Synthesis and Characterization of Nano-MnO₂ for Electrochemical Supercapacitor Studies," *J. Electrochem. Soc.*, vol. 155, no. 1, p. A34, 2008.

S. Devaraj and N. Munichandraiah, "High Capacitance of Electrodeposited MnO₂ by the Effect of a Surface-Active Agent," *Electrochem. Solid-State Lett.*, vol. 8, no. 7, p. A373, 2005.

M. Kundu and L. Liu, "Direct growth of mesoporous MnO₂ nanosheet arrays on nickel foam current collectors for high-performance pseudocapacitors," *J. Power Sources*, vol. 243, pp. 676–681, Dec. 2013.

M. Kundu, C. C. A. Ng, D. Y. Petrovykh, and L. Liu, "Nickel foam supported mesoporous MnO₂ nanosheet arrays with superior lithium storage performance," *Chem. Commun. (Camb)*, vol. 49, no. 76, pp. 8459–61, Oct. 2013.

M. Yano, S. Suzuki, M. Miyayama, and M. Ohgaki, "Electrode properties and microstructures of MnO₂ nanosheet thin films as cathodes for electrochemical capacitors," *Solid State Ionics*, vol. 233, pp. 32–37, Feb. 2013.

H. Liu, B. Lu, S. Wei, M. Bao, Y. Wen, and F. Wang, "Electrodeposited highly-ordered manganese oxide nanowire arrays for supercapacitors," *Solid State Sci.*, vol. 14, no. 7, pp. 789–793, Jul. 2012.

C.-L. Ho and M.-S. Wu, "Manganese Oxide Nanowires Grown on Ordered Macroporous Conductive Nickel Scaffold for High-Performance Supercapacitors," *J. Phys. Chem. C*, vol. 115, no. 44, pp. 22068–22074, Nov. 2011.

J. Duay, S. A. Sherrill, Z. Gui, E. Gillette, S. B. Lee, and U. States, "Self-Limiting Electrodeposition Properties," *ACS Nano*, vol. 7, no. 2, pp. 1200–1214, 2013.

L. Wang, D. Deng, and K. Y. S. Ng, "Facile one-step synthesis of MnO₂ nanowires on graphene under mild conditions for application in supercapacitors," *J. Mater. Sci.*, vol. 48, no. 18, pp. 6410–6417, May 2013.

T. Yousefi, A. N. Golikand, M. Hossein Mashhadizadeh, and M. Aghazadeh, "Facile synthesis of α -MnO₂ one-dimensional (1D) nanostructure and energy storage ability studies," *J. Solid State Chem.*, vol. 190, pp. 202–207, Jun. 2012.

S. Santhanagopalan, A. Balram, and D. D. Meng, "Scalable High-Power Redox Capacitors with Aligned Nanoforests of Crystalline MnO₂ Nanorods by High Voltage Electrophoretic Deposition," *ACS Nano*, vol. 7, no. 3, pp. 2114–2125, 2013.

Z. Song, W. Liu, M. Zhao, Y. Zhang, G. Liu, C. Yu, and J. Qiu, "A facile template-free synthesis of α -MnO₂ nanorods for supercapacitor," *J. Alloys Compd.*, vol. 560, pp. 151–155, May 2013.

S. H. Lee, H. Lee, M. S. Cho, J.-D. Nam, and Y. Lee, "Morphology and composition control of manganese oxide by the pulse reverse electrodeposition technique for high performance supercapacitors," *J. Mater. Chem. A*, vol. 1, no. 46, p. 14606, 2013.

S. Chen, T. Zhai, X.-H. Lu, M.-Z. Zhang, Z.-Y. Li, C.-W. Xu, and Y. Tong, "Large-area manganese oxide nanorod arrays as efficient electrocatalyst for oxygen evolution reaction," *Int. J. Hydrogen Energy*, vol. 37, no. 18, pp. 13350–13354, Sep. 2012.

Z. G. Ye, X. L. Zhou, H. M. Meng, X. Z. Hua, Y. H. Dong, and A. H. Zou, "The Electrochemical Characterization of Electrochemically Synthesized MnO₂-Based Mixed Oxides for Supercapacitor Applications," *Adv. Mater. Res.*, vol. 287–290, pp. 1290–1298, Jul. 2011.

B. Babakhani and D. G. Ivey, "Investigation of electrochemical behavior of Mn–Co doped oxide electrodes for electrochemical capacitors," *Electrochim. Acta*, vol. 56, no. 13, pp. 4753–4762, May 2011.

J. Kang, A. Hirata, L. Kang, X. Zhang, Y. Hou, L. Chen, C. Li, T. Fujita, K. Akagi, and M. Chen, "Enhanced supercapacitor performance of MnO₂ by atomic doping," *Angew. Chem. Int. Ed. Engl.*, vol. 52, no. 6, pp. 1664–7, Feb. 2013.

G. A. Snook, P. Kao, and A. S. Best, "Conducting-polymer-based supercapacitor devices and electrodes," *J. Power Sources*, vol. 196, no. 1, pp. 1–12, Jan. 2011.

Q. Pei, G. Zuccarello, M. Ahlskog, and O. Inganäs, "Electrochromic and highly stable poly(3,4-ethylenedioxythiophene) switches between opaque blue-black and transparent sky blue," *Polymer*, vol. 35, no. 7, pp. 1347–1351, 1994.

S.-B. Yoon and K.-B. Kim, "Effect of poly(3,4-ethylenedioxythiophene) (PEDOT) on the pseudocapacitive properties of manganese oxide (MnO₂) in the PEDOT/MnO₂/multiwall carbon nanotube (MWNT) composite," *Electrochim. Acta*, vol. 106, pp. 135–142, Sep. 2013.

R. Liu and S. Lee, "MnO₂/poly (3, 4-ethylenedioxythiophene) coaxial nanowires by one-step coelectrodeposition for electrochemical energy storage," *J. Am. Chem. Soc.*, vol. 130, pp. 2942–2943, 2008.

K. S. Ryu, Y.-G. Lee, Y.-S. Hong, Y. J. Park, X. Wu, K. M. Kim, M. G. Kang, N.-G. Park, and S. H. Chang, "Poly(ethylenedioxythiophene) (PEDOT) as polymer electrode in redox supercapacitor," *Electrochim. Acta*, vol. 50, no. 2–3, pp. 843–847, Nov. 2004.

J. Hong, I.-H. Yeo, and W. Paik, "Conducting Polymer with Metal Oxide for Electrochemical Capacitor: Poly(3,4-ethylenedioxythiophene) RuO_x Electrode," *J. Electrochem. Soc.*, vol. 148, no. 2, p. A156, 2001.

A. Bahloul, B. Nessark, E. Briot, H. Groult, a. Mauger, K. Zaghieb, and C. M. Julien, "Polypyrrole-covered MnO₂ as electrode material for supercapacitor," *J. Power Sources*, vol. 240, pp. 267–272, Oct. 2013.

R. K. Sharma, a. C. Rastogi, and S. B. Desu, "Manganese oxide embedded polypyrrole nanocomposites for electrochemical supercapacitor," *Electrochim. Acta*, vol. 53, no. 26, pp. 7690–7695, Nov. 2008.

- Y. Huo, H. Zhang, J. Jiang, and Y. Yang, "A three-dimensional nanostructured PANI/MnO_x porous microsphere and its capacitive performance," *J. Mater. Sci.*, vol. 47, no. 19, pp. 7026–7034, Jun. 2012.
- L. Deng, Z. Hao, J. Wang, G. Zhu, L. Kang, Z.-H. Liu, Z. Yang, and Z. Wang, "Preparation and capacitance of graphene/multiwall carbon nanotubes/MnO₂ hybrid material for high-performance asymmetrical electrochemical capacitor," *Electrochim. Acta*, vol. 89, pp. 191–198, Feb. 2013.
- L. Li, C. Chen, J. Xie, Z. Shao, and F. Yang, "The preparation of carbon nanotube/MnO₂ composite fiber and its application to flexible micro-supercapacitor," *J. Nanomater.*, vol. 2013, pp. 2–6, 2013.
- Q. Cheng, J. Tang, J. Ma, H. Zhang, N. Shinya, and L.-C. Qin, "Graphene and nanostructured MnO₂ composite electrodes for supercapacitors," *Carbon N. Y.*, vol. 49, no. 9, pp. 2917–2925, Aug. 2011.
- G. Yu, L. Hu, M. Vosgueritchian, and H. Wang, "Solution-processed graphene/MnO₂ nanostructured textiles for high-performance electrochemical capacitors," *Nano Lett.*, vol. 11, pp. 2905–2911, 2011.
- Y. Hou, Y. Cheng, T. Hobson, and J. Liu, "Design and synthesis of hierarchical MnO₂ nanospheres/carbon nanotubes/conducting polymer ternary composite for high performance electrochemical electrodes," *Nano Lett.*, vol. 10, no. 7, pp. 2727–33, Jul. 2010.
- Z. Lei, F. Shi, and L. Lu, "Incorporation of MnO₂-Coated Carbon Nanotubes between Graphene Sheets as Supercapacitor Electrode," *Appl. Mater. Interfaces*, vol. 4, pp. 1058–1064, 2012.
- C. Yuan, L. Hou, L. Yang, D. Li, L. Shen, F. Zhang, and X. Zhang, "Facile interfacial synthesis of flower-like hierarchical α -MnO₂ sub-microspherical superstructures constructed by two-dimension mesoporous nanosheets and their application in electrochemical capacitors," *J. Mater. Chem.*, vol. 21, no. 40, p. 16035, 2011.
- P.-C. Gao, A.-H. Lu, and W.-C. Li, "Dual functions of activated carbon in a positive electrode for MnO₂-based hybrid supercapacitor," *J. Power Sources*, vol. 196, no. 8, pp. 4095–4101, Apr. 2011.
- J. C. Zhao, B. H. Tang, L. Sun, J. Zheng, J. Cao, and J. L. Xu, "Effect of loading amount on capacitance performances of MnO₂/ordered mesoporous carbon composites," *Mater. Technol.*, vol. 27, no. 4, pp. 328–332, Sep. 2012.
- L. Yuan, X. Lu, X. Xiao, T. Zhai, J. Dai, F. Zhang, B. Hu, and X. Wang, "Flexible Solid-State Supercapacitors Based on Carbon Nanoparticles / MnO₂ Nanorods Hybrid Structure," *ACS Nano*, vol. 6, no. 1, pp. 656–661, 2012.

X. Lu, D. Zheng, T. Zhai, Z. Liu, Y. Huang, S. Xie, and Y. Tong, "Facile synthesis of large-area manganese oxide nanorod arrays as a high-performance electrochemical supercapacitor," *Energy Environ. Sci.*, vol. 4, no. 8, p. 2915, 2011.

M. Yu, T. Zhai, X. Lu, X. Chen, S. Xie, W. Li, C. Liang, W. Zhao, L. Zhang, and Y. Tong, "Manganese dioxide nanorod arrays on carbon fabric for flexible solid-state supercapacitors," *J. Power Sources*, vol. 239, pp. 64–71, Oct. 2013.

Y. Zhang, J. Li, F. Kang, F. Gao, and X. Wang, "Fabrication and electrochemical characterization of two-dimensional ordered nanoporous manganese oxide for supercapacitor applications," *Int. J. Hydrogen Energy*, vol. 37, no. 1, pp. 860–866, Jan. 2012.

M. Chigane, M. Ishikawa, and M. Izaki, "Preparation of Manganese Oxide Thin Films by Electrolysis/Chemical Deposition and Electrochromism," *J. Electrochem. Soc.*, vol. 148, no. 7, p. D96, 2001.

M. Chigane and M. Ishikawa, "Manganese oxide thin film preparation by potentiostatic electrolyses and electrochromism," *J. Electrochem. Soc.*, vol. 147, no. May 2010, pp. 2246–2251, 2000.

H. Ashassi-Sorkhabi, E. Asghari, and P. La'le Badakhshan, "Potentiostatic and cyclic voltammetric deposition of nanostructured manganese oxide for supercapacitor applications," *Curr. Appl. Phys.*, vol. 14, no. 2, pp. 187–191, Feb. 2014.

X. Lang, A. Hirata, T. Fujita, and M. Chen, "Nanoporous metal/oxide hybrid electrodes for electrochemical supercapacitors," *Nat. Nanotechnol.*, vol. 6, no. 4, pp. 232–6, Apr. 2011.

J. Xu, Z. Li, D. Han, B. Deng, J. Li, and Y. Jiang, "The mechanism of specific capacitance improvement of supercapacitors based on MnO₂ at an elevated operating temperature," *Thin Solid Films*, vol. 520, no. 18, pp. 5952–5959, Jul. 2012.

M. J. Tadjer, M. a. Mastro, J. M. Rojo, A. B. Mojena, F. Calle, F. J. Kub, and C. R. Eddy, "MnO₂-Based Electrochemical Supercapacitors on Flexible Carbon Substrates," *J. Electron. Mater.*, vol. 43, no. 4, pp. 1188–1193, Feb. 2014.

X. Zhang, X. Liu, B. Li, Q. Chu, Y. Wang, X. Zhao, and X. Wang, "Rapid microwave synthesis of δ -MnO₂ microspheres and their electrochemical property," *J. Mater. Sci. Mater. Electron.*, vol. 24, no. 7, pp. 2189–2196, Feb. 2013.

S. Komaba, T. Tsuchikawa, A. Ogata, N. Yabuuchi, D. Nakagawa, and M. Tomita, "Nanostructured birnessite prepared by electrochemical activation of manganese(III)-based oxides for aqueous supercapacitors," *Electrochim. Acta*, vol. 59, pp. 455–463, Jan. 2012.

S. Komaba, A. Ogata, and T. Tsuchikawa, "Enhanced supercapacitive behaviors of birnessite," *Electrochem. commun.*, vol. 10, no. 10, pp. 1435–1437, Oct. 2008.

T. Zhou, S. Mo, S. Zhou, W. Zou, Y. Liu, and D. Yuan, "Mn₃O₄/worm-like mesoporous carbon synthesized via a microwave method for supercapacitors," *J. Mater. Sci.*, vol. 46, no. 10, pp. 3337–3342, Jan. 2011.

G. H. A. Therese and P. V. Kamath, "Electrochemical Synthesis of Metal Oxides and Hydroxides," *Chem. Mater.*, vol. 12, no. 5, pp. 1195–1204, May 2000.

A. D. Cross, A. Morel, T. F. Hollenkamp, and S. W. Donne, "Chronoamperometric Versus Galvanostatic Preparation of Manganese Oxides for Electrochemical Capacitors," *J. Electrochem. Soc.*, vol. 158, no. 10, p. A1160, 2011.

W. Wei, X. Cui, X. Mao, W. Chen, and D. G. Ivey, "Morphology evolution in anodically electrodeposited manganese oxide nanostructures for electrochemical supercapacitor applications—Effect of supersaturation ratio," *Electrochim. Acta*, vol. 56, no. 3, pp. 1619–1628, Jan. 2011.

L. Pigani, A. Heras, Á. Colina, R. Seeber, and J. López-Palacios, "Electropolymerisation of 3,4-ethylenedioxythiophene in aqueous solutions," *Electrochem. commun.*, vol. 6, no. 11, pp. 1192–1198, Nov. 2004.

N. Sakmeche, S. Aeiyaich, and J. Aaron, "Improvement of the electrosynthesis and physicochemical properties of poly (3, 4-ethylenedioxythiophene) using a sodium dodecyl sulfate micellar aqueous medium," *Langmuir*, vol. 1, no. 28, pp. 2566–2574, 1999.

M. A. Valle, P. Cury, and R. Schrebler, "Solvent effect on the nucleation and growth mechanisms of poly (thiophene)," *Electrochim. Acta*, vol. 48, pp. 397–405, 2002.

M. Morvant and J. Reynolds, "In situ conductivity studies of poly (3, 4-ethylenedioxythiophene)," *Synth. Met.*, vol. 92, pp. 57–61, 1998.

A. Milchev and L. Heerman, "Electrochemical nucleation and growth of nano- and microparticles: some theoretical and experimental aspects," *Electrochim. Acta*, vol. 48, no. 20–22, pp. 2903–2913, Sep. 2003.

M. R. Majidi, K. Asadpour-Zeynali, and B. Hafezi, "Reaction and nucleation mechanisms of copper electrodeposition on disposable pencil graphite electrode," *Electrochim. Acta*, vol. 54, no. 3, pp. 1119–1126, Jan. 2009.

J. Booth, R. G. Compton, and J. H. Atherton, "Mechanism of Solid / Liquid Interfacial Reactions . Atomic Force Microscopy Studies of the Self-Passivating Reaction between Solid p -Chloranil and Aqueous Phase N , N -Dimethylphenylenediamine," vol. 5647, no. 010, pp. 3980–3985, 2010.

B. J. Hwang, R. Santhanam, and Y.-L. Lin, "Nucleation and Growth Mechanism of Electropolymerization of Polypyrrole on Gold/Highly Oriented Pyrolytic Graphite Electrode," *J. Electrochem. Soc.*, vol. 147, no. 6, p. 2252, 2000.

A. Milchev, "Electrochemical alloy formation—theory of progressive and instantaneous nucleation without overlap," *Electrochim. Acta*, vol. 42, no. 10, pp. 1533–1536, Jan. 1997.

Z. Guo and L. Tan, *Fundamentals and Applications of Nanomaterials*. Norwood: Artech House, 2009.

R. J. Stokes and D. F. Evans, *Fundamentals of Interfacial Engineering*. New York: Wiley, 1997.

J. Goldstein, D. Newbury, D. Joy, C. Lyman, P. Echlin, E. Lifshin, L. Sawyer, and J. Michael, *Scanning Electron Microscopy and X-Ray Microanalysis*, Third. New York: Springer Science, 2003.

T. B. Reddy, *Linden's Handbook of Batteries*, Fourth Edi. New York: McGraw-Hill Education, 2011.

Y. Gorlin and T. F. Jaramillo, "A bifunctional nonprecious metal catalyst for oxygen reduction and water oxidation," *J. Am. Chem. Soc.*, vol. 132, pp. 13612–13614, 2010.

M. Huynh, D. K. Bediako, Y. Liu, and D. G. Nocera, "Nucleation and Growth Mechanisms of an Electrodeposited Manganese Oxide Oxygen Evolution Catalyst," *J. Phys. Chem. C*, vol. 118, no. 30, pp. 17142–17152, Jul. 2014

M. F. Dupont and S. W. Donne, "Nucleation and Growth of Electrodeposited Manganese Dioxide for Electrochemical Capacitors," *Electrochim. Acta*, vol. 120, pp. 219–225, Feb. 2014.

R. L. Paul and A. Cartwright, "The Mechanism of the Deposition of Manganese Dioxide Part 2. Electrode Impedance Studies," vol. 201, pp. 113–122, 1986.

C. Batchelor-McAuley, L. Shao, G. G. Wildgoose, M. L. H. Green, and R. G. Compton, "An electrochemical comparison of manganese dioxide microparticles versus α and β manganese dioxide nanorods: mechanistic and electrocatalytic behaviour," *New J. Chem*, vol. 32, no. 7, p. 1195, 2008.

S. Nijjer, J. Thonstad, and G. . Haarberg, "Oxidation of manganese(II) and reduction of manganese dioxide in sulphuric acid," *Electrochim. Acta*, vol. 46, no. 2–3, pp. 395–399, Nov. 2000.

Z. Rogulski, H. Siwek, I. Paleska, and a. Czerwiński, "Electrochemical behavior of manganese dioxide on a gold electrode," *J. Electroanal. Chem*, vol. 543, no. 2, pp. 175–185, Feb. 2003.

C. J. Clarke, G. J. Browning, and S. W. Donne, "An RDE and RRDE study into the electrodeposition of manganese dioxide," *Electrochim. Acta*, vol. 51, no. 26, pp. 5773–5784, Aug. 2006.

W. H. Kao and V. J. Weibel, "Electrochemical oxidation of manganese (II) at a platinum electrode," *J. Appl. Electrochem*, vol. 22, pp. 21–27, 1992.

R. L. Paul and A. Cartwright, "The Mechanism of the Deposition of Manganese Dioxide, Part 3. Rotating Ring-Disc Studies," *J. Electroanal. Chem*, vol. 201, pp. 123–131, 1986.

Z. Rogulski, M. Chotkowski, and A. Czerwi, "Electrochemical behavior of MnO₂ / RVC system," *J. New Mater. Electrochem. Syst*, vol. 9, pp. 401–408, 2006.

M. Dupont, A. F. Hollenkamp, and S. W. Donne, "Electrochemically active surface area effects on the performance of manganese dioxide for electrochemical capacitor applications," *Electrochim. Acta*, vol. 104, pp. 140–147, Aug. 2013.

Appendix

Hexagonal Birnessite Diffraction Card

PDF#18-0802: QM=Doubtful(?); d=Other/Unknown; I=(Unknown)															PDF Card		
Birnessite, syn																	
MnO2																	
Radiation=CuKa1					Lambda=1.5406					Filter=							
Calibration=					d-Cutoff=					I/Ic(RIR)=							
Ref= Level-1 PDF																	
Hexagonal(Unknown),										Z=15			mp=				
Cell=5.82x5.82x14.62<90x90x120>										Pearson=							
Density(c)=5.05			Density(m)=			Mwt=			Vol=								
Ref= Ibid.																	
Strong Line: 2.44/X 4.75/9 1.42/8 7.20/8 2.12/4 1.27/1 1.67/1																	
7 Lines, Wavelength to Compute Theta = 1.54056A(Cu), I%-Type = (Unknown)																	
#	d(A)	I(f)	h	k	l	2-Theta	Theta	1/(2d)	#	d(A)	I(f)	h	k	l	2-Theta	Theta	1/(2d)
1	7.2000	80.0	0	0	2	12.283	6.141	0.0598	5	1.6700	10.0	3	0	1	54.935	27.468	0.2578
2	4.7500	90.0	1	0	1	18.665	9.333	0.0906	6	1.4200	80.0	1	1	9	65.701	32.851	0.3032
3	2.4400	100.0	0	0	6	36.805	18.402	0.1765	7	1.2700	10.0				74.677	37.338	0.3390
4	2.1200	40.0				42.611	21.305	0.2031									

Cubic Spinel Diffraction Card

PDF#00-013-0162(RDB): QM=Indexed(I); d=(Unknown); I=Diffractometer
Manganese Oxide
Mn3 O4
Radiation=FeKa Lambda=1.9373 Filter=
Calibration= 2T=18.239-89.308 I/Ic(RIR)=I
Ref: Faulring, Zwicker, Forgeng.
Am. Mineral., v45 p947 (1960)
Cubic - Powder Diffraction, Fd-3m (227) Z=8 mp=
CELL: 8.42 x 8.42 x 8.42 <90.0 x 90.0 x 90.0> P.S=cF56.00
Density(c)=5.092 Density(m)= Mwt=228.81 Vol=596.95 F(12)=15(0.045,18/0)
Ref: Ibid.

Strong Lines: 2.54/X 1.49/6 2.98/5 4.86/5 2.10/5 1.62/5 1.10/4 1.28/2
Sample Preparation: Spinel structure, formed by heating cryptomelane above 900 C for a prolonged period (critical temperature of formation about 1050 C).
Contains about 4% K2 O as impurity.
Unit Cell Data Source: Powder Diffraction.

2-Theta	d(Å)	I(f)	(h k l)	Theta	1/(2d)	2pi/d	n^2
18.239	4.8600	50.0	(1 1 1)	9.120	0.1029	1.2928	3
29.961	2.9800	50.0	(2 2 0)	14.980	0.1678	2.1085	8
35.308	2.5400	100.0	(3 1 1)	17.654	0.1969	2.4737	11
36.962	2.4300	10.0	(2 2 2)	18.481	0.2058	2.5857	12
43.038	2.1000	50.0	(4 0 0)	21.519	0.2381	2.9920	16
53.278	1.7180	20.0	(4 2 2)	26.639	0.2910	3.6573	24
56.783	1.6200	50.0	(5 1 1)	28.391	0.3086	3.8785	27
62.352	1.4880	60.0	(4 4 0)	31.176	0.3360	4.2226	32
73.728	1.2840	20.0	(5 3 3)	36.864	0.3894	4.8934	43
78.690	1.2150	10.0	(4 4 4)	39.345	0.4115	5.1713	48
86.330	1.1260	10.0	(6 4 2)	43.165	0.4440	5.5801	56
89.308	1.0960	40.0	(7 3 1)	44.654	0.4562	5.7328	59

Tetragonal Spinel Diffraction Card

PDF#00-018-0803(RDB): QM=Doubtful(0); d=Debye-Scherrer(114.6mm); I=(Unknown)

Manganese Oxide

Mn₃O₄

Radiation=FeK α Lambda=1.9373 Filter=Mn

Calibration= 2 θ =18.015-98.084 I/Ic(RIR)=0

Ref: Bricker.

Am. Mineral., v50 p1296 (1965)

Tetragonal - Powder Diffraction, I41/amd (141) Z=4 mp=

CELL: 5.78 x 5.78 x 9.33 <90.0 x 90.0 x 90.0> P.S=tI28.00 (Å)

Density(c)=4.876 Density(m)= Mwt=228.81 Vol=311.70 F(19)=2.6(0.152,48/6)

Ref: Ibid.

Strong Lines: 2.49/X 3.08/9 2.76/9 1.54/8 4.92/7 2.04/6 2.36/3 1.34/3

General Comments: Pattern very similar to Mn₃O₄ (hausmannite).

Close to MnOOH inverts to \bar{a} MnOOH on standing in water suspension for several months.

Z by analogy with hausmannite, L.G.B., assuming Mn10.66 O16.

Additional Patterns: To replace 00-006-0540.

Analysis: Analysis gave Mn 01.442 ·0.49 H₂ O.

Sample Preparation: Synthetic, formed by treatment of a suspension of Mn₃O₄ by oxygen gas.

Unit Cell Data Source: Powder Diffraction.

2-Theta	d(Å)	I(f)	(h k l)	Theta	1/(2d)	2 π /d	n ²
18.015	4.9200	70.0	(1 0 1)	9.008	0.1016	1.2771	
28.966	3.0800	90.0	(1 1 2)	14.483	0.1623	2.0400	
31.027	2.8800	20.0	(2 0 0)	15.513	0.1736	2.1817	
32.412	2.7600	90.0	(1 0 3)	16.206	0.1812	2.2765	
36.041	2.4900	100.0	(2 1 1)	18.020	0.2008	2.5234	
38.100	2.3600	30.0		19.050	0.2119	2.6624	
44.370	2.0400	60.0	(2 2 0)	22.185	0.2451	3.0800	
49.786	1.8300	10.0		24.893	0.2732	3.4334	
50.977	1.7900	30.0		25.489	0.2793	3.5102	
53.887	1.7000	20.0	(3 1 2)	26.944	0.2941	3.6960	
56.029	1.6400	10.0	(3 0 3)	28.014	0.3049	3.8312	
58.764	1.5700	30.0		29.382	0.3185	4.0020	
60.025	1.5400	80.0	(2 2 4)	30.013	0.3247	4.0800	
64.678	1.4400	30.0	(3 1 4)	32.339	0.3472	4.3633	